CENTRO DE INVESTIGACIONES
EN OPTICA, A.C.

"ANALYSIS OF HYBRID PEROVSKITE FILMS ($MAPbI_3$) FABRICATED BY THE ONE AND TWO-STEPS METHODS."

Thesis submitted in fulfillment of the requirements for the Ph.D degree in science (Optics)

Present: Diana-Marcela Montoya-Montoya

Advisor: Dr. J. Oracio C Barbosa-García
Co-advisor: Dr. Enrique Pérez-Gutiérrez

León Guanajuato México
September 2021

Abstract

In the field of new technologies for renewable energy production, hybrid solar cells based on organic-inorganic perovskite material (HPSC) are now in the way to become a new real alternative. However, in the fabrication of perovskite films to be used as active layer in HPSC, some parameters like homogeneous morphology and pure crystallization should be controlled because they can affect the conversion efficiency of devices.

In this work, the one-step and the two-step methods (with close-spaced sublimation and spin-coating with sequential deposition) were used to deposit $MAPbI_3$ perovskite films. For both methods, there are several variables to control the perovskite formation and film quality. The influence of anti-solvent, the time for its addition, and the annealing temperature on the features of perovskite films were studied for the one-step method. The temperature for deposition of the inorganic film was studied for the close-spaced sublimation method, and the time that MAI-solution remains onto the PbI_2 film before the spin process began was studied for spin-coating with sequential deposition methods. The morphology, the UV-Vis absorption spectra, and the XRD pattern for each film were analyzed to determine the film quality.

The $MAPbI_3$ perovskite films were used as the active layer in HPSCs with inverted architecture, the average photovoltaic performance of the devices was affected by the film features. In addition, the electron transport layer and counter electrode interface generated by the use of an alternative cathode was also studied. It was found that a poor physical contact at the ETL/CE interface does not drastically affect the efficiency of the device.

Acknowledgements

- I would like to express my appreciation to my advisors, Dr. Enrique Pérez-Gutierrez and Dr. Oracio Barbosa-Garcia, for their valuable supervision, suggestions and patience, which made me a better professional. I wish to express my sincere thanks to Dr. Enrique Pérez-Gutierrez to transmit his experience and knowledge of this work area.

- I would like to thank my evaluation committee members, Dr. José Luis Maldonado, Dr. Mario Rodriguez, Dr. Diego Solis Ibarra and Dra. Ma. Concepción Arenas, for their time and comments which contributed to the improvement of my thesis project.

- I am grateful to Dr. José Luis Maldonado, Dr. Mario Rodriguez and Dr. Antonio Menses for their teaching, motivation and valuable comments to improve this work.

- I thank to Dr. Wilson Bernal for technical support with the deposit of the evaporated electrodes, Christian Albor for assistance with XRD and SEM measurements and Martin Olmos for technical support.

- Additionally, I would like to thank Mexico for receiving me and for having given me the opportunity to train as a scientist, I would especially like to thank to Centro de Investigaciones en Óptica (CIO) and Grupo de Propiedades Ópticas de la Materia (GPOM) to providing me all the necessary facilities to develop this research. I appreciate collaborations and suggestions from all group members; researchers, technicians and students. I also want to thank CONACYT for granting me a doctoral scholarship.

-Last, but no least important, I want to thank God for my life and for everything that surrounds me. I would like to thank my families, Montoya-Mejia and Bernal-Pinilla, for their unconditional love and support. Above all, thanks my dear sister Vane and mother Maria for teaching me to be a strong and courageous women; I especially thank to my husband Wilson for loving, supporting and providing me quiet. I also enjoyed our scientific discussions. Thanks to my friends of different nationalities for the shared experiences and for the support they gave me in the most difficult moments. And of course thanks to my dear baby who came to accompany me in the last process of this project.

Contents

List of figures

List of tables

1. Introduction

Most countries have been seeking to change traditional energy sources to renewable energy to address the increasingly severe impact of the energy crisis, especially global warming and to ensure a sustainable future. Renewable energy technologies are essential contributors to reducing dependency on fossil fuels and providing opportunities for mitigating greenhouse gas production.

According to the issued report by the Renewables 2020 Global Status Report for the 21st Century (REN21) in 2020, [1] the estimated share of renewable energy in global electricity production increased considerably; however, by the end of 2019 it was 27.3% and the rest, 72.7%, was coming from non-renewable sources. Energy sources such as solar, wind and hydropower showed the highest participation in renewable electricity generation with a percentage of 2.8%, 5.9% and 15.9% respectively (see Figure 1.1).

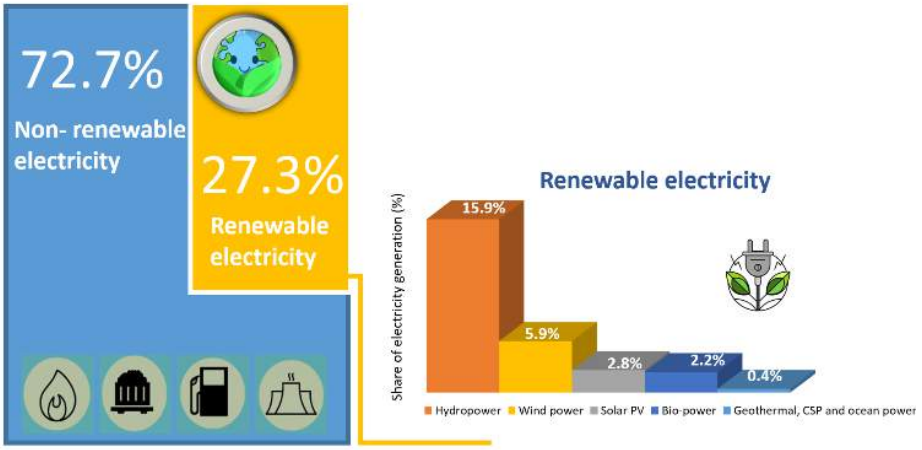

Figure 1.1 Estimated renewable energy share of global electricity production, end 2019. Data from [1]

Nevertheless, solar energy is an interesting technology with increasing use as renewable source; in late 2019, it was estimated that solar energy production increased by more than 30% (producing more than 580 TWh) worldwide over the previous year. [2] The top 10 countries with the highest cumulative solar capacity are: China, United States, India, Japan, Australia, Germany, Mexico, Korea, Turkey and The Netherlands with a percent production of 45%, 11%, 11%, 7%, 4%, 3%, 3%, 2%, 2% and 1% respectively. The remaining 45% corresponds to the rest of the world. [1] The Energy Information Administration (EIA) expects that solar energy would reach, at least, 16 % of the share of global electricity by 2050. [2]

The devices that are used to convert sunlight into electricity are known as solar cells. The operation of solar cells is based in the photovoltaic (PV) effect. In a silicon solar cell, a p-n junction is created by doping the intrinsic material. The PV effect on this junction leads to the generation of the charge carriers due to the absorption of photons. [3] Electrons move to the n-side of the junction, while holes move to the p-side of the junction. Finally, the harvesting of the photo-generated charge carriers at the electrodes of the solar cell occurs.[3] The power conversion efficiency is how much of the incident power on the solar cell is converted into electricity.

The first solar cells were developed in the 1950s at Bell Laboratories; the PV devices were made of p-n junction silicon and converted only 5% of the sun's energy, obtaining 5 mW of power. [4] Nowadays, silicon (Si) is the most common semiconductor used in solar cells. However, semiconductor compounds such as copper indium gallium selenide (CIGS) and cadmium telluride (CdTe) are also used. [4] Inorganic semiconductors have different band gap energy, which determine the adsorbed photons. The optimal band gap,

under one sun illumination, for higher adsorption of solar irradiation is between 1.4-1.5 eV. [5] Depending on the semiconductor material for the active layer, inorganic, organic or hybrid in solar cells, these devices can be classified as first, second and third generation.

First-generation solar cells (Gen-I) refers to Si-based devices; the Si has a bandgap of 1.1 eV and an absorption coefficient of ~10^3 cm^{-1}. These devices represent more than 90% of the current solar energy market. [6] Although this technology has a high conversion efficiency (>20%), some issues should be addressed for a massive application. For instance, the typical thickness of Si wafer is in the range of 100-200 μm. Therefore the consumption of material represents an important part of the costs of the cell. [5] Also, the devices lack of transparency and mechanical flexibility and require special equipment for their fabrication. [4] Second-generation (Gen-II) devices are based on thin films of inorganic semiconductors such as amorphous or microcrystalline silicon (aSi or mcSi), CdTe, CIGS, etc. These materials have a narrow band gap (~1.1-1.5 eV) with absorption coefficient ~10^3-10^4 cm^{-1}. The conversion efficiency of these solar cells has reached values over 20%. [7] Compared with Gen-I, these materials have lower manufacturing costs and better mechanical flexibility but have lower efficiency. Gen-I and Gen-II cells have in common that their performance cannot exceed the theoretical Shockley-Queisser (SQ) limit of 33.7%.[8]

The third generation (Gen-III) solar cells aim at the lowest cost and higher efficiency than Gen-I and II. The active layer in Gen-III of solar cells uses organic as well as hybrid materials that includes Quantum Dot, Organic Dye Sensitized, polymers PV, and lead halide derivate. The band gap of these materials is between 1.5 to 2.7 eV and have

absorption coefficients in the range of 10^5 cm^{-1}. [8] According to Sinke´s work, Gen-III devices could have performance above the SQ limit. [8] Figure 1.2 shows the projection of efficiency and cost for PV technology generations according to Shockley- Queisser limit. [8, 9] Although the efficiencies achieved with this type of technology is high, the devices have scalability and lifetime problems.

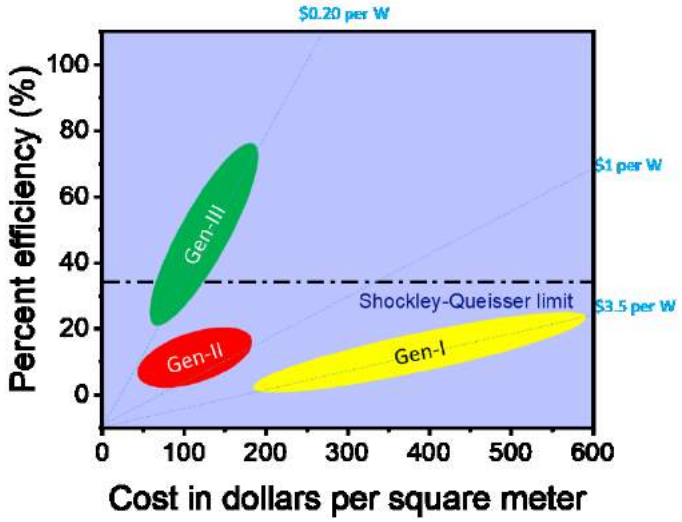

Figure 1.2 The projection of efficiency and cost for PV technology generations. Data from [8]

Important research work concerning Gen-III devices in Mexico is carrying out by developing new active organic materials, improving the structure and efficiency of solar cells. For example, the research Group of Optical Properties of Materials (GPOM) at the Optics Research Center (CIO) has been working in the fabrication of organic photovoltaic cells (OPV) with alternative cathodes such as the Field's metal (FM). This electrode is a eutectic alloy which is made up of 32.5% Bi, 51% In and 16.5% Sn. By optical and atomic force microscopy studies has been reported that FM and organic layers form a homogeneous interface achieving efficiencies to 9.2%. [10] The FM deposit for solar cells is much easier to do since is through drop casting at low temperature (~ 85 ºC) and room

atmospheric conditions; this in contrast to the deposit of standard cathodes (such as Al or Ag) that need to be deposited using high-vacuum evaporation.[10–12]

On the other hand, research groups around the world, Mexico included, have been working on hybrid (organic-inorganic) materials with perovskite structure as the active layer in solar cells (HPSCs). Perovskite materials have attracted attention for their interesting optical and electrical properties and for its high conversion efficiency exceeding 25%, surpassing the record of copper indium CIGS solar cells and approaching that of Si solar cells. [13] The high conversion efficiencies of HPSCs were achieved over 10 years meanwhile for inorganic technologies, as the Si cells, took about 30 years. This shows how important is for research groups and industry to get a new technology for renewable energy sources based on hybrid perovskite materials. Table 1.1 shows the conversion efficiencies for several solar cells fabricated with different semiconductor materials. Although the HPSCs are not the best solar cells with the highest efficiency they are very competitive. Besides, HPSCs might be much easier to be fabricated and less expensive than other technologies.

Table 1.1 Efficiency of several PV cells to date. Data from NREL Chart, 2021 source [14]

Solar cell	Types	Efficiency (%)	Developer name
Silicon	Single crystal	26.1	ISFH(Institute for Solar Energy Research Hamelin)
	Poly-cry	23.3	FhG-ISE (Fraunhofer Institute for Solar Energy Systems)
	Thin film	21.2	Solexel
	a-Si: H	14	AIST (National Institute of Advanced Industrial Science and Technology)
	Silicon heterostructure	26.7	Kaneka (Kaneka Solar Energy)
GaAs	Single crystal	27.8	LG (LG Electronics)
	Thin-film	29.1	Alta device
CIGS		23.4	SolarFron (Solar Frontier)
CdTe		22.1	FirstSolar (First Solar Inc)
Quantum dot		18.1	UNIST (Ulsan National Institute of Science and Technology)
Dye-sensitized		13	EPFL (École Polytechnique Fédérale de Lausanne)
Organic		18.2	SJTU/BUAA (Shanghai Jiao Tong University /University of Aeronautics and Astronautics)
Perovskite		**25.5**	UIST (Ulsan National Institute of Science and Technology)

1.1 Perovskite materials in solar cells

1.1.1 Structure of perovskite

The discovery of calcium titanate ($CaTiO_3$) in 1839 by the Russian mineralogist, Gustav Rose, is considered the origin of perovskite materials. Generally, materials which have the same crystal structure of $CaTiO_3$ are referred to as perovskite materials. These perovskite materials typically have a cubic or tetragonal crystal structure with the stoichiometry of ABX_3, where A is a monovalent cation, B is a smaller metal divalent cation, and X is a halide anion (Figure 1.3). The B cations are coordinated with X anions forming octahedrons ($[BX_6]^{-4}$) that are connected each other. [15] The perovskite materials exhibit a wide range of electronic behavior including piezoelectric, thermoelectric, semiconducting, and superconducting properties depending on the specifics of material.

In hybrid perovskite material used for active layer in solar cells (HPSCs), the A cation can be ethylammonium ($CH_3CH_2NH_3^+$ =ME), methylammonium ($CH_3NH_3^+$ =MA) or formamidinium ($CH_3(NH_2)_2^+$ = FA). The B cation can be Pb_2^+, Sn_2^+, Cd_2^+, etc and X is a halide anion (I^-, Br^- or Cl^-). Several mixed cations and anions perovskite structures have been investigated. [16]

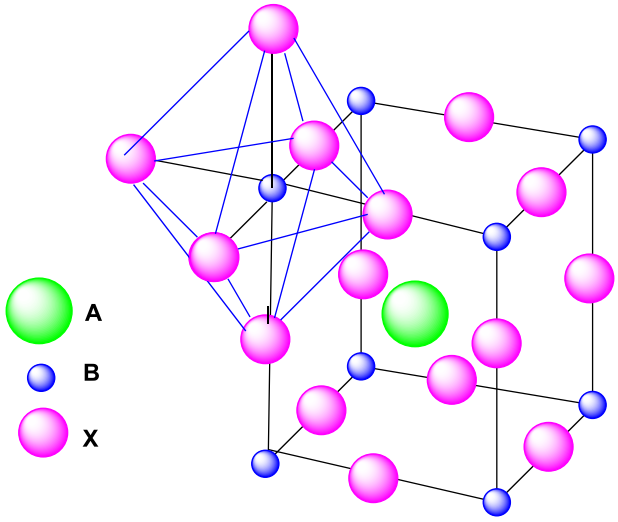

Figure 1.3 Crystal structure of perovskite ABX_3

Theoretically, the dimensionality and stability (chemical and thermal) of the crystalline structure can be predicted through the Goldschmidt's tolerance factor (t), which is given by the following equation:

$$t = \frac{r_A + r_B}{\sqrt{2}(r_B + r_X)} \qquad (1)$$

Where r_A, r_B and r_X are the effective ionic radii for A, B and X ions, respectively. An ideal cubic perovskite is expected when t = 1; while octahedral distortion is expected when t < 1. Symmetry also decreases for t < 1, which may affect electronic properties.[17] Also, depending on the relative sizes of the cation A and the octahedron, the perovskite phase can be three-dimensional (3D), two-dimensional (2D) or even one-dimensional (1D) in crystal structure.[18]

1.1.2 Optical and electrical properties perovskite materials

Hybrid perovskite materials have been tested in solar cells owing to their interesting optical and electrical properties such as: high absorption coefficient (>10^5 cm^{-1}) with wide absorption range from UV-Vis to near-infrared (NIR) , small exciton binding energy (<10 meV), long charge carrier diffusion length (~ 300 nm), [19] and direct band gap varying in a range of 1.2-2.5 eV depending on their composition or temperature. [12] For example, methylammonium triiodo plumbate, $CH_3NH_3PbI_3$ ($MAPbI_3$), which is commonly taken as reference perovskite material in HPSCs, can decreases band gap from 1.61 eV to 1.55 eV with decrease in temperature from 300 K to 150 K. [20]

As the band gap is particularly dependent to the B-X bond, it can also be tuned through composition engineering by modifying B or X, or even A which affects B-X-B bond length and angle. For instance, when in the $MAPbI_3$ perovskite the MA cation is replaced by FA cation (whose ionic sizes are 217 pm and 253 pm, respectively), the band gap decreases from 1.55 eV to 1.48 eV because the size of the A cation affects to the tolerance factor, t, and thus changes to the spacing of the $[BX6]^{-4}$ octahedron, altering the band gap. [21] Introduction of small quantities of additional cations also afford tuning of energy bands of the perovskite. The $MA_xFA_{1-x}PbI_3$ perovskite fabricated by a mixture of FA and MA (in the A site) also show shifted optical absorption (to red) with respect to $MAPbI_3$, extending solar energy absorption to the longer wavelengths thereby increasing the current density (J_{sc}) generated by devices. This mixed cation perovskite $MA_xFA_{1-x}PbI_3$ has been used to fabricate HPSCs with PCEs over 20%. [22]

The substitution of halide ions also produces shifts in the band gap of $MAPbI_3$ perovskite. The change from I to Cl or Br vary the band gap to 3.0 and 2.3 eV, respectively. The change in band gap is related to the electronic state of anions; the valence band composition changes from 3p to 4p to 5p for Cl, Br, and I, respectively. [23] The substitution of divalent cation B can also alter the band gap of the perovskite absorber. If Pb is replaced by Sn the band gap can be reduced from 1.55 eV to 1.17 eV. [21] However, the stability neither efficiency of the Sn-based HPSCs is comparable to their Pb-based HPSCs. [21]

With regard to the electric properties, hybrid perovskite materials are ambipolar charge transporters with high electron and hole mobilities on the order of ~1000 $cm^2V^{-1}s^{-1}$ (for the $MAPbI_3$ perovskite) and are characterized by having large charge carrier diffusion lengths of 100 -1000 nm that is much longer than the film thickness (~200-500 nm) that needed for get full optical absorbance. [23]

1.1.3 Perovskite solar cells efficiency evolution

The first approach for the use of perovskite materials in solar cells was the dye sensitized solar cells, where the perovskite was the absorber material deposited on porous TiO_2 layer.[17] Miyasaka et. al, reported by the first time a perovskite-DSSC in 2009 with a power conversion efficiency (PCE) of 3.8%. [24] They used $MAPbI_3$ as a light-harvesting layer. The efficiency was increased by Im et al. through the fabrication of $MAPbI_3$ quantum dots, delivering a PCE of 6.5%. [25] However, the devices presented stability problems due to the liquid electrolyte and it was replaced with a solid-state hole conductor (2,2',7,7'-Tetrakis[N,N-di(4-methoxyphenyl)amino]-9,9'-spirobifluorene = spiro-

OMeTAD). Thus, the PCE of $MAPbI_3$-based mesoscopic heterojunction configured solar cells increased to ~10%. [26] Burschka et al. in 2013 certified a HPSC with the PCE of ~15%. [27] They used a planar configured device with $MAPbI_{3-x}Cl_x$ as active layer. The introduction of chloride in the perovskite film achieved better diffusing length of charge carriers and the layer was more uniform. In recent years there has been significant progress in the conversion efficiency of HPSCs, research groups worldwide have been reporting efficiencies greater than 20%. [28–31] The highest certified efficiency to date is 25.5% (by Ulsan National Institute of Science and Technology (UNIST)).[13] Despite the certified high efficiencies of these devices, it should be noted that the most commonly reported efficiencies from research groups, even among the top groups, are in the range of 10-15% (especially for $MAPbI_3$ or $MAPbI_{3-x}Cl_x$ perovskites). [32–38] Figure.1.4 shows the PCE evolution of HPSCs to date.

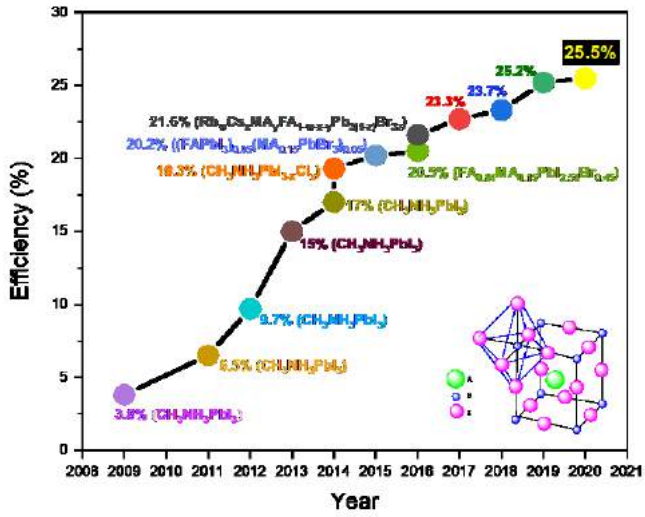

Figure 1.4 The power conversion efficiency evolution of HPSCs

1.1.4 Perovskite solar cells architecture

The HPSCs architectures can be divided into three types: the n-i-p mesoporous, n-i-p planar (direct) and p-i-n planar (inverted) architecture. The n-i-p structures are shown in Figure 1.5 (a) and (b). Analogous to inorganic thin-film solar cells, the structures are composed of a cathode, an n-type electron transport layer (ETL), an intrinsic perovskite layer, a p-type hole transport layer (HTL), and a metal anode. Due to the low exciton energy and long diffusion lengths of charge carriers, the photoexcited electrons and holes have sufficiently long lifetimes to be transported along the active layer and reach the interfaces with the charge selective layers (HTL and ETL). The n-i-p mesoporous architecture has an ETL scaffold of n-type semiconductor nanoparticles with nanoscale pores and a perovskite compact layer on top of this scaffold (Figure 1.5 (a)). In 2013, Heo et al. reported the first cell with this architecture. They used $MAPbI_3$ perovskite as active layer on a mesoporous (mp)-TiO_2 layer, the $MAPbI_3$ was deposited by one step method. Polytriarylamine (PTAA) and Au were used as HTL and electrode, respectively. Although the perovskite film had a rough and discontinuous morphology, PCE of cell was 12%, with short circuit current (J_{sc}) =16.5 mA/cm^2, open circuit voltage (V_{oc}) = 0.9 V and fill factor (FF) = 0.73. [39] By fabricating a smoother and thinner perovskite film using the two-step deposition method, Im et al. reported cells with better PCE (17%) under the same architecture. The efficiency enhancement, especially the improved J_{sc} (21.64 mA/cm^2) and V_{oc} (1.056 V) were mainly due to the formation of a dense and uniform perovskite layer. [40] To date, the highest efficiency achieved with this structure is 22.1% with V_{oc} = 1.1 V, J_{sc} =25 mA/cm^2, and FF= 0.80. [41] The n-i-p planar architecture was originated from the HPSCs but replacing the mesoporous layer, Figure 1.5 (b). In 2012, Snaith et al. reported for the first time a planar HPSCs using $MAPbI_{3-}$

$_xCl_x$, with an achieved PCE of 1.8%. The low efficiency was due to the incomplete coverage of perovskite film on the compact TiO_2 layer. [42] Although p-i-n planar devices appear to be composed of smooth and uniform films, perovskite films use to be porous and had a high density of surface defects; this has been related to a hysteresis behavior of the electrical parameters of devices. However, perovskite film morphology was improved using new film deposition techniques. [43], [44] For example, Snaith et al. employed the dual-source co-evaporation technique to evaporate lead chloride ($PbCl_2$) and methylammonium iodide (MAI) to form uniform $MAPbI_{3-x}Cl_x$ films. The device achieved a PCE 15%, with V_{oc} = 1.07 V, J_{sc} = 21.5 mA/cm^2 and FF = 0.67. [45] Owing to advances in film deposition techniques, efficiencies for n-i-p planar devices have increased to 22.54 % with V_{oc} = 1.16 V, J_{sc} =24.78 mA/cm^2, and FF= 0.78.[46]

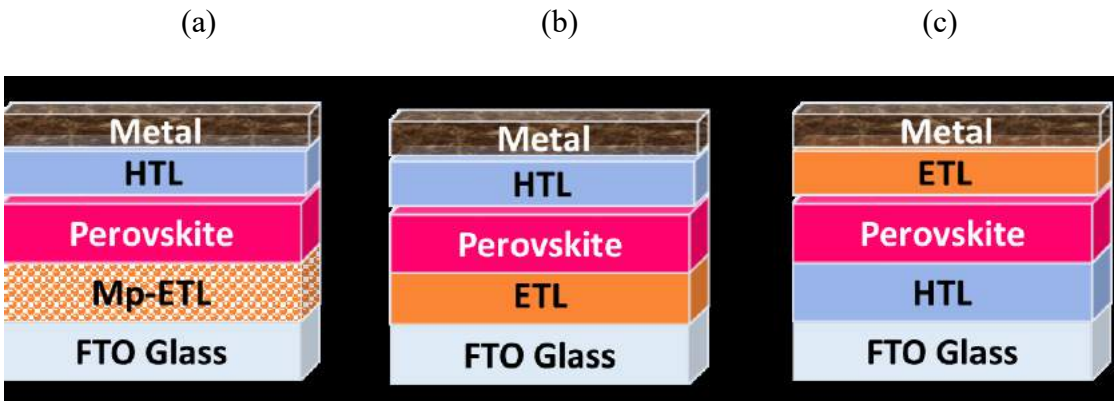

Figure 1.3 Schematics of structures typical device HPSC architectures. (a) n-i-p mesoporous, (b) n-i-p planar, and (c) p-i-n planar.

Figure 1.5 (c) shows the p-i-n architecture, also called inverted structure, since the charge carrier extraction is reversed like the organic PV devices. The p-i-n structure comprises an anode, a HTL, an intrinsic perovskite layer, an ETL, and a metal cathode. The efficiency of HPSCs in the planar p-i-n architecture has rapidly progressed. In 2013,

Snaith et al. prepared a cell with structure FTO/PEDOT:PSS/$MAPbI_{3-x}Cl_x$/$PC_{61}BM$/TiO_x/Al, where (6,6)-phenyl-C_{61}-butyric acid methyl ester ($PC_{61}BM$) and polypolystyrene sulfonate (PEDOT:PSS) were used as ETL and HTL, respectively. The efficiency reported for this configuration was of 9.8%. [47] In 2014, $PC_{61}BM$ was replaced with (6,6)-phenyl-C_{71}-butyric acid methyl ester ($PC_{71}BM$) layer. The device exhibited a PCE of 12.2% with a better photocurrent and fill factor compared to the $PC_{61}BM$. The device with $PC_{71}BM$ had a better spectral response in the visible region and a better planar junction with the cathode than the $PC_{61}BM$. [48] Recently, highest efficiency achieved with this structure is 22.34%.[49]

Transparent conductive oxides (TCO), including fluorine-doped tin dioxide (FTO) and indium tin oxide (ITO), with high optical transmittance and low electrical resistivity, are widely used in HPSCs. Overall, the conductivity of FTO is better than ITO and also for the electrical properties of ITO can be degraded in presence of oxygen at relatively high temperature (i.e. around 500 °C), while FTO is much more stable in such conditions. [32]

1.2 The fabrication of perovskite films.

The notable improvement in efficiency of HPSCs is mainly related with materials and properties of the active layer such as composition, [50] crystallinity, [51–53] and morphology, [25–28] which are also related to the deposition method. There are several methods employed for deposition of perovskite films, for instance one-step spin-coating, [25], [57-58] two-step spin-coating, [59-60] co-evaporation [61] or vapor-assisted solution method. [62] Appropriate control and full understanding of these methods are necessary to obtain high quality perovskite films, i.e., films with uniform and

homogeneous morphology (with compact grains, pinhole-free, low roughness, adequate thickness, etc), pure crystalline phase and suitable interface properties.

Two of the most used methods to fabricate films are the one and two step by spin-coating. For the one-step deposition method, the precursor solution is prepared by dissolving organic halide MAX and metal halide PbX_2 in an aprotic polar solvent, such as γ-butyrolactone (GBL), dimethyl formamide (DMF), dimethyl sulfoxide (DMSO), N-2-methyl pyrrolidone, or a mixture of them. Then, the precursor solution is spin-coated on a substrate. The wet film is dry to reach supersaturation followed by nucleation and growth of perovskite microcrystals. Finally, the substrate is exposed to thermal annealing to complete the film growth (see Figure 1.6 (a)).

In two-step deposition, two possible routes are commonly reported: (i) independent solutions of metal halide PbX_2 and halide MAX is prepared and sequentially deposited (first PbX_2 and then MAX on top), followed by annealing for a suitable conversion of the blend into perovskite ($MAPbX_3$) (see Figure 1.6 (b)); (ii) first, PbX_2 film is deposited on the substrate by spin-coating; then, the film is immersed in a MAX solution, usually prepared with isopropyl alcohol (IPA) as a solvent. Afterward, the film is dried by spin-coating method and then is annealed (see Figure 1.6 (c)).

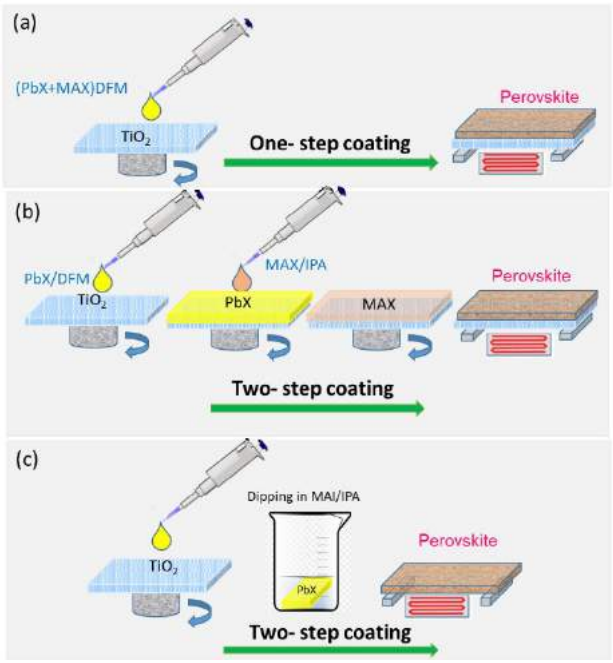

Figure 1.4 Diagram of various methods used to prepare perovskite layer.

For both methods have been reported that environmental conditions (e.g., oxygen and humidity), [63] the substrate type, molar composition of solutions, [44] solvents, [23] annealing temperature/time, [37], [64] additives [65–67] and spin-coating speed/time [15] are important processing parameters that influence the quality of perovskite films. In the following section we will discuss general mechanisms of perovskite film formation as well as the most important contributions in both deposit methods under analysis to get high-quality perovskite films and good reproducibility of films.

1.3 State of the art films deposition for solar cell devices

1.3.1 One-step method

The one-step spin-coating method is generally used to fabricate perovskite films due to the fast and easy processing. Overall, stoichiometry between PbX_2:MAX and solvent are

some fundamental parameters to be considered to achieve quality films. Commonly reported stoichiometry values are 1:1 or 1:3 (molar ratio) and GBL, DMF, DMSO, or their mixtures using solvents for precursor solution. Im et al. first reported perovskite films deposited from a solution of MAI and PbI_2 (1:1 molar ratio) dissolved in GBL. The solution was deposited on a mesoporous structure of TiO_2 to form a $MAPbI_3$ film. $MAPbI_3$ film had several micrometer-sized islands and the cell showed an efficiency of 6.54%. [25] Later, Dualeh et al. fabricated a $MAPbI_{3-x}Cl_x$ film from a $PbCl_2$ and MAI solution in DMF; this film was used as the active layer in an HPSC that reached a PCE = 11.66%. [56] The molar ratio for the solution was 1:3 ($PbCl_2$:MAI); with any deviation in the stoichiometry (excess of MAI or $PbCl_2$) affected the quality perovskite film as well as photovoltaic performance of the devices. Contrary to the previous work, they used DMF as a solvent and informed that DMF coordinates better with lead halide creating an intermediate phase during film fabrication, which modulated the growth of the grains, improving the film morphology homogeneity and crystallinity. DMSO or the mixture of DMSO/GBL, DMSO/DMF or DMF/GBL have also been used to prepare the precursor solutions, with these solvents denser perovskite films have been obtained. For example, H.-B. Kim et al. observed that the DMF / GBL mixture produced more uniform perovskite films with grain sizes ~100 nm and smoother (RSM = 6.6 nm) as contrasted to films fabricated from solutions with only DMF or GBL which exhibited morphologies with higher roughness and various pinholes. The morphological characteristics of the films from the DMF / GBL mixture improved the interfacial contact with the charge transport layers and the device performance was higher. [68]

On the other hand, it has been found that the lack of control in the drying process for the one-step method leads to perovskite films with dendritic structures, i.e., non-continuous

films with low surface coverage. [69]. To solve this problem, some chemical and physical approaches have been used to promote the supersaturation into the film, improving the control in the nucleation and the uniform growth of the grains. [69]

Chemical approaches

For the chemical approaches, excess methyl anthranilate (MA)-salts, chloride derivative additives [70–72] and other Lewis bases as additives have been used. [73] For example, Liang et al. added 1% of 1,8-diiodooctane (DIO) into a perovskite precursor solution of $MAPbI_{3-x}Cl_x$. DIO increased the solubility of $PbCl_2$ and was able to temporarily coordinate with Pb_2^+ during crystal growth; modulating crystallization kinetics which led to a smoother perovskite morphology with a surface coverage of ~90%. With these films HPSCs were fabricated and the device with DIO improved efficiency from 9% up to 11.8%. Chloride derivative additives such as Methylammonium chloride=MACl and ammonium chloride = NH_4Cl, [70–72] as well as hydrophilic acids such as HCl, HBr and HI, [25] into a perovskite precursor solution can also modulate crystallization kinetics. These additives form intermediate phases that slow down the nucleation and crystal growth processes. With better control of the crystallization process, the films adopt morphologies with low roughness and few pinholes; the photovoltaic devices achieve efficiencies around 10%.

Physical approaches

For physical approaches, thermal annealing, [74-75] gas flow, [76-78] vacuum drying, [18] additive engineering, [65–67] or combinations of these have been used to control the perovskite film morphology. Dualeh et al. found that annealing temperature has an

impact on $MAPbI_3$ perovskite film morphology, which in turn was correlated with the efficiency of the solar cell. [74] The temperature range studied was from room temperature to 200 ºC. The sample annealed at 60 ºC did not form a homogeneous film; rather large islands of precursor material was detected. As the annealing temperature was increased to 80 ºC and 100 ºC, the films showed a coverage much higher and the shape of the individual grains was better defined. While samples annealed at temperatures above 120 ºC exhibited larger sized islands but these were not interconnected. The changes in morphology were related to the conversion rate as observed in their XRD studies. The best efficiency was 11.66% using the $MAPbI_3$ film treated at 100 ºC.

The flow of certain gases and additive engineering can also generate a control on morphology perovskite film. For example, methylamine (CH_3NH_2) gas has been shown to enhance the solubility of MAI and PbI_2 in solvents. With an improved solubility, the solvent can evaporate rapidly during the spin-coating of the perovskite precursor solution, facilitating rapid crystallization of the perovskite at room temperature. With this technical, perovskite films presented an uniform morphology free of pinholes with grain size of about 0.8-1.0 μm and the devices achieved a PCE 12.1% in large-area (36.1 cm^2) in solar module. [77]

With regard to additive engineering, the use of anti-solvents are very common to reduce the solubility of perovskite precursors in the solution, thus promoting nucleation and fast crystal growth on the film to produce very uniform and compact films. The anti-solvents such as toluene, chlorobenzene, benzene, etc., have been widely used in the fabrication of perovskite films. Jeon et al. et al. [65] were the first to report on the use of anti-solvent in perovskite films. They use toluene droplets at the first seconds of the spin procedure.

During centrifugation, toluene rapidly led to the supersaturation by helping to fast evaporation of DMF. Compact perovskite films with grain sizes in the range 100-500 nm were obtained, and HPSCs showed PCEs close to 15%. Simultaneously, Xiao et al. studied the effect of chlorobenzene on perovskite film morphology. [66] After spin-coating, the wet film was immediately exposed to chlorobenzene to induce fast crystallization. This resulted a highly compact film with polygon grain (micrometer-sized); the application of these films in HPSCs led to an average PCE of 13.9%.

Although anti-solvents have been widely used in the fabrication of perovskite films, some authors such as J. Ye et al. and B. Li et al. [79-80] reported that the inappropriate use (solvent type, volume, deposition time, etc.) affect the quality and reproducibility of the perovskite films; uncontrollable inhomogeneous nucleation process could occur and lead to uneven film. Moreover, the use anti-solvent is still a challenge to implement for a scalable deposition.[81]

1.3.2 Two-step method

Burschaka et al. reported the first time the two-step deposit method in HPSCs fabrication. They prepared $MAPbI_3$ films by depositing PbI_2 onto a nanoporous TiO_2 film and subsequently it was transformed into perovskite by exposing it to a solution of CH_3NH_3I (MAI). The resultant morphology of the perovskite was cuboidal with better coverage compared to a one-step process. The devices fabricated by two-step process showed an efficiency of 15%. [60] Later, Im et al. investigated the relationship between cuboidal size of grains perovskite and the MAI concentration. [40] They found that grains size of $MAPbI_3$ decreased with increasing concentration. The average cuboid size was

determined to be ~720 nm for 0.038 M, ~360 nm for 0.044 M, ~190 nm for 0.050 M, ~130 nm for 0.057 M and ~90 nm for 0.063 M. Photovoltaic parameters were also significantly dependent on MAI concentration because of the difference in crystal size of the $MAPbI_3$. The highest PCE (17.01%) was achieved with 0.038 M sample. Compared with the one-step deposition method, the two-step method is more tolerant of wet environments, for example, Grätzel's group showed that a small amount of H_2O in the organic halide solution could help uniform grain growth of perovskite films and achieved an efficiency of 20%. [82]

The two-step deposition method was also applied to planar architectures. The $MAPbI_3$ film formed fiber-shaped grains with large pinholes and poor coverage which led to higher charge carrier recombination and leakage current. [83] The latter also occurred when the grain size of the perovskite was increased, which was attributed to an increase in the surface roughness of the films. [83] Other studies showed incomplete conversion of PbI_2 to $MAPbI_3$ films, so that structures with mesoporous scaffolds are more effective to facilitate faster reaction between PbI_2 and organic halide. [64] However, the long reaction time and the use of the mesoporous layer have limited the ability to scale up the film in the two-step deposit method. Numerous studies have been designed to advance understanding of film formation by two-step method on mesoporous scaffolds and planar structures. The strategies also include the chemical and physical approaches indicated in section 1.3.1.

1.4 Purposes of this work

Although strategies to improve perovskite film quality have been extensively used (mainly through above deposit methods), the truth is that reproducibility is far away to be a reality for mass production, even for small areas (0.1 cm^2) reproducibility is not possible at all.[84] Low reproducibility is the main obstacle to bring this technology to the market. The main challenge for reproducibility is to maintain the quality of the perovskite layer in the entire deposit area. Few authors have addressed this problem, for example Angmo et al. recently reported that reproducibility of perovskite films is related to thermodynamic and kinetic factors that influence how the perovskite film crystallizes.[84] These authors compare two crystallization mechanisms: the nucleation mechanism (ND) and the crystal growth mechanism (CGD). The films formed through these mechanisms showed different microstructural properties in morphology. The main differences depended on the rate of concentration and the degree of the reached supersaturation. For the ND mechanism, films presented better homogeneity (entire substrate) with the use of ethyl acetate as an anti-solvent; also showed higher average efficiency (13.54 ± 0.80%). The PCE thus reported, show good reproducibility of devices, which was correlated to the good reproducibility of the perovskite films. Simultaneously, Li's group developed a spontaneous supersaturated nucleation strategy to fabricate high-quality and reproducible perovskite films without the use of anti-solvents.[80] They proposed a strategy using strong coordination Lewis base additives and weak coordination volatile solvents to fabricate perovskite films. The devices showed a PCE of 13.13% in large areas (100 cm^2).

As noted above, the notable improvement in the efficiency of HPSCs is mainly related to the quality of perovskite films, which in turn is correlated to the deposition method.

Reproducibility is very important, however, it does not occur from one laboratory to another even between very experienced groups.[85] This has led to apparently contradictory results and caused confusion among research groups all over the world. We believe that the lack of reproducibility is partly related to the fact that some important processes within the active material are not yet fully understood. To help to solve this problem, this research work aims to compare one and two-step deposition techniques to find out the main experimental parameters involve in both methodologies that might affect the quality and reproducibility of perovskite films. Therefore, the morphology, roughness, grain size, crystallinity and absorption of the films were analyzed and correlated with the features of each technique, i.e., one-step, by spin-coating, and two-step, by spin-coating and close-space sublimation. The perovskite films were used as the active layer in HPSCs with inverted architecture. Worthy to add is the poor physical contact observed at the ETL/FM interface, not affected the performance of the fabricated devices. It is reported that this fact does not affect the reported efficiencies of the devices as much as the quality of the perovskite films.

After this introductory chapter, experimental procedures follows as chapter 2 where material and the one and two steps methods are described together with the film and device characterizations. Chapter 3 reports results and an experimental discussion based on the identified parameters. The analysis and discussion of the reported results between both used methodologies is given in chapter 4. The conclusions and perspectives of this work are reported in Chapter 5.

2. Experimental procedure

In this chapter, the methodology for the fabrication of $MAPbI_3$ perovskite films using the one-step by spin coating and two-step by spin coating and close-space sublimation, is presented. The characterization was carried out using atomic force spectroscopy (AFM), X-ray diffraction (XRD) and UV-visible spectroscopy (UV-Vis).

2.1 Materials

A commercial ink was used from Ossila Ltda. The ink is based on a mixture of methyl amine iodide (CH_3NH_3I=MAI) and lead chloride II ($PbCl_2$) in a molar ratio of ($PbCl_2$: MAI) of 1:3 with N, N - dimethylformamide (DMF) as solvent. MAI was also obtained from Ossila Ltda, lead iodide II (PbI_2) and $PC_{71}BM$ were purchased from American Dye Source. PEDOT:PSS (Clevios PVP AI4083) was got from Heraeus-Clevios. All solvents as: DMF, DMSO, ethanol and chlorobenzene (CB) were acquired from Sigma Aldrich. As substrate-device ITO/glass with 10-15 Ω/square was acquired from Delta Technologies. As cathodes Ca/Ag and Field's metal (FM) were used, they were acquired from Aldrich and Rotometals, respectively. The FM is an eutectic alloy that has been previously used by our group [10-11] and it is made up of 32.5% Bi, 51% In, and 16.5% Sn by weight, it has a melting point above 62 ºC, and can be deposited through drop casting at low temperature (~95 ºC).

2.2 The $MAPbI_3$ perovskite film preparation.

The $MAPbI_3$ perovskite films were produced in three different deposition methods one-step by spin-coating and two-steps by close-space sublimation and spin-coating with sequential deposition. For the one-step deposit method, several batches of $MAPbI_3$ perovskite films were prepared from one solution containing MAI, PbI_2, DMSO and DMF and one a batch of commercial ink. The molar ratios were (MAI: PbI_2: DMSO) of 1:1:1 diluted in 1 ml of DMF and ($PbCl_2$: MAI) of 1:3 diluted in DMF and were used to each ink. We assign them as ink-1 and ink-2 respectively.

Below is a detailed description of the methods used to produce each perovskite film using different deposition methods.

2.2.1 One-step deposition process using the spin-coating technique.

For the one-step deposit method, two precursor solutions (hereafter called inks) were used. The first solution was prepared by mixing the precursors MAI, PbI_2, and DMSO, the molar ratio was 1:1:1 (MAI: PbI_2: DMSO) diluted in 1 ml of DMF (**ink-1**). A second solution was a commercial ink composed of $PbCl_2$ and MAI molar ratio 1:3 diluted in DMF (**ink-2**). Several batches of $MAPbI_3$ perovskite films were prepared from each one solution.

For the deposition of $MAPbI_3$ perovskite films, glass/ITO of dimensions 1.5 x 1.5 cm^2 was used as substrate. Before being used, substrates were cleaned with ethanol in an ultrasonic bath and rubbed with alcohol-wetted cotton, then were dried at 80 ºC for 12 h;

the final cleaning step was a 10 min UV oxygen plasma treatment. Previous to the deposition of perovskite film, the substrates were covered with a thin layer of poly (3,4-ethylene dioxythiophene) polystyrene sulfonated (PEDOT:PSS) deposited at 5000 rpm for 1 min by spin-coating. The PEDOT:PSS films were thermally annealed at 120 ºC for 20 min. The substrates were transferred to a glove box with an N_2 atmosphere where the perovskite inks were deposited by the conventional one-step method. (see Figure 1.6 (a)). To cover the total area of the substrates, 30 µl of the corresponding precursor ink was used, the spin-coating speed was set at 4000 rpm, the spin time was 20 s (for ink-1) and 60 s (for ink-2). For the procedure with anti-solvent, 100 µl of chlorobenzene was added in the first seconds of the spin process. Finally, the substrates were annealed at 100 ºC by 2 min for the ink-1 and 80 ºC for 60 min for the ink-2.

2.2.2 Two-step deposition process using the close-space sublimation technique.

For the fabrication of the $MAPbI_3$ perovskite films by the close-space sublimation method, the procedure is shown in Figure 2.1. First the organic and inorganic materials were deposited separately, and then organic material was sublimated on the inorganic one to achieve the conversion to perovskite. Before preparing the solutions, the precursors (PbI_2 and MAI) were dried at 60 ºC for 24 h in a vacuum oven at -0.4 bar.

Inorganic film:

The PbI_2 film was deposited by spin coating from a solution with DMF as the solvent and a concentration of 300 mg/ml. 100 µl of the PbI_2 solution was filtered out and deposited

on the substrate (covered with the PEDOT:PSS film) at 3000 rpm for 1 min and annealed at 60 ºC for 24 h in a vacuum oven at -0.4 bar. Before the deposition, both the solution and the substrate were heated; different temperatures were used: ambient, 40 ºC, 60 ºC, 80 ºC, 100 ºC and 120 ºC, and its effect on the morphology of the films was studied.

Organic film:

For deposition of MAI film, 30 mg of this compound were solved in 1 ml of ethanol. A glass substrate (pre-treated with oxygen plasma) was used for film deposition. The substrate was placed on a hot plate at 60 ºC for 10 min, and then 100 µl of the MAI solution was drip deposited. It waited for the solvent evaporation, and the film was placed at 60 ºC in a vacuum oven at -0.4 bar for 24 h to ensure a completely dry.

$MAPbI_3$ perovskite film:

Using the close-space sublimation technique, the $MAPbI_3$ perovskite film was fabricated. The PbI_2 and MAI films were placed face to face, with a separation of 1 mm, in a vacuum oven at 130 ºC for 60 min at -0.8 bar (relative pressure). When the PbI_2 film changed color (from yellow to brown), a thermal post-treatment was given at 110 ºC for 60 min at -0.4 bar vacuum. The procedure has schemed in Figure 2.1.

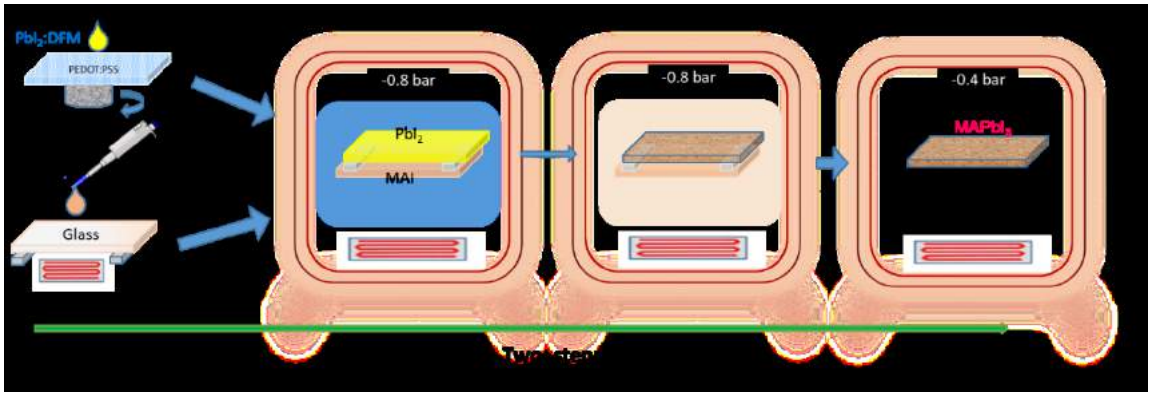

Figure 2.1 Diagram of close-space sublimation method used to prepare perovskite layer

2.2.3 Two-step deposition process using the spin-coating technique.

The two-step method for deposition of $MAPbI_3$ perovskite films is shown in Figure1.6 (b). A PbI_2 film was deposited by spin-coating from a solution with a 300 mg/ml concentration and with DMF as the solvent. 80 µl of PbI_2 solution was filtered out and dropped onto the PEDOT:PSS film and spin-coated at 3000 rpm for 30 s followed by annealing at 140 ºC by 30 min in a vacuum oven (-0.4 bar). Before the deposition of PbI_2, the solution and substrate were kept on a hot plate at 100 ºC for 15 min. In the second step, 100 µl of MAI in ethanol solution (30 mg/ml) was poured over the PbI_2 film, the solution remains onto film 15, 20, and 25 s before centrifugation began. Then spin-coated at 3000 rpm for 10 s followed by annealing at 100 ºC between 15 and 120 min in a vacuum oven (-0.8 bar).

2.3 Film characterization techniques

Film characterization by AFM and SEM:

An AFM Easyscan2 from Nanosurf was used to measure the thickness and study the morphology of the films. The AFM is an instrument mechano-optical capable of detecting forces of Femtonewtons order. The morphology of the samples was also analyzed with scanning electron microscopy (SEM), images were acquired with a Jeol JSM 7800F electron microscope.

Film characterization by X-Ray:

In this work, X-ray diffraction (XRD) pattern generation was carried out with Bruker D2 PHASER. The diffractometer was configured with Cu Kα radiation source (wavelength of 1.5418 A), 10 kV and 5 mA. Samples were analyzed with an angle sweep of 10-60º with a standard increase of 0.02º. The technique was used to verify the crystalline phase of the films.

Film characterization by UV-visible spectroscopy (UV-Vis)

The Perkin Elmer spectrophotometer model Lambda 900 was used. This equipment has a double beam optical system and double monochromator with tungsten halogen (VIS/NIR) and deuterium (UV) sources. It was used to know the absorption spectra of the films. The spectra were taken in a range of 400 to 1000 nm.

2.4 Device fabrication and characterization

Figure 2.2 shows the schematic representation of the fabricated devices with architecture glass/ITO/PEDOT:PSS/$MAPbI_3$/$PC_{71}BM$/FM. The PEDOT:PSS and the $PC_{71}BM$ were used as hole and electron transport layers, respectively. PEDOT:PSS was deposited as mentioned in section 2.2.1 and $PC_{71}BM$ was deposited onto perovskite film at 1000 rpm for 30 s by spin-coating in a N_2 atmosphere. As a cathode, Field's metal (FM) was used and deposited by drop casting technical on a hot plate at 85 ºC in normal room atmosphere without any other special condition. The device active area was 0.07 cm^2, this was delimited with tape mask and then a small amount of FM was melted and dropped on top of the device. For the evaporated cathode, 50 nm of Ca and 100 nm of Ag were deposited by thermal evaporation at a pressure of 2×10^{-6} torr (active area: 0.09 cm^2).

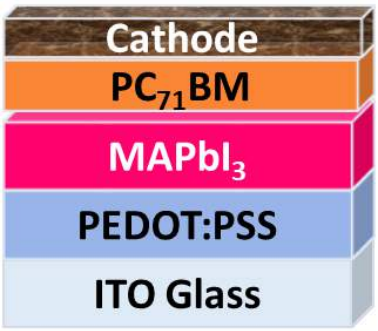

Figure 2.2 Schematic representation of perovskite devices.

Device Characterization

To estimate the power conversion efficiency (PCE) of solar cells it is necessary to obtain the characteristic current-voltage curve under standard AM1.5 illumination, this corresponds to the sun angle with the zenith of 48.2º and the integrated irradiance is 1000

W/m^2 =100 mW/cm^2. For device characterization, a solar simulator Sciencetech SS150 (AAA type) was used, light intensity was calibrated at 100 mW/cm^2 using an Oriel reference cell. Characteristic J-V curves were recorded with a sourcemeter Keithley 2450. Once the J-V curve was measured, the short circuit current (J_{sc}) and the open circuit voltage (V_{oc}) were obtained directly from the intersections of the electrical characteristic with the vertical and horizontal axes, respectively, and therefore, the PCE value could be estimated (see Figure 2.3).

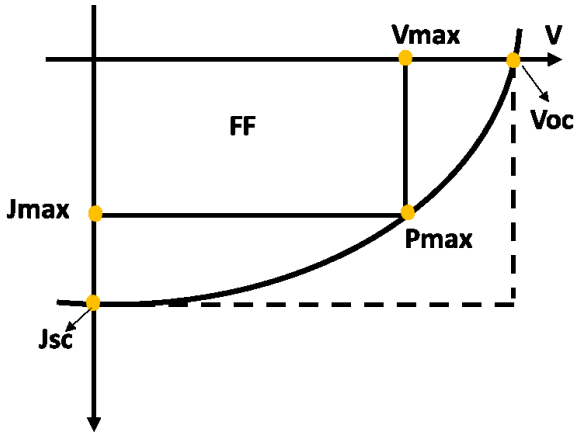

Figure 2.3 J-V curve of solar cell.

The cell delivers power in the range bias from 0 to V_{oc}, the cell achieves a maximum power point (P_{max}) at some voltage V_{max} and a corresponding current density J_{max}. With these values together with J_{sc} and V_{oc} it is possible to calculate the fill factor (FF). The FF describes the rectangle of J-V curve which shown in Figure 2.3 and is given by the following equation:

$$FF = \frac{J_{max}V_{max}}{J_{sc}V_{oc}} \qquad (2.1)$$

PCE of solar cells can be calculated by means of equation:

$$\text{PCE} = FF\,\frac{V_{oc}J_{sc}}{P_{in}} \qquad (2.2)$$

Where P_{in} have a value of 100 mW/cm^2 under AM1.5 standard.

3. Results and experimental discussion.

The results about deposition and characterization of fabricated $MAPbI_3$ perovskite films by the one-step and the two-step deposition methods described above are presented. Characterization was conducted by XRD, UV-Vis absorption, and morphological analyses. The influence of deposition technique parameters such as anti-solvent washing, annealing temperature, temperature for deposition of the inorganic film and, the time that the MAI-solution remains onto the PbI_2 film before the spin process began on the homogeneity, crystallinity, and reproducibility of perovskite films were studied. Besides, the influence of such parameters on the photovoltaic performance of perovskite solar cells is presented. J-V plots were acquired and efficiency was determined.

3.1 Results for one-step method

3.1.1 Chlorobenzene dripping on perovskite films deposited by the one-step method.

The dripping of anti-solvent, such as chlorobenzene (CB), during the spin-process in the one-step deposition method of perovskite films, has been widely used; this approach has shown an acceleration of perovskite film crystallization that leads to the formation of a uniform film with high surface coverage.[66], [86-87] Furthermore, it has been reported that the quality film obtained largely depends on the rate of dispersion of the anti-solvent [48]. Nevertheless, other parameters that would impact the preparation of perovskite films

to achieve reproducibility are not really pointed out in most works; for instance, the volume of anti-solvent and the right time for dispensing it.

For our case, chlorobenzene was used as anti-solvent, and it was dropped on the perovskite film at different times along the spin process to analyze the effect on crystallinity, optical absorption, and morphology. Deposition of perovskite ink was performed as mentioned in section 2.2.1. Ink-1 with molar ratio MAI: PbI_2: DMSO of 1:1:1 solved in 1 ml of DMF was used to produce films by one-step deposition. 100 µl of CB were dispensed on the film at 0 s and after 5, 10, 15, and 20 s of centrifugation process begun. A pristine film (without CB washing out) was used as a reference. The samples were fabricated in a glove box (N_2 atmosphere).

In Figure 3.1, photographs of $MAPbI_3$ films with and without CB-washing and annealed at 100 ºC by 2 min are shown. The pristine film is homogeneous and completely opaque with a grey color as shown in Figure 3.1 (a); meanwhile Figure 3.1 (b) shows the CB-washed film. The CB was dropped just at the beginning of the centrifugation process, i.e., at 0 s. Photographs of the samples with CB dispensed at 5, 10, 15, and 20 s after the centrifugation begun are shown in Figures 3.1(c-f), respectively. These films exhibited changes in color and appearance (films with low or high opacity). The film washed at 0 s is less opaque than the pristine film; besides, it exhibits irregular areas with bright and haziness spots marked with pink circles, Figure 3.1 (b). The film washed at 5 s, dark brown color, and highly reflective was observed (Figure 3.1 (c)); these features indicate homogeneous and smooth surface $MAPbI_3$. For the rest of the samples, the CB-washed conducted to a major opacity and irregular areas in the films (Figure 3.1(d-f)).

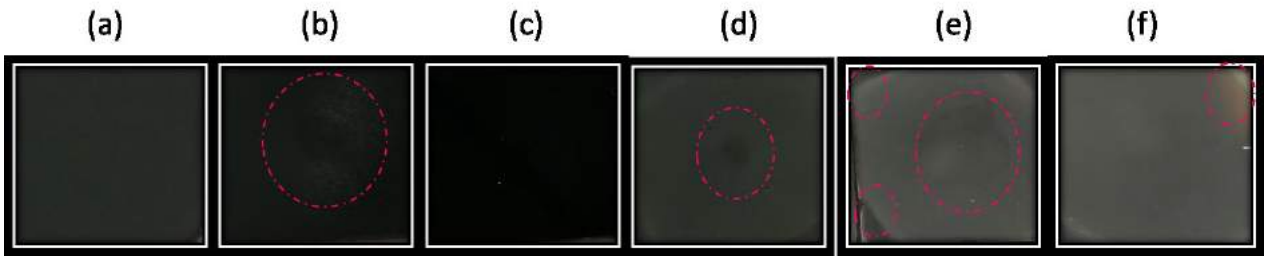

Figure 3.1 Photographs of perovskite films prepared by the one-step method. (a) Pristine (Without CB washing) and with CB washing at different times: at the beginning (b) 0 s, after (c) 5 s, (d) 10 s, (e) 15 s, (e) 20 s from the start of the spin-coating process.

3.1.1.1 Crystallinity

The perovskite films were analyzed by XRD (see Figure 3.2). The XRD pattern for the pristine film showed peaks at 2θ=14.2º, 19.9º, 23.5º 24.7º, 28.6º, 31.7º, 35.1º, 40.8º, 43.3º, and 50.5º. These peaks were assigned to planes with Miller indices (110), (112), (121), (022), (220), (222), (132), (040), (330), and (044), respectively (Figure 3.2a). The diffractogram indicates the formation of the tetragonal phase (*I4/mcm* space group) in the $MAPbI_3$ perovskite layer. The assignation of the peaks was done according to the interplanar spacing equation for a tetragonal unit cell: [88]

$$\frac{1}{d^2} = \left(h^2 + \frac{k^2}{a^2}\right) + \frac{l^2}{c^2}, \qquad (3.1)$$

where *h, k* and *l* are the miller indices, *d* is interplanar spacing, *a* and *c* are the lattice constant of the unit cell. The lattice constant for tetragonal phase of $MAPbI_3$: $a\ (\text{Å}) = b = 8.8392$, $c\ (\text{Å}) = 12.6948$, α=γ=β= 90º according to the JCPDS (Joint Committee on Powder Diffraction Standards) card Nº4124388.[89]

The XRD pattern for the washed films showed the same diffraction peaks. Only the film where CB was dispensed at 5 s showed a slight increase in the intensity of the peaks which could indicate a higher crystallinity. The main increasing in intensity peaks at 14.2º and 28.6º (Figure 3.2a, blue diffractogram); the increase in the intensity of these peaks may be related to the more homogeneous nucleation and modulated growth kinetics during crystallization.[90]

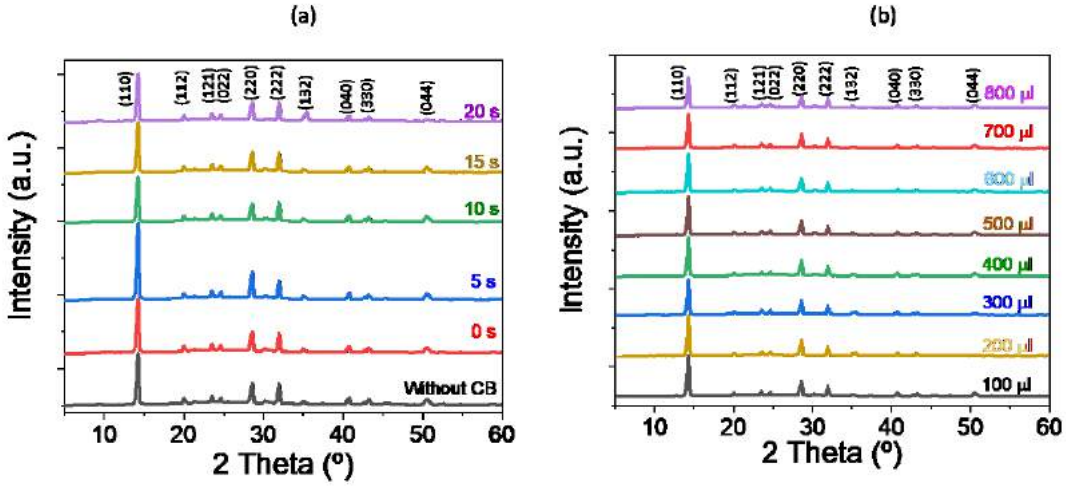

Figure 3.2 XRD of perovskite films prepared by one-step method: (a) without and with chlorobenzene washing at different times. (b) Treated with different volumes of CB after post-annealing.

According to the last two results, when chlorobenzene is dispended at 5 s after the spin process began, a more homogeneous and crystalline film is obtained. Therefore, this time was fixed, and a different volume of CB was dispensed. Figure 3.2 (b) shows the XRD pattern for films washed with different volumes of CB. The XRD patterns for these films show the same diffraction peaks. Their intensity is rather similar, indicating that the volume of CB does not induce polymorphism or variation of the crystalline structure.

These results agree with the work of Xiao M et al., where regardless of the used volume of anti-solvent the perovskite was effectively formed [91].

The full width at half maximum (FWHM) was calculated for each peak of XRD pattern. The values are relatively constant regardless of whether the film was washed with or without chlorobenzene; this also occurs even when the amount of anti-solvent is varied. The values are showed in Table 3.1. The grain size calculated from the patterns are in the range of 27-31 nm; these values are consistent with previous reports. [39] The average grain size was estimated using Sherrer's equation ($D = K\lambda/\text{FWHM}, \text{where } K = 0.09 \text{ and } \lambda = 0.15406\ nm$). [88]

Table 3.1 FWHM and grain size of perovskite films calculated from XRD patterns

Sample	Without CB	0 s	5 s	10 s	15 s	20 s
FWHM (rad)	0.33	0.32	0.31	0.38	0.38	0.32
Grain size (nm)	29	30	31	27	27	30

3.1.1.2 Absorption

Figure 3.3 (a) shows the absorption spectra of perovskite films, pristine and washed with chlorobenzene (CB dispensed at different spin-process times). The absorption spectra cover the whole visible spectrum; the absorption edge for all films starts at 790 nm. Figure 3.3 (b) shows the Tauc´s plot for the absorbance that indicates bandgap energy of ~1.58 eV. The peak at 750 nm has been used to compare the intensity of absorption between different films; the pristine one has lower absorption than the washed films. The film with the higher absorption corresponds to the washed at 5 s (blue line). A higher intensity of

absorption can be related to a complete transformation of precursors into perovskite material.

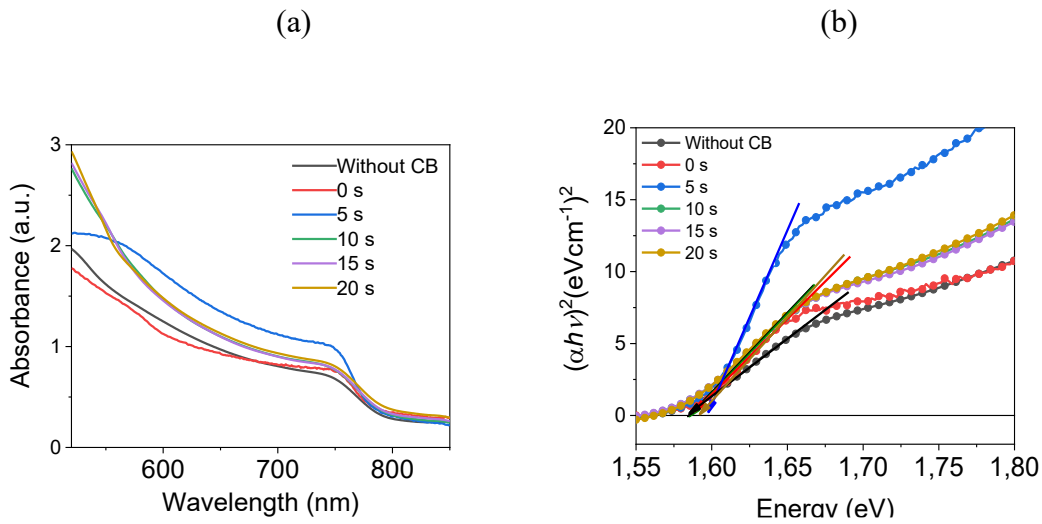

Figure 3.3 (a) UV-Vis absorption and (b) Tauc´s plot for perovskite films prepared by one-step method without and with chlorobenzene washing at different times.

Films washed at 10, 15, and 20 s exhibit similar absorption spectra but of lower intensity than the 5 s film. This decrease of the absorbance can be related to the non-homogenous transformation of precursors into perovskite that, in turn, can be observed in the opacity and irregular areas on the film surface.

On the other hand, it is noticed from Figure 3.4 that the absorption spectra of the perovskite films washed with different volumes of CB were quite similar; this confirm that the volume of chlorobenzene does not affect the optical properties of the perovskite film and agree with the XRD patterns.

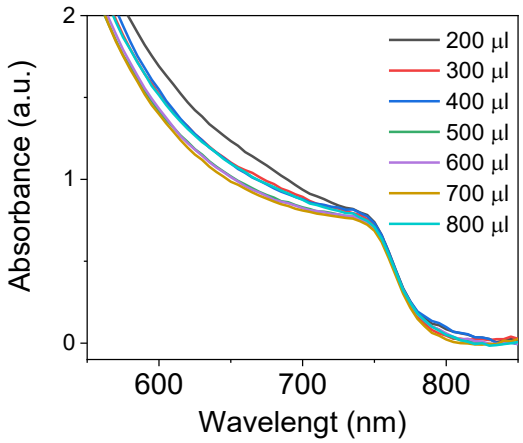

Figure 3.4 (a) UV-Vis absorption for perovskite films with different volumes of CB.

3.1.1.3 Morphology

The morphological features of perovskite films, such as homogeneity, grain size, surface coverage, thickness, etc., have an important role in the performance of the devices. To analyze the effect of washing with chlorobenzene, morphological characterization was conducted by AFM. Multiple AFM images/scans were taken at different locations of the film to check the surface morphology, and the typical images are shown in Figure 3.5. The thickness of all perovskite films is about 380-410 nm, which is consistent with previous reports where similar deposition conditions were used. [7], [56], [92]. In this case, the time for dispensing chlorobenzene has a remarkable effect on the $MAPbI_3$ films morphologies. Figure 3.5 shows the 5µm × 5µm AFM images; this revealed different morphologies and roughness for each film. The pristine film, without the addition of chlorobenzene, has an undefined grain morphology and a high roughness of 165 nm (see Figure 3.5 (a)). It is known that high roughness makes difficult the charge transfer between the device interfaces as well as induce recombination processes. [93-94] For the case of chlorobenzene dispensed at 0 s, it is observed a film with a better-defined

morphology composed of micrometric spherical grains; however, the surface roughness is high (123 nm, see Figure 3.5 (b)). The morphology of the film washed 5 s after the centrifugation exhibits compact micro-grains, ~0.25 µm, homogeneously distributed on the surface and it has few pinholes (see Figure 3.5 (c)). The average roughness was 14 nm; this morphology has been mentioned as ideal for charge transport on the perovskite layer and at the interfaces with other layers in the device.[95] The CB (anti-solvent) induces the supersaturation in the precursor solution and, therefore, fast nucleation of perovskite grains. The induced faster nucleation leads to compact grains and homogeneous film, as shown in Figures 3.1 (c) and 3.5 (c). In this regard, Xiao et al. reported that in the one-step method supersaturation could occur in the first three seconds after centrifugation begun. [49]

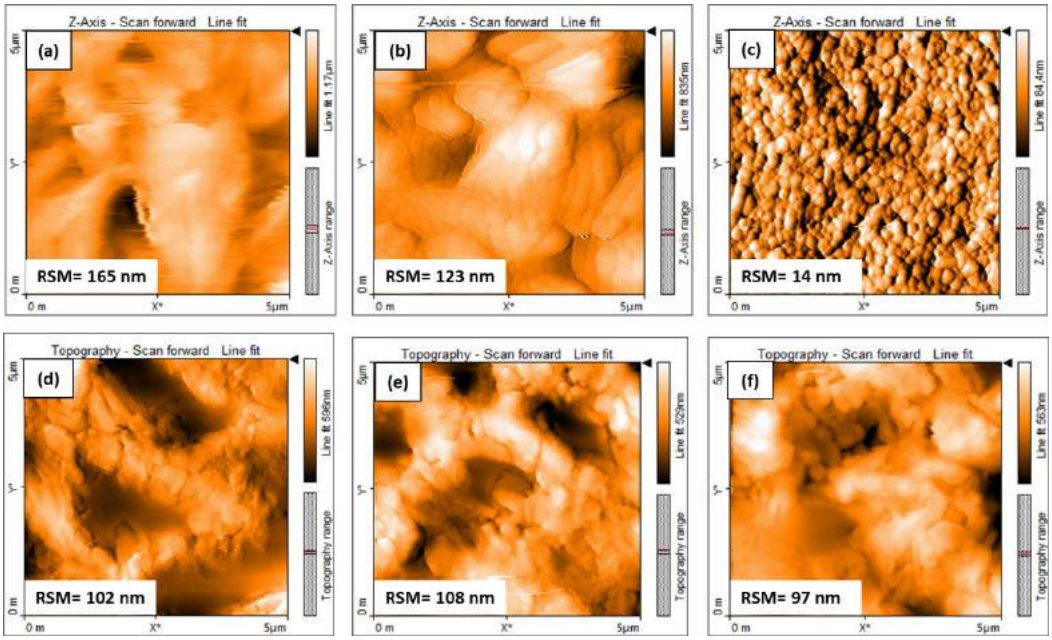

Figure 3.5 AFM of perovskite films prepared by one-step method (a) Without CB washing. CB washing at different times: before (b) 0 s and after (c) 5 s, (d) 10 s, (e) 15 s, (e) 20 s, from the start of the spin-coating process.

The morphology of the films was not homogeneous when CB was added at 10 s, 15 s, and 20 s (see Figure. 3.5 (d-f)). At each time the solvent evaporation had already begun (and therefore the nucleation), then the addition of chlorobenzene at this stage does not contribute to the control of crystallization. The AFM images do not show a defined grain morphology; the film has large pinholes and the average roughness was over 100 nm. All these defects can induce recombination processes in the devices.

According to these results, the supersaturation induced by washing with CB can help control perovskite film crystallization and morphology; however, this happens only at a specific time. Our results showed that the right time corresponds to 5 s after the centrifugation began. It was not possible with the shorter or larger times to induce a supersaturation effect and control film features; therefore, film morphology showed high roughness and undefined grains.

On the other hand, the effect of the used CB volume for washing on film morphology was also analyzed. Xiao *et al.*, pointed out that the volume could influence the supersaturation process. [91] The morphology of the sample washed with 100 µl of chlorobenzene was described above and corresponds to micrograph shown in the Figure 3.5 (c). While AFM images of perovskite films washed with 200, 300, 400, 500, 700, and 800 µl of CB are shown in Figure 3.6 (a-f).

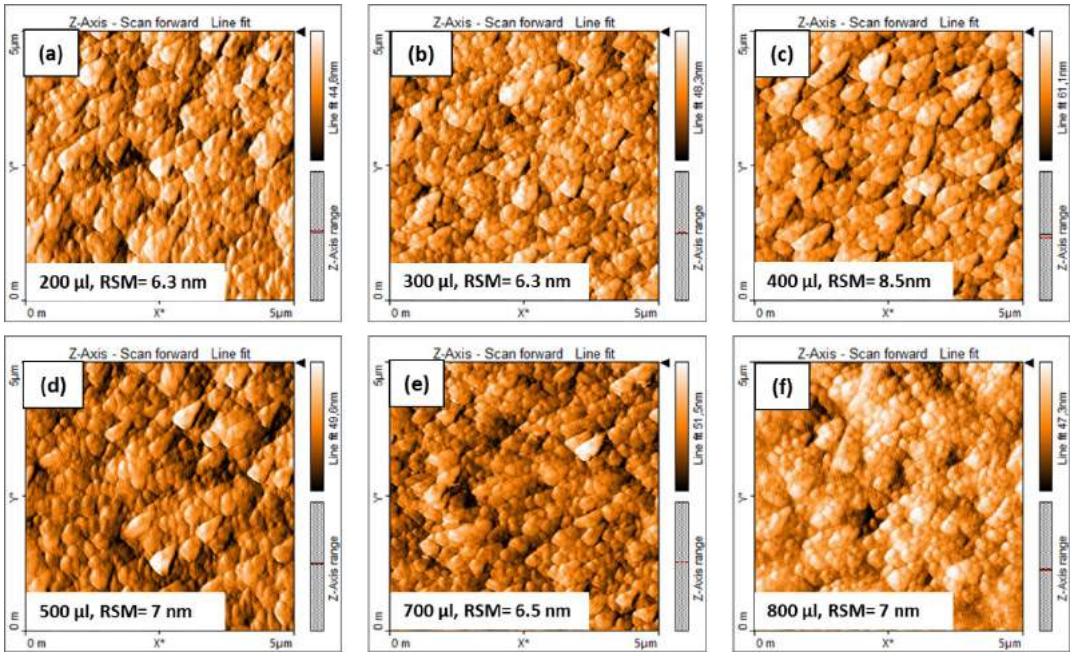

Figure 3.6 AFM images of perovskite films washed with CB with different volumes, (a)-(f) 200µl-800µl, respectively.

From Figure 3.6, it can be observed that the CB volume used for washing does not show a considerable influence on grain size and roughness of films. The grain size is in the range of 140 nm, and the average roughness is about 6.5 nm independently of the used volume. Interestingly, the similar study conducted by Xiao et al., [91] showed oppositive results; they that the anti-solvent volume considerably changed perovskite grain size, crystallization kinetics and coverage of the film. For example, the grain size change from <100 to ~300 nm when 100 or 300 µl of antisolvent was used. However, the volume of precursor solution in the mentioned study is not reported. In our case, with the volume of precursor solution deposited on the substrate, 100 µl of CB is enough to achieve the supersaturation process.

The morphological results are consistent with the XRD and absorption studies. All these studies point out that the right time for dispense CB for washing is at 5 s to produce

perovskite film with the optimal morphology, higher crystalline, and the highest absorbance compared to the pristine film and samples washed at different times. Besides, it should be highlighted that the results are highly reproducible when chlorobenzene is dispensed at 5 s. At least 5 samples were prepared and characterized for each batch, obtaining the same results each time.

3.1.1.4 Photovoltaic device

To evaluate the effect of CB-washed perovskite film features on photovoltaic performance, solar cell devices with the architecture glass/ITO/PEDOT:PSS/$MAPbI_3$/ $PC_{71}BM$/FM were prepared. The $MAPbI_3$ perovskite films with the best crystalline, absorption, and morphological characteristics, i.e., those with CB-washing applied after 5 s that the centrifugation process began, were used as active layer. Besides, films without CB washing were also used as the active layer in HPSCs and were used as a reference. Figure 3.7 illustrated the current density-voltage (J-V) curves for the best photovoltaic devices. The devices based on pristine perovskite film showed a V_{oc} = 0.73 V and J_{sc} = 7.88 mA/cm^2. From these values the FF and PCE were calculated, 0.44 and 2.52 % respectively. While the perovskite solar cell fabricated with the CB-washing film exhibits a slight enhance in the V_{oc} = 0.82 V and increment in the J_{sc} = 10.45 mA/cm^2 compare to pristine device. Therefore, a significant improved in the FF (0.68) and PCE (5.83%) also were achieved.

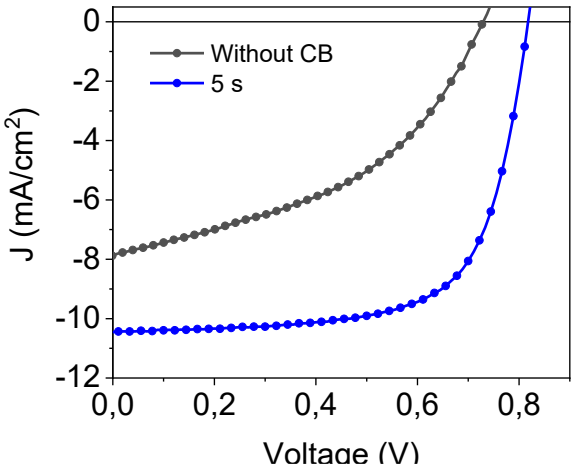

Figure 3.7 J-V curves of perovskite solar cells, based $MAPbI_3$ perovskite films prepared by one-step method with and without CB washing.

The improvement in device performance whose active layer was CB-washed ascribed to a better morphology, i.e., compact and defined grains and lower roughness, which could lead to a better transport of charge carriers towards the respective electrodes and mainly avoiding recombination. Also, the higher crystallinity improves the charge carrier mobility. On the other hand, the poor performance of the pristine device was due to defects in the morphology of the active layer, the presence of an undefined grain structure, and high roughness; it has been reported these features cause charge carrier's recombination at grain boundaries and at the interfaces between devices layers reducing the electrical parameters. [93] In addition, perovskite films washed with CB at other times were also used as active layer in HPSCs, the performance of those devices was similar to the obtained for devices based on pristine film, i.e., efficiencies about 2%.

Table 3.2 shows the photovoltaic parameters of the best cells and, in parenthesis, the average of 10 fabricated devices. As shown in the table, the devices with CB-washing have higher reproducibility; the standard deviation is low; for example, for the PCE, it

was ±0.20%. The opposite case occurs with the pristine devices where the standard deviation for PCE was ±0.58%, indicating low reproducibility related to the irregular areas observed in the morphological study.

Table 3.2. Parameters from the best perovskite solar cells, based on perovskite films treated without and CB washing 5 s

Sample	Voc [V]	Jsc[mA/cm^2]	FF	PCE [%]
Pristine	0.73 (0.74±0,09)	7.88 (4.81±2.24)	0.44 (0.54±0.99)	2.52 (1.77±0.58)
CB-washing 5 s	0.82 (0.81±0.01)	10.45 (11.01±0.77)	0.68 (0.63±0.06)	5.83 (5.59±0.20)

As can be seen, CB washing at 5 s has a positive effect on $MAPbI_3$ film features deposited by the one-step method but also has a significant impact on device performance.

3.1.2 Annealing temperature on perovskite films deposited by the one-step method in a glove box

The annealing temperature is a critical parameter for transforming the precursors into the film of the perovskite; the temperature and time for annealing also influence the features of the films. It has been reported that the minimum temperature to facilitate the formation of $MAPbI_3$ perovskite material in films deposited by the one-step method should be higher than 60 ºC. [74] At lower temperatures, the conversion to perovskite cannot be

completed, while for high temperatures (<120 ºC), the film can be damaged due to the organic compound of perovskite. [44], [74] Nevertheless, the most common temperature reported to obtain the $MAPbI_3$ material is 100 ºC during a time about 10 min when using a solution of Pbl_2 and MAI in a 1:1 molar ratio. [26], [96] While for solutions based on $PbCl_2$ and MAI in a 1:3 molar ratio, temperatures between 90-100 ºC for 1-3 h to complete the total conversion are required. [69-70]

For our analysis on the effect of temperature for the fabrication process, a commercial ink based on a 1:3 molar ratio of $PbCl_2$:MAI diluted DMF (ink-2) was used for the deposition of $MAPb(I_{3-X}Cl_X)$ perovskite film by the one-step method. Different temperatures were considered and its effect on the crystallinity, absorption, and morphology of perovskite films was studied. The deposition of perovskite precursor solution was performed as specified in section 2.2.1. Films were also washed with chlorobenzene, and according to those results in section 3.1.1, the time for dispensing the anti-solvent was 5 s after spin process began. After the spin process, the samples were annealed at 80, 100, and 120 ºC for 60 min in a glove box. Besides, some films were annealed over 120 ºC, and the initial dark brown color of the films changed to yellowish, indicating a decomposition of the perovskite. The formation of PbI_2 caused a change on the color, which originated from the decomposition of $MAPbI_3$ and from the exchange of chloride by iodide in the $PbCl_2$ precursor. [74], [96] The quality of these films was poor, and they were discarded in this study but still considered in our study.

3.1.2.1 Crystallinity

The XRD patterns of the three perovskite films annealed at 80 ºC, 100 ºC, and 120 ºC are shown in Figure 3.8. Interestingly the XRD patterns correspond to $MAPbI_3$ perovskite tetragonal phase (*P4mm* space group) and all patterns showed predominant crystallization along the (010), (020), (021) and (221) planes with peaks at 14.2º, 28.6º, 31.7º y 43.3º, 2θ, respectively. Unit cell parameters of perovskite are: $a\,(\text{Å}) = b = 6.3120$, $c\,(\text{Å}) = 6.3160$, α=γ=β= 90º. The JCPDS card Nº96-433-5635 was obtained from the *X'per* software database and used for calculations.[89]

Although the precursor solution was based on PbCl the expected perovskite material would be $MAPb(I_{3-X}Cl_X)$, nevertheless, according to XRD analysis, the obtained material mainly was $MAPbI_3$. Overall, when chloride is within the perovskite crystal structure the peak at 14.2º (2θ) moves to higher values.[97], [98] It has been reported that the higher MAI concentration favors chloride substitution by iodide in the PbCl leading to obtain mainly $MAPbI_3$ instead $MAPb(I_{3-X}Cl_X)$. [99]

The XRD patterns showed that the peak intensities assigned to (010), (020), and (021) planes slightly increased their intensity for those samples annealed at 80 ºC; this in comparison to the signals for samples annealed at 100 ºC and 120 ºC. The higher intensity could indicate the formation of more perovskite material. From XRD patterns the grain size was estimated; the average values were 56, 55, and 48 nm for samples annealed at 80, 100, and 120 ºC, respectively. Such values are similar, but no remarkable effect can be observed.

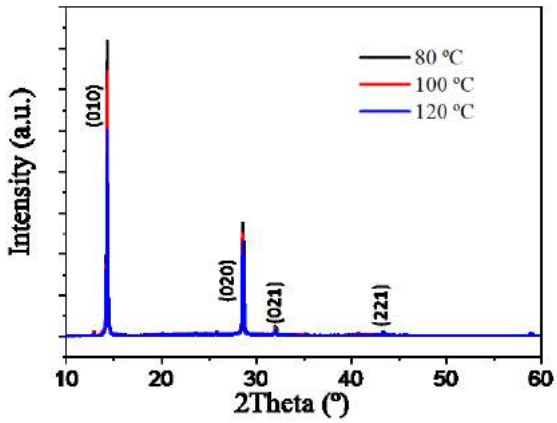

Figure 3.8 XRD of perovskite films annealed at different temperatures at 80 ºC, 100 ºC and 120 ºC.

3.1.2.2 Absorption

Figure 3.9 (a) shows absorption spectra of perovskite films annealed at different temperatures. The absorption spectra cover a wide range from 450 to 800 nm. The edge of absorption is at about 790 nm, which correspond to a bandgap energy of 1.59 eV according to Tauc´s Plot (Figure 3.9 b). The sample annealed at 80 ºC has a slightly higher absorption intensity than the samples annealed at 100 ºC and 120, especially at the edge of absorption. Some reports pointed that this change in absorption intensity is related to an improvement in film crystallinity since the grain size is increased leading to a more efficient absorption within the active layer. [74] Thus, the sample treated at 80 ºC could have larger crystal size than the other two samples, which agrees with the XRD pattern.

Interestingly, the edge of absorption corresponds exactly with that of $MAPbI_3$, Figure 3.3. As mentioned above, the expected perovskite material was $MAPb(I_{3-X}Cl_X)$, however, for this material the edge of absorption and the XRD analysis indicates that the perovskite material is mainly $MAPbI_3$.

(a) (b)

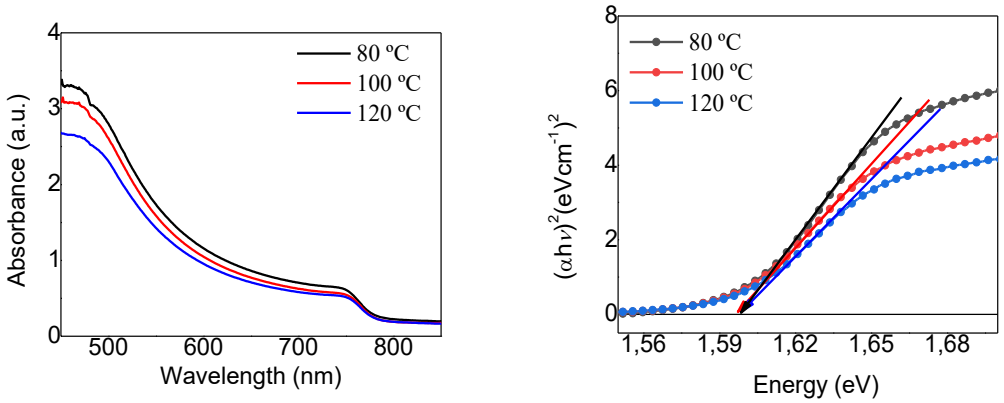

Figure 3.9 (a) UV-Vis absorption and (b) Tauc´s plot for perovskite annealed at different temperatures at 80 ºC, 100 ºC and 120 ºC.

3.1.2.3 Morphology

Figure 3.10 shows AFM images of the morphology for perovskite films annealed at different temperatures, in 5 µm x 5 µm scale. These micrographs show that both distribution and sizes for perovskite grains change as a function of temperature. Figure 3.10 (a) corresponds to the film annealed at 80 ºC; it presents a morphology with compact grains and homogeneous distribution. The grains are well defined with regular shape and an average size of about 400 nm. Also, the film exhibits an average roughness of 34 nm; this value is generally reported for $MAPbI_3$ films fabricated by the one-step method.[94]

When the annealing temperature was 100 ºC, a morphology with large aggregates of perovskite grains with an undefined distribution was observed (Figure 3.10 (b)). Also, pinholes of hundreds of nanometers appear within the film. The average roughness increases from 34 to 39 nm compared against the sample annealed at 80 ºC. Figure 3.10 (c) shows the morphology for the film treated at 120 ºC; similarly, to that annealed at 100 ºC, agglomerates of perovskite grains and pinholes were observed within the film.

However, the size of agglomerates and pinholes increased considerably; both are in the range of micrometers tens. The average roughness in the film was about 37 nm. The changes in the morphology caused by the annealing temperature indicate that, although anti-solvent induces supersaturation and fast nucleation, a rearrangement of perovskite material can be done into the film even after solvent evaporation. [83] It is evident that at lower temperatures, a more controlled crystallization process can be achieved allowing the formation of films with larger grain size and homogeneous distribution, as was the case of films treated at 80 ºC. The thickness of all perovskite films is about 450 nm.

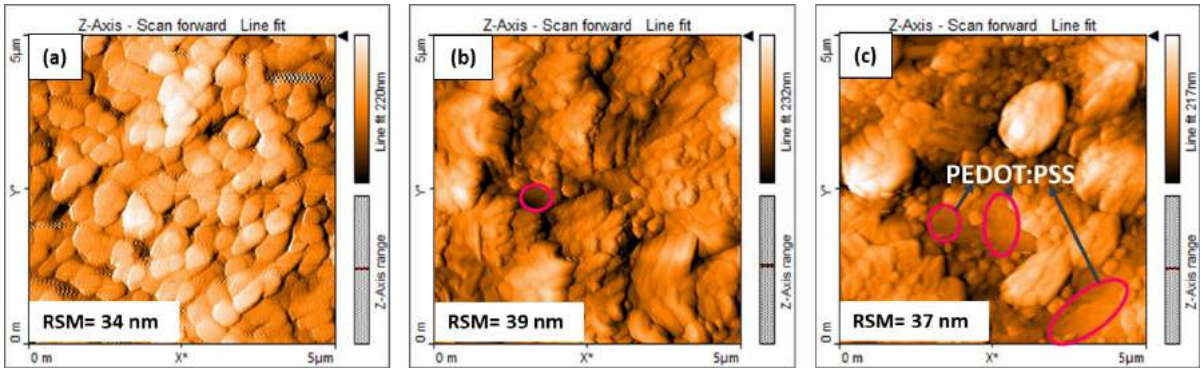

Figure 3.10 AFM of perovskite films annealed at different temperatures at (a) 80 ºC, (b) 100 ºC (c) 120ºC.

Our results agree with some reports where annealing temperature was varied for perovskite transformation. Chavhan et al.[100] investigated the effect of temperature on the morphology of $MAPbI_3$ films, they used 90, 100, 110, and 120 ºC for annealing along 3 h. Although the trend of morphological changes with temperature is alike our results, the reported morphology had discrete islands with several pinholes, i.e., our films present higher homogeneity. Eperon et al. [43] annealed the films at 90, 110, 130, 150, and 170 ºC for 120, 50, 20, 10, and 7.5 min, respectively. In contrast to our results, the authors found that perovskite grain size increased while annealing temperature increased.

However, pinholes size also increased and the morphology changed from continuous layers to islands. This led to a decrease in surface coverage which is unfavorable for photovoltaic devices because it reduces the charge transport and could lead to a short circuit in the device.

3.1.2.4 Photovoltaic device

Perovskite films annealed at 80, 100 and 120 ºC, were used as the active layer in HPSC with architecture glass/ITO/PEDOT:PSS/Perovskite/$PC_{71}BM$/FM. As expected, devices with the film annealed at 80 ºC showed the best J-V curve, as shown in Figure 3.11 (a). The efficiency for such devices was 10.5%, while for films annealed at 100 and 120 ºC was 5.1 and 4.5%, respectively. All PV parameters are given in Table 3.3; the numbers in parentheses are the average device performances determined from 10 fabricated solar cells.

(a) (b)

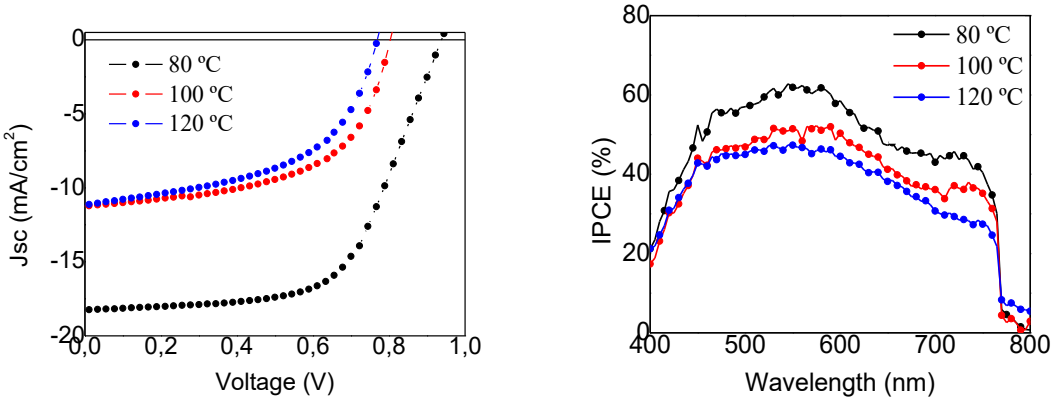

Figure 3.11 (a) J-V curves and (b) IPCE of perovskite solar cells, based on perovskite films treated at different temperatures.

The incident photon-to-current efficiency (IPCE) was also measured for each set of devices, and representative curves are shown in Figure 3.11 (b). The curves for devices based on perovskite films treated at different temperatures can be clearly discriminated; a higher photo-response is observed for devices treated at 80 ºC. For this device an increment in the V_{oc} but mainly for J_{sc} shows higher IPCE and can be ascribed by a better crystalline quality observed from the XRD analysis, as well as the formation of a smooth and compact film without pinholes. For devices treated at 100 and 120 ºC, the reduction in J_{sc} was responsible for the lower efficiency. From Table 3.3 devices with a more homogeneous active layer, i.e., cells with the perovskite film treated at 80 ºC, are highly reproducible. When the temperature increases and the quality of the active layer declines, the reproducibility also decreases; the standard deviations of the PCEs of the 100 and 120 ºC devices are higher than those of the 80 ºC devices.

Table 3.3 PV Parameters from the best perovskite solar cells, based on perovskite films treated at different temperatures.

Sample	**Voc [V]**	**Jsc[mA/cm^2]**	**FF**	**PCE [%]**
80 ºC	0.93	18.26	0.62	10.5
	(0.92±0.01)	(18.33±0.41)	(0.61±0.01)	(10.23±0.21)
100 ºC	0.80	11.23	0.57	5.1
	(0.80±0.01)	(11.29±0.70)	(0.54±0.02)	(4.85±0.36)
120 ºC	0.77	11.16	0.53	4.5
	(0.71±0.11)	(10.69±0.60)	(0.49±0.05)	(3.73±0.63)

3.2 Results for two-step method

As mentioned above, $MAPbI_3$ perovskite films were also prepared by a two-step method; the close-space sublimation and spin-coating methods were used. Analysis of the crystalline, morphological, and optical properties for films prepared by these two methods were conducted and compared with films prepared by the one-step method.

3.2.1 $MAPbI_3$ perovskite films prepared by the close-space sublimation method.

Close-space sublimation is an alternative to prepare perovskite films with presumably better homogeneity and reproducibility.[98] The deposition of perovskite films with this technique was performed as described in section 2.2.2; a precursor solution of MAI and PbI_2 have been used to deposition for the respective films on separate substrates by spin-coating technique. Then for the reaction between the PbI_2 and MAI, films were placed against each other 1 mm apart and located in a vacuum oven under the pressure of -0.8 bar at 130 ºC. MAI sublimates on the PbI_2 film to get $MAPbI_3$ perovskite films. The conditions used for the sublimation process were fixed according to lab conditions and material features; a pressure of -0.8 bar is a typical vacuum level achieved with a mechanical pump (10^{-2} – 10^{-3} torr), while 130 ºC is a temperature necessary for slow MAI sublimation at this pressure.

However, according to some studies the temperature of the PbI_2 solution for the spin-coating process has great influences on PbI_2 film morphology.[98], [101] Therefore, it was studied the effect of the preheating of PbI_2-DMF solutions on morphology and quality

of the PbI_2 films and its final effect on $MAPbI_3$ perovskite films features. Six temperatures between room temperature (RT) and 120 ºC, with intervals of 20 ºC, were used for the preheating of the substrates and PbI_2-DMF solution before the spin coating process. Temperature over 120 ºC was also used but it was discarded from this study due to features of such films were similar than those for samples deposited at 120 ºC.

Photographs of PbI_2 and $MAPbI_3$ films are shown Figure 3.12; notice that the temperature of solution affected the homogeneity of PbI_2 films (top photographs in Figure 3.12). This effect could be due to fast crystallization owing to the induced gradient temperatures by the spin process. When $MAPbI_3$ films were transformed from PbI_2 deposited at RT, 40 ºC and 120 ºC produced opaque and not homogeneous films with irregular areas and white spots. While $MAPbI_3$ transformed from PbI_2 films deposited at 60, 80, and 100 ºC show bright and more homogeneous surfaces, especially the film where PbI_2 was deposited at 100 ºC, which also has a darker brown color.

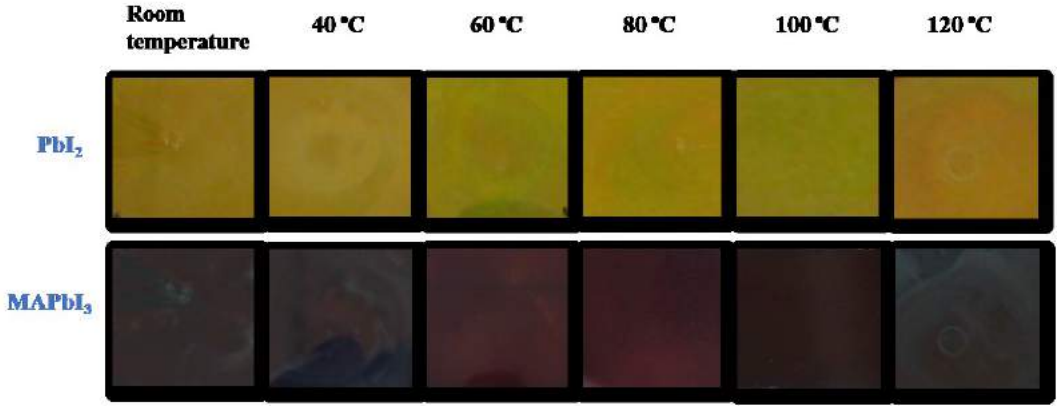

Figure 3.12 PbI_2 films deposited by heating both substrate and solution at different temperature (from room temperature to 120 ºC), as well as the corresponding perovskite films obtained after sublimation of MAI onto PbI_2.

3.2.1.1 Crystallinity

Figure 3.13 shows the XRD patterns for PbI_2 films deposited at different temperatures and $MAPbI_3$ films prepared by close-space sublimation method. Figure 3.13 (a) shows the diffractograms of the PbI_2 films; it can be seen predominant diffraction peaks at 2θ = 12.7º, 25.8º, 39º, and 52.7º that were assigned to 001, 101, 110, and 004 planes. A diffraction peak also appears at 11.7º (red asterisk), which corresponds to the formation of PbI_2•DMF adducts (coordination complexes).[102], [103] The adducts form larger lattice spacing in the structure due to the incorporation of methylammonium cations or DMF molecules between the inorganic sheets; [85] in our films, they would be DMF molecules. Coordination complexes dictate the process of transformation of PbI_2 into perovskite and influence film quality and morphology. Previously Wakamiya et al. observed that the liberation of the coordinated DMF (with Pb) started around 70 ºC and was completed at 112.6 ºC when the samples changed from pale to intense yellow. [84] These results are consistent with those reported here; our films also changed from pale to intense yellow with increasing temperature (top photographs in Figure 3.12).

The XRD patterns of $MAPbI_3$ perovskite are shown in Figure 3.13 (b). The XRD patterns correspond to tetragonal phase (*I4/mcm* space group) $MAPbI_3$ perovskite and can be observed diffraction from planes (110), (112), (121), (022), (220), (222), (132), (040), (330), and (044); assigned from peaks at 2θ = 14.2º, 19.9º, 23.5º 24.7º, 28.6º, 31.7º, 35.1º, 40.8º, 43.3º, and 50.5º, respectively. The peaks for perovskite film transformed from PbI_2 deposited at 100 ºC are more intense than those of the other samples, which could indicate higher crystallinity. Unit cell parameters of perovskite are: $a\,(\text{Å}) = b = 8.8395$,

$c\,(\text{Å}) = 12.4265$, α=γ=β= 90º. The JCPDS card Nº 4124388 were used for the calculation. The card was obtained from *crystallography open database* open-access.[89]

(a) (b)

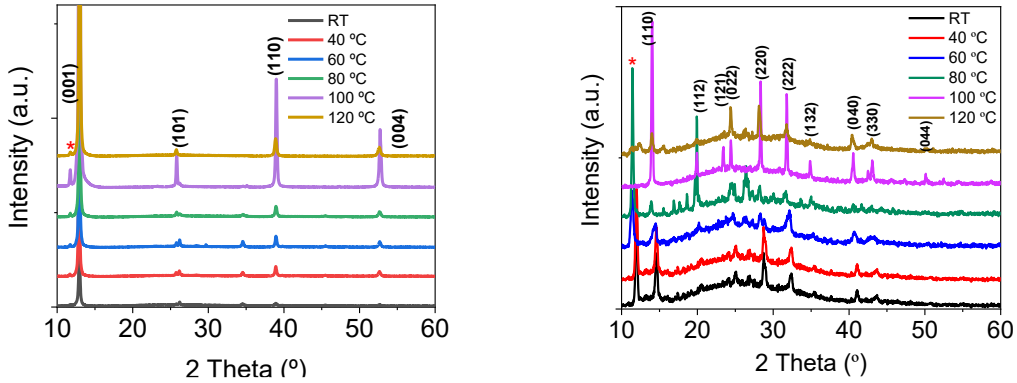

Figure 3.13 XRD patterns for (a) PbI_2 films deposited from solutions heated at several temperature, from room temperature (RT) to 120 ºC, and (b) transformed into $MAPbI_3$ by close-space sublimation.

When PbI_2-DMF solution was deposited at temperatures below 80 ºC, the peak at 11.7º (red asterisk) was observed. This peak indicates that some adducts remain in the perovskite lattice after the sublimation of MAI. While the perovskite films reached from PbI_2 film deposited at 100 ºC and 120 ºC do not show this peak, indicating the total transformation of PbI_2 into $MAPbI_3$ perovskite, that is, the substitution of the adduct by MAI along the sublimation process.

3.2.1.2 Absorption

The absorption spectra of the $MAPbI_3$ films are shown in Figure 3.14 (a), the edges of absorption are at about 790 nm, which correspond to the bandgap energy of 1.59 eV

according to Tauc´s Plot (Figure 3.14 (b)). The absorption curves cover a wide range of wavelengths from the visible to the near infrared. The intensity of absorption spectra increases with increasing the temperature for deposition of PbI_2 films; a higher absorption can be related to a better transformation of PbI_2 into $MAPbI_3$. The absorption results agree with the different appearances for perovskite films presented in Figure 3.12 and the intensity of peaks in diffractograms from XRD analysis, as well as the absence of peak assigned to adduct in perovskite films prepared from PbI_2 deposited over 100 ºC.

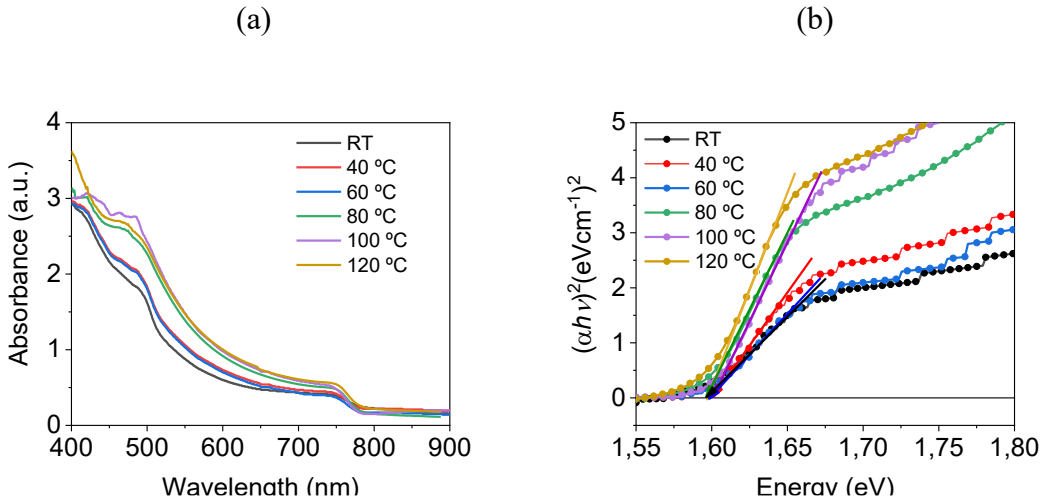

Figure 3.14 (a) UV-Vis absorption and (b) Tauc´s plot for $MAPbI_3$ films transformed by close-space sublimation method.

3.2.1.3 Morphology

The morphology and quality of the PbI_2 and $MAPbI_3$ films were studied by SEM and AFM (see Figure 3.15). Both features showed the strong influence of the temperature used for the deposition of PbI_2 films. The main influence was on the size and distribution of grains in the final $MAPbI_3$ films. For all the cases, the perovskite films show a granular morphology; however, for RT, 20 ºC and 60 ºC, both PbI_2 and perovskite films showed

several pinholes and varied grain size domain. For 80 ºC, the pinholes were reduced in both films, and at 100 ºC, the PbI_2 and perovskite films exhibit the best homogeneity and biggest-compact grains. While at 120 ºC, the films have a non-well-defined morphology (see Figure 3.15 (f)).

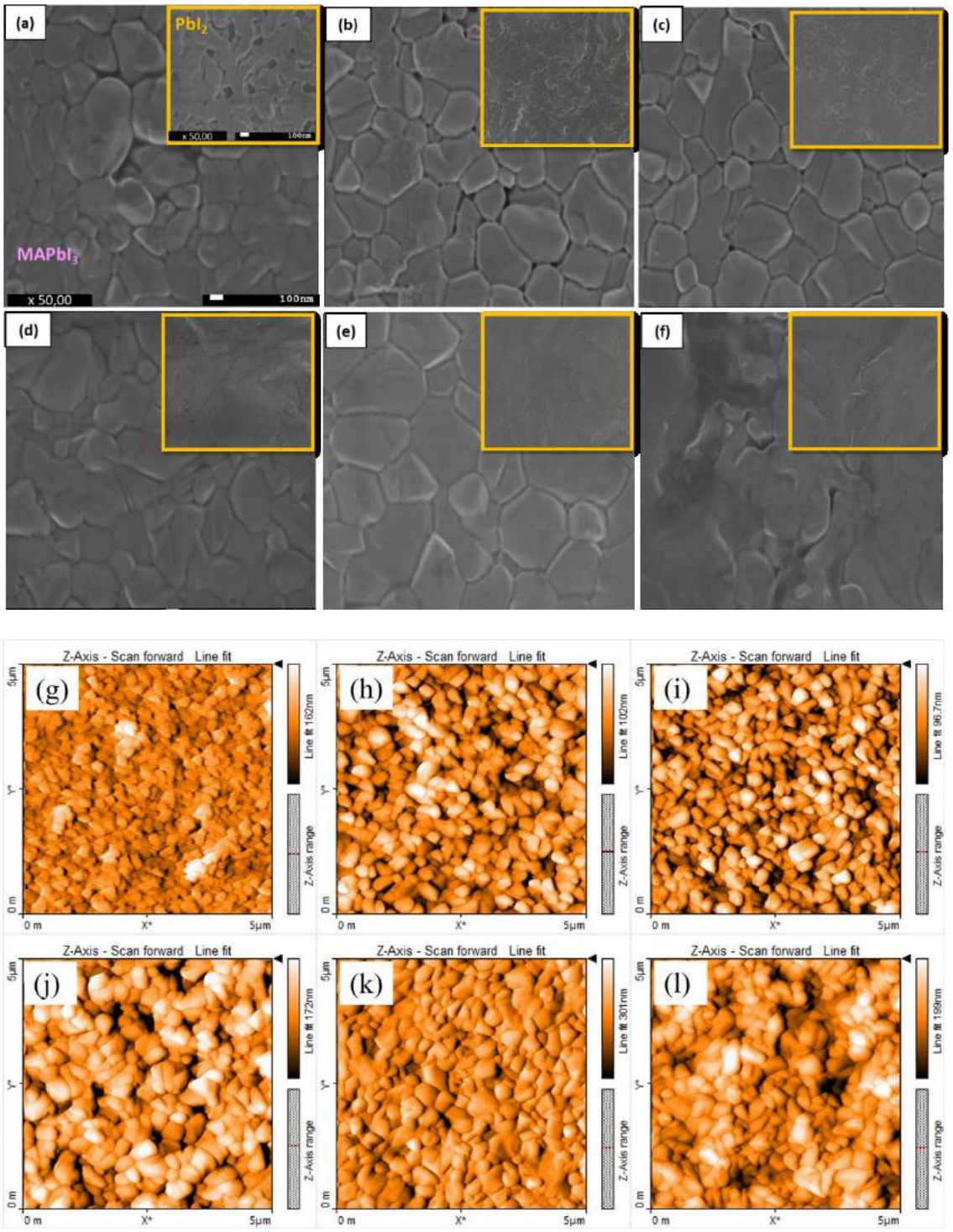

Figure 3.15 Representative SEM and AFM images for perovskite films achieved by sublimation of MAI onto PbI_2 films. The PbI_2 (yellow square in SEM images) was deposited by spin-coating from solutions at (a), (g) room temperature, (b), (h) 40 ºC, (c), (i) 60 ºC, (d), (j) 80 ºC, (e), (k) 100 ºC and (f), (l) 120 ºC.

The morphological change of the PbI_2 films could be related to the formation PbI_2•DMF adducts, which causes variation in the growth and arrangement of the PbI_2 crystals and, in turn, is consistent with the appearance of the films (change of color films, see Figure 3.12). The average roughness and thicknesses of the PbI_2 and $MAPbI_3$ films were measured by AFM, the values are reported in Table 3.4. The average roughness values for PbI_2 films are similar between 10 and 16 nm when temperatures between RT and 100 °C were used for deposition. While for $MAPbI_3$ films, the average roughness was between 11 and 25 nm. When 120 ºC was used for PbI_2 deposition, an increment in average roughness was observed, 25 and 36 nm, to PbI_2 and $MAPbI_3$ films, respectively. These average roughness values are in the range of some recently reported works. [104-105]

On the other hand, the measured thicknesses of the PbI_2 films are in the range of 180 to 210 nm being the lowest value for the sample deposited at room temperature and the highest value for the sample at 120 ºC; these results clearly showed the effect of the temperature used for PbI_2 deposition. With the transformation from the inorganic films into perovskite films, thickness increases ~200 nm in all cases, being between 378 and 419 nm. The variation of thicknesses of PbI_2 films is related to the crystallization process induced by the fast quenching (from the initial temperature to RT) due to the spin process. The final thickness for $MAPbI_3$ films is due to the introduction of MAI cation to form perovskite structure. The thickness variations together with transformation grade can explain the slight changes in the intensity of the UV-Vis absorption spectra of the perovskite films shown in Figure 3.14 (a).

Table 3.4 The average roughness and thicknesses of PbI_2 and $MAPbI_3$ films from PbI_2-DMF solutions heated to temperatures from room temperature (RT) to 120 ºC.

Measure	Film	RT	40 ºC	60 ºC	80 ºC	100 ºC	120 ºC
Roughness (nm)	PbI_2	10	16	12	14	12	25
	$MAPbI_3$	11	25	18	19	17	36
Thickness (nm)	PbI_2	180	193	198	204	208	210
	$MAPbI_3$	378	383	402	406	415	419

To improve the quality of $MAPbI_3$ films by the sublimation method was also used DMSO as a co-solvent in the PbI_2 solution (see section Appendix I). Different volume ratios of DMF and DMSO were used in the solutions precursor. The introduction of DMSO showed an effect on the morphology and crystallinity of $MAPbI_3$ films. However, the adjustment of the solvent chemistry does not allow a precise control on the film reproducibility and the performance of the device. Here, with changes in the temperature for the deposition of PbI_2 films, it was avoided the use of an additional solvent; this procedure was highly reproducible and simplified the process.

3.2.1.4 Photovoltaic device

The perovskite films were used as the active layer in solar cell devices with the configuration ITO/PEDOT:PSS/Perovskite/$PC_{71}BM$/FM architecture. According to the morphological and XRD analysis, films where PbI_2 was deposited at 100 ºC show the better features to be used as the active layer. Therefore, devices were prepared with these films and, as a reference, devices with perovskite films where PbI_2 was deposited at room temperature (RT) were also fabricated. Figure 3.16 shows the J-V plots of the devices,

the average of electrical parameters from a set of 10 devices are summarized in Table 3.5. As expected, the best performance was for the device in which PbI_2 was deposited at 100 ºC. An efficiency of 7.6% was achieved with a V_{oc} of 0.76 V, J_{sc} of 15 mA/cm^2, and FF of 0.67. While for devices where PbI_2 was deposited at RT, the efficiency was 3.91%, mainly due to a lower current density. The improved performance for the former devices is related to a higher J_{sc} and is associated with a better morphology and crystallinity. The higher photocurrent is attributed to the reduction in the loss of photo-generated carriers at the grain boundaries and recombination processes.

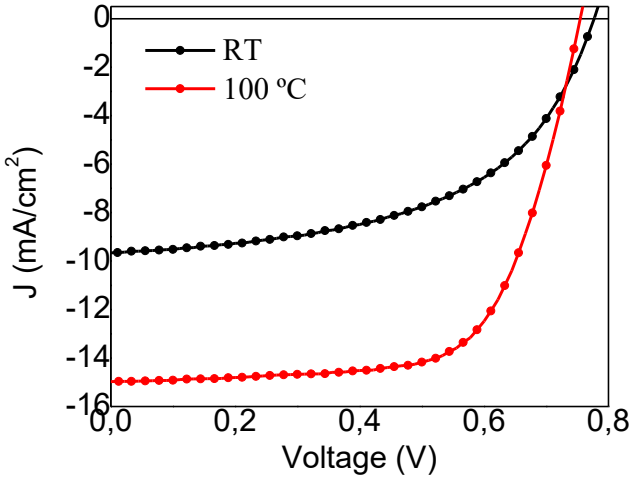

Figure 3.16 J-V plots for the best perovskite photovoltaic devices obtained from PbI_2 films deposited from solutions at room temperature (RT) and 100 ºC.

Table 3.5 PV parameters for perovskite solar cells, where PbI_2 films were deposited at room temperature (RT) and 100 ºC. In parenthesis the average values determined from 10 devices with standard deviations.

Sample	Voc [V]	Jsc[mA/cm^2]	FF	PCE [%]
RT	0.77 (0.74±0,02)	9.65 (7.21±2.20)	0.53 (0.49±0.03)	3.91 (2.99±0.92)
100 ºC	0.76 (0.73±0.03)	15 (12.75±2.07)	0.67 (0.63±0.04)	7.60 (6.59±1,01)

As can be seen, the temperature used for PbI_2 films deposition determine its morphological and structural properties, which in turn, will determine those of $MAPbI_3$ perovskite layer after transformation by the close-space sublimation method. This method allows us to get perovskite films with good homogeneity and reproducibility.

3.2.2 $MAPbI_3$ perovskite films prepared by the spin-coating method with sequential disposition.

The sequential spin-coting process is also a two-step method for perovskite deposition; it is highly used to fabricate $MAPbI_3$ films. The process also involves the deposition of PbI_2 films by spin coating, and then a MAI solution is spin-coated onto PbI_2 film. The reaction of the two precursors (organic/inorganic) into the film leads to the formation of $MAPbI_3$ perovskite material. Several authors have reported that in the sequential spin-coating process, the proportion of MAI and the control of its deposition parameters, for instance, used volume of MAI solution, atmosphere, the rate for dispense solution, etc., determine

the quality of perovskite film. [53] In this work, a less studied parameter, the time that MAI solution remains onto the PbI_2 film after being dispensed and before the centrifugation process began, was analyzed; we named it centrifugation waiting time (CWT). This parameter is important because it could influence the reaction kinetics between PbI_2 to MAI to form $MAPbI_3$. It determines the diffusion of MAI into PbI_2 film and has important effects on the structural, morphological, and optoelectronic properties of the perovskite film. Moreover, this is an important parameter to improve the reproducibility of the films, which has not been reported in the literature.

According to those achieved results in the previous section, the PbI_2 film was deposited from a PbI_2-DMF solution heated (together with the substrate) at 100 ºC for 15 min before deposition (Section 3.2.1). The film was annealed at 140 ºC by 30 min in a vacuum oven a pressure of -0.8 bar; this treatment is essential to remove DMF solvent totally because we observed that traces of this solvent together with ethanol from MAI solution could induce damage in the perovskite films. To form perovskite material, the PbI_2 film was placed on spin-coater and 100 µl of the MAI solution was dispensed onto the film, the solution remains onto film 15, 20, and 25 s before centrifugation started. Finally, thermal annealing was performed to ensure the solvent evaporation and achieve the transformation to $MAPbI_3$. Details of film deposition are reported in the experimental section.

When the MAI solution is dispensed on the PbI_2 film, a change in color from yellow to light brown was observed. The brown color comes stronger after thermal annealing, changing from light to dark brown. Figure 3.17 (a) shows these changes before and after the annealing. The film color also changes depending on the CWT, which indicates the

conversion percentage resulting from different diffusion of the MAI within PbI_2 films, as indicated in the scheme of Figure 3.17 (b). CWT lowers than 10 s were also used; however, the samples were not homogeneous; they showed areas with yellow and brown spots because of incomplete conversion. The lack of homogeneity caused them to be discarded from this study.

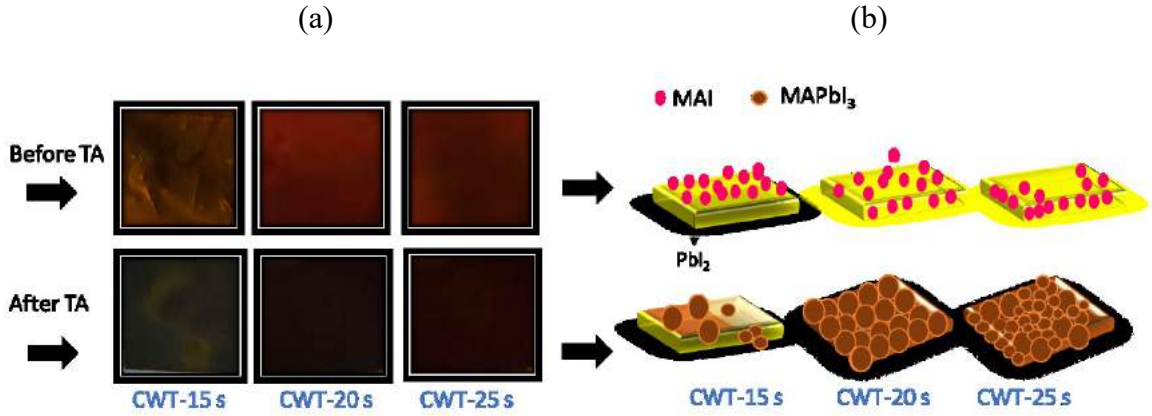

Figure 3.17 Perovskite films prepared by the two-step method sequential deposition with different CWT. (a) Photographs and (b) schematics of the processes of before and after of annealing.

3.2.2.1 Crystallinity

Inhomogeneous diffusion of MAI into PbI_2 films can generate different percentages of transformation affecting the crystallization of $MAPbI_3$ films. Figure 3.18 shows the XRD patterns of perovskite films for the different CWT and annealing time between 15 and 120 minutes. In Figures 3.18 (a), the XRD pattern for the sample with CWT of 15 s shows peaks from PbI_2 at $2\theta = 12.7^o$, 39^o, and 52.7^o that correspond to planes (001), (110) and (004), respectively. Although after annealing, the diffractograms show a peak at 14.2^o, which corresponds to $MAPbI_3$, the peaks from PbI_2 predominates independently of the annealing time; times up to 120 minutes were tried. The presence of PbI_2 indicates an

incomplete transformation into $MAPbI_3$ owing to the short CWT; the PbI_2 in perovskite film acts as a recombination agent to the detriment of photovoltaic performance. [93], [106]

(a) (b)

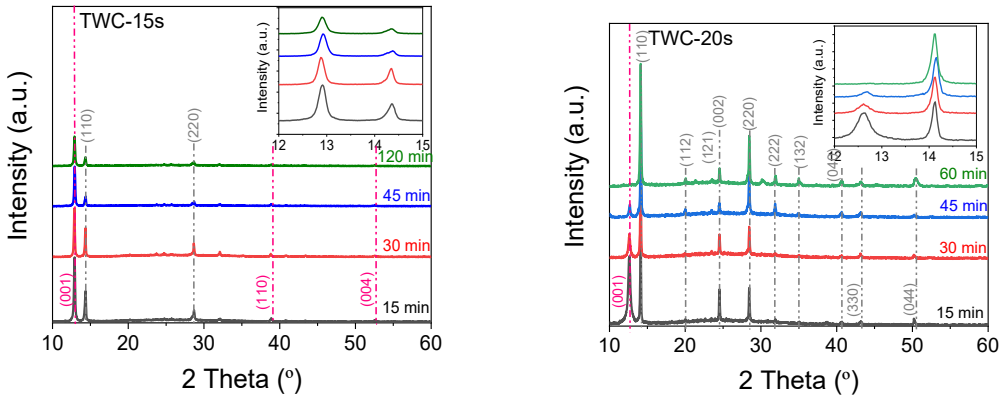

(c)

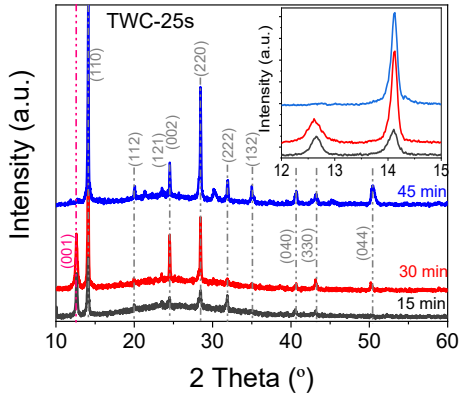

Figure 3.18 The XRD pattern of perovskite films with different CWT, (a) 15 s, (b) 20 s and (c) 25 s. Pink and black dotted lines correspond to the peaks of PbI_2 and $MAPbI_3$, respectively.

In Figures 3.18 (b) and (c), the XRD patterns for films with CWT of 20 s and 25 s are shown. The diffractograms show the presence of peaks assigned to PbI_2 when a short annealing time was used; however, complete conversion into perovskite was obtained in 60 and 45 min, for CWT of 20 s and 25 s, respectively. With both times, enough MAI diffusion was achieved, and under the annealing, the perovskite formation was possible. The diffractograms indicate the formation of the tetragonal phase (*I4/mcm* space group) for $MAPbI_3$ perovskite with peaks at 2θ=14.2º, 19.9º, 23.5º 24.7º, 28.6º, 31.7º, 35.1º, 40.8º, 43.3º, and 50.5º. The peaks were assigned to planes (110), (112), (121), (022), (220), (222), (132), (040), (330), and (044), respectively. Unit cell parameters of perovskite are: $a\,(\text{Å}) = b = 8.8395$, $c\,(\text{Å}) = 12.4265$, α=γ=β= 90º. The JCPDS card Nº 4124388 were used for the calculation. [89]

3.2.2.2 Absorption

Figure 3.19 shows the UV-Vis absorption spectra of perovskite films with CWT of 15 s, 20 s, and 25 s; the films were annealed 120 min, 60 min, and 45 min, respectively. For CWT of 20 s and 25 s, the absorption spectrum is quite similar; in both cases, the edge of absorption is over 820 nm, and only for CWT of 20 s a slightly higher absorption was observed. The absorption spectrum for the film with CWT of 15 s is mainly dominated by PbI_2 absorption (it shows an absorption shoulder around 500 nm). The absorption spectra of these perovskite films are consistent with the color observed for each one and XRD studies, which indicate that more PbI_2 is converted to $MAPbI_3$ with a longer CWT. Figure 3.19 (b) shows the Tauc´s plot for perovskite films; the calculated bandgap was of 1.98 eV, 1.49 eV, and 1.52 eV for films with CWT of 15 s, 20 s, and 25 s, respectively.

(a) (b)

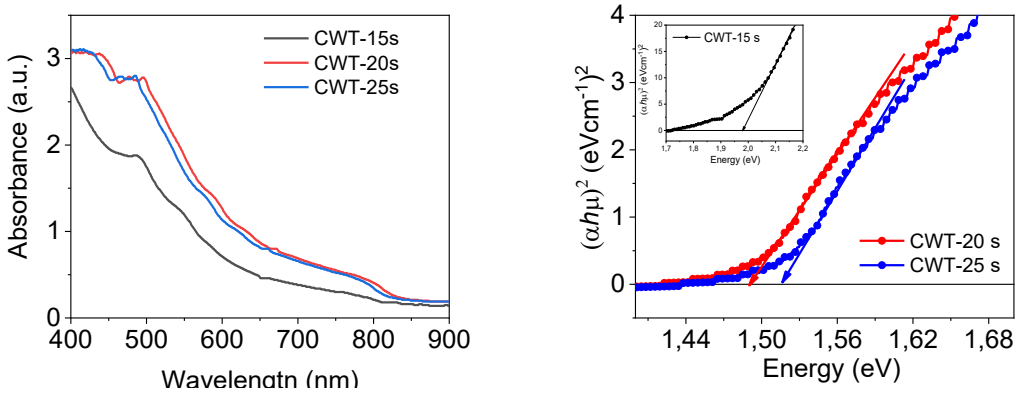

Figure 3.19 (a) UV-Vis absorption and (b) Tauc´s plot for perovskite films with CWT of 15s, 20s and 25s.

3.2.2.3 Morphology

Figure 3.20 (a) shows the AFM images for films with different CWT; in all cases, a granular morphology was observed. However, for CWT of 15 s, the grains are not well defined; they look fused. Figure 3.15 (e) showed the morphology for PbI_2 film is a homogeneous and smooth surface. As can be seen, the transformation of PbI_2 into $MAPbI_3$ leads to a change from a smooth morphology to a grained one. Therefore, the morphology observed for the film with CWT of 15 s indicated an incomplete transformation that agrees with UV-Vis absorption and XRD results. The average roughness for this film was 14 nm. For CWT of 20 s and 25 s, the granular morphology is better defined and the average roughness increases ~24.5 nm, this can be related with a complete transformation into perovskite material. Although the morphology for these films are quite similar, the morphology of the 20 s sample adopts a larger grain size (~ 400 nm) compared to those of 25 s sample (~ 250 nm).

The measured thickness of the films is in the range of 280-300 nm for the three films.

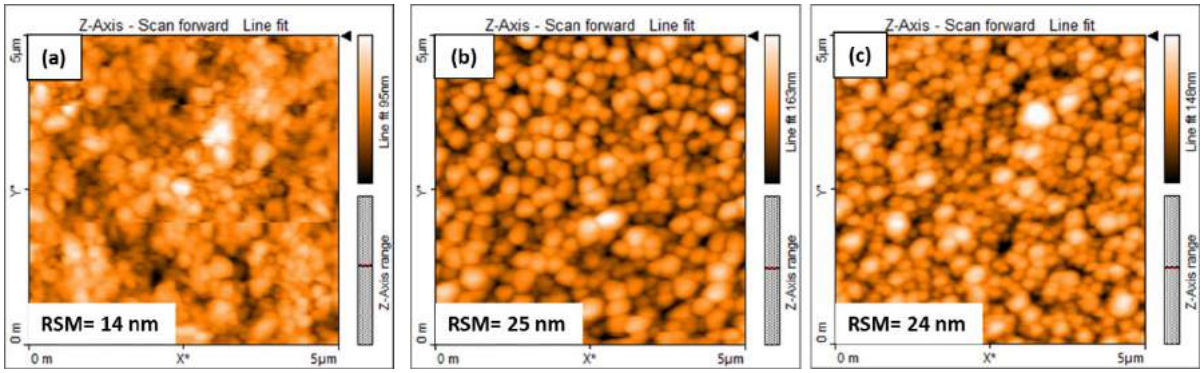

Figure 3.20 AFM images of perovskite films with CWT of (a) 15 s, (b) 20 s and (c) 25 s. RSM in the average roughness.

3.2.3.4 Photovoltaic device

Perovskite solar cells were fabricated using the ITO/PEDOT:PSS/Perovskite/$PC_{71}BM$/FM architecture, and perovskite active layer was a film CWT of 15s, 20s and 25s. Figure 3.21 shows representative J-V curves for such devices, and Table 3.6 lists the average photovoltaic parameters based on a set of ten devices. Devices with CWT of 15 s showed a poor PCE performance of 1.29%; overall, low values were obtained in their photovoltaic parameters. This could be due to the incomplete conversion of PbI_2 into perovskite, evidenced above. For devices with CWT of 20 s and 25 s, the average PCE was 6.37% and 5.23%, respectively. The main difference in the performance of such devices is the J_{sc} value, being 10.66 mA/cm^2 for devices with CWT of 20 s. Owing to the active layer for both devices showed complete conversion and similar absorption, the increment in photocurrent could arise from a well-defined granular morphology with a grain size of ~400 nm, which is larger than shown by the sample with CWT of 25 s. The change in grain size is related to the crystallization

speed of the films, which was controlled with the different waiting times prior to centrifugation after having deposited the MAI. It is well known that grain boundaries act as traps and recombination centers to the detriment of photocurrent.

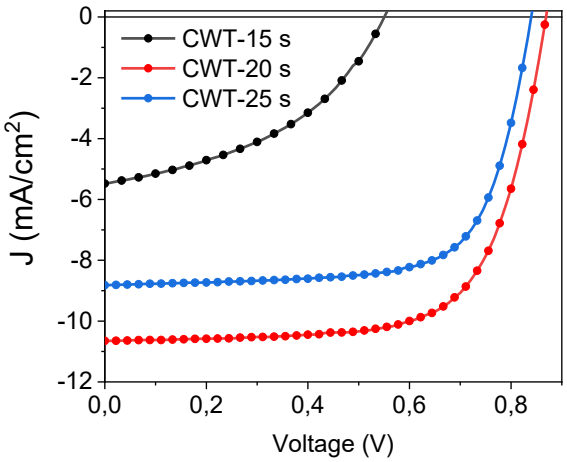

Figure 3.21 Representative J-V curves of perovskite solar cells based on $MAPbI_3$ perovskite films prepared by two-step method with sequential disposition. CWT of 15s, 20 s and 25 s.

Table 3.6 Average parameters for perovskite solar cells, with CWT of 15 s, 20 s and 25s

Sample	**V_{oc} [V]**	**J_{sc}[mA/cm^2]**	**FF**	**PCE [%]**
CWT-15 s	0.54	5.48	0.43	1.29
	(0.50±0.04)	(5.26±0.22)	(0.40±0.03)	(0.90±0.39)
CWT-20 s	0.87	10.66	0.69	6.37
	(0.80±0.06)	(9.31±0.35)	(0.61±0.08)	(5.80±0.57)
CWT-25 s	0.83	8.82	0.71	5.23
	(0.75±0.08)	(8.3±0.52)	(0.65±0.06)	(4.61±0.62)

3.3 Study of the $PC_{71}BM$/CE interface of perovskite cells with FM and Ca-Ag as counter electrode.

It has been widely reported that defects or imperfections at grain boundaries of the perovskite layer or at the interface with charge transport layers deeply influence device performance. [93], [107-108] Enhanced physical processes of transport and extraction of charge carriers from the active layer to the electrodes must be carried out in a well-constructed layered structure avoiding bulk and interface defects. [109] Such defects in films and interfaces would cause charge trapping or recombination as well as inefficient charge collection, which significantly would diminish the photovoltaic parameters. [107] However, we found that the defects at the electron transport layer and counter-electrode interface, ETL-CE interface, with an alternative CE are not explicitly determining the charge collection, suggesting that electrons can move along perovskite layer until reaching a zone with homogeneous contact between ETL-CE.

In this work inverted-planar structure perovskite solar cells with glass/ITO/PEDOT:PSS/$MAPbI_3$/$PC_{71}BM$/CE architecture was fabricated and the ETL-CE interface, and its influence on device performance was analyzed by means of SEM, IPCE and laser beam induced current (LBIC). Field's metal (FM) and Ca/Ag were used as alternative CE and reference CE, respectively. The devices were fabricated as indicated in the experimental section. The $MAPbI_3$ film was deposited by one-step method. The morphological and crystalline study of the $MAPbI_3$ film was presented in section 3.1.2.

The study of the interface ETL-CE through SEM was carried out. The Figure 3.22 (a) and Figure 3.22 (b) and (c) show the cross-section images of HPSCs with Ca/Ag and FM as

CE, respectively. These figures show that the Perovskite-$PC_{71}BM$ interface is homogeneous, with continuous physical contact. For cells with Ca/Ag, a continuous contact between the $PC_{71}BM$ layer and the CE is also observed (see Figure 3.22 (a)) while for the case of FM CE large defects at the $PC_{71}BM$-FM interface can be observed; Figure 3.22 (b) and (c) show regions at this interface with homogeneous contact as well as empty zones with poor physical contact (red rectangles and blue ellipses, respectively). The empty spaces can be as large as tens of microns (see Figure 3.22 (c)). This would have an important effect on devices performance because a good physical contact at the ETL-CE interface would increase the efficiency of electron-extraction and the recombination of the charge carriers diminishes, avoiding current leakages. Poor physical contact would force electrons to move through longer distances in the ETL in order to be collected by the CE, which would increase the charge transport resistance.[110] In addition, during the transport process charge carriers can be captured or recombined in the observed empty spaces at this interface. Therefore, areas with good physical contact at the ETL-FM interface would be responsible for good collecting of electrons and would potentially be crucial for good performance of the device.

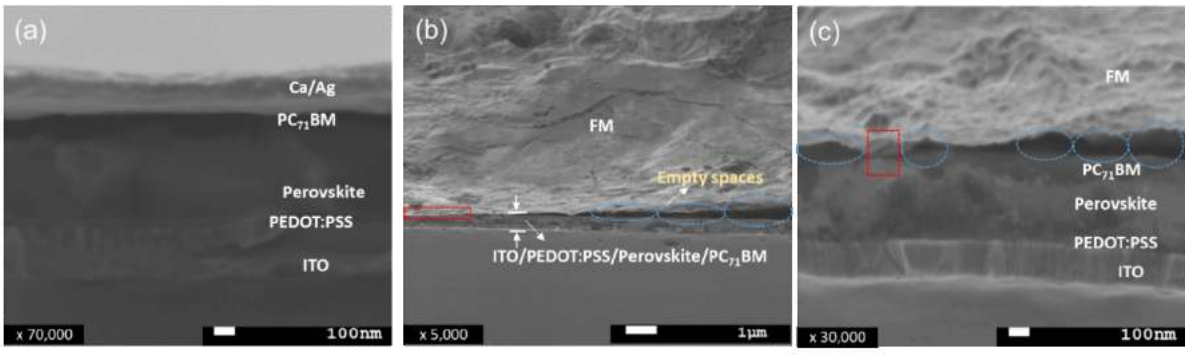

Figure 3.22 SEM images for PSCs cross section with (a) Ca/Ag and (b, c) FM and as CEs.

The J-V plots behavior and PCE of HPSCs with Ca/Ag and FM as CE were evaluated. Representative J-V curves are displayed in Figure 3.23 (a) and Table 3.7 shows the photovoltaic parameters of the best cells and, in parenthesis, the average of ten fabricated devices. The PCE of the devices with alternative CE was close to the value of the evaporated CE, a maximum value of 10.5% for devices with FM and 11.6% with evaporated Ca/Ag was achieved. These PCEs are similar to several previous reports with a similar architecture and evaporated CE.[36-37]

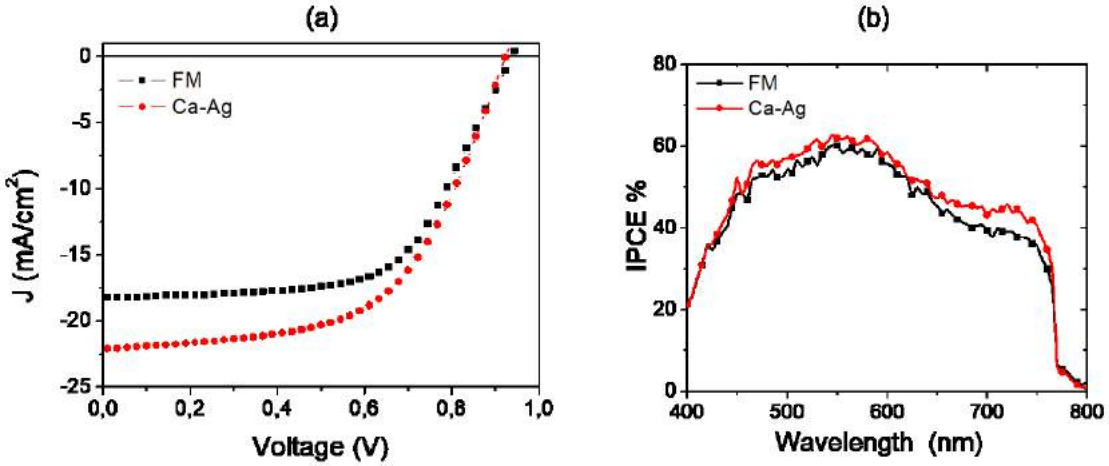

Figure 3.23 (a) J-V curves and (b) IPCE of PSCs, with FM or Ca/Ag as CEs.

Table 3.7 PV parameters for HPSCs with Ca/Ag and FM as counter-electrode.

CE	V_{oc} [V]	J_{sc}[mA/cm^2]	FF	PCE [%]
FM	0.93 (0.92±0.02)	18.26 (18.33±0.40)	0.62 (0.61±0.04)	10.50 (10.20±0.60)
Ca/Ag	0.92 (0.90±0.02)	22.14 (19.84±0.20)	0.57 (0.59±0.01)	11.60 (10.50±0.20)

The slight decrease in the efficiency of the device with FM is due to the reduction in J_{sc}; 22.14 mA/cm^2 with Ca/Ag meanwhile 18.26 mA/cm^2 with FM. The J_{sc} reduction would be ascribed to the inhomogeneous physical contact at $PC_{71}BM$-FM interface as observed in the SEM images. The lack of contact in some regions of such interface leads to a lower electron harvesting and charge loss. The IPCE of devices was also measured and Figure 3.23 (b) shows the corresponding plots. Notice that both curves are quite similar and only a slightly higher IPCE value was recorded for devices with Ca/Ag. Therefore, the slight decay of the spectrum in the cells with FM implies that the charge collection is lower than with the Ca/Ag thereby induced a smaller J_{sc} for cells with FM.

The photocurrent response (at the microscale regime) on the active area of perovskite devices was also analyzed by the laser beam induced current (LBIC) technique. Figure 3.24 shows representative LBIC photocurrent contour maps of the active area for cells (analyzed active areas were designed in a circle shape of 0.07 cm^2). The red zones in the images denote a higher current and the blue ones zero response. As expected, the photoresponse for the device with Ca/Ag is uniform in almost the whole analyzed area (see Figure 3.24 (a)). In contrast, for devices with FM some non-homogeneous regions can be observed (see Figure 3.24 (b)). Variations on photocurrent response depicted by zones with different coloration, yellow, green and blue are shown. Most of the defects revealed by LBIC analysis are in the periphery of active area, this could be related with the deposition technique, it can also be observed at the center of active area defects with no photoresponse are presented (small areas with green or blue color). These defects correspond to poor physical contact at the ETL-FM interface, which are consistent with the non-contact zones observed in the SEM study. However, LBIC images shown that,

even at the center of active area the good photoresponse (yellow and red zones) is large enough leading to currents comparable with the cells that were fabricated with Ca/Ag.

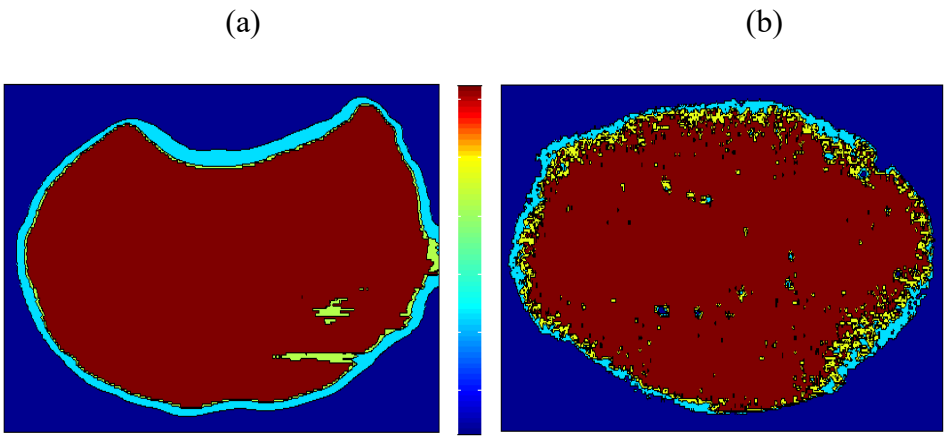

Figure 3.24 LBIC images of photoresponse for PSCs with (a) Ca/Ag and (b) FM as CEs.

For HPSCs not only the interface of the CEs determines the photovoltaic performance, but also the work function of the CEs, the Fermi level of the active layer and the energy levels of the transport layer. [111] Therefore, the good performance of FM as an alternative CE could also be related to its electronic properties such as work function, about 4.2 eV; [11-12] this value is quite similar to that for Ag or Al that are usually used in inverted architecture. Figure 3.25 shows the energy level diagram for HPSCs. Based on previous results, it can be assumed that the FM forms an ohmic contact with the perovskite active layer, in such a way that the equilibrium energy to equalize the Fermi levels occurs predominantly at the contact Perovskite-$PC_{71}BM$.[112]

Owing to the observed differences at the ETL-CE interface for both used electrodes, it is reasonable to suppose that the charge extraction for FM counter electrode should be significantly affected. However, it was found that the photovoltaic parameters for devices with FM are quite like those of the evaporated CE. Therefore, performance of devices

using FM as CE suggests that the observed defects in morphology and contact at the interface $PC_{71}BM$-FM do not play, necessarily, a crucial role in the device performance. Also, that a continuous contact at ETL-CE interface could not be mandatory for acceptable performance of PSCs.

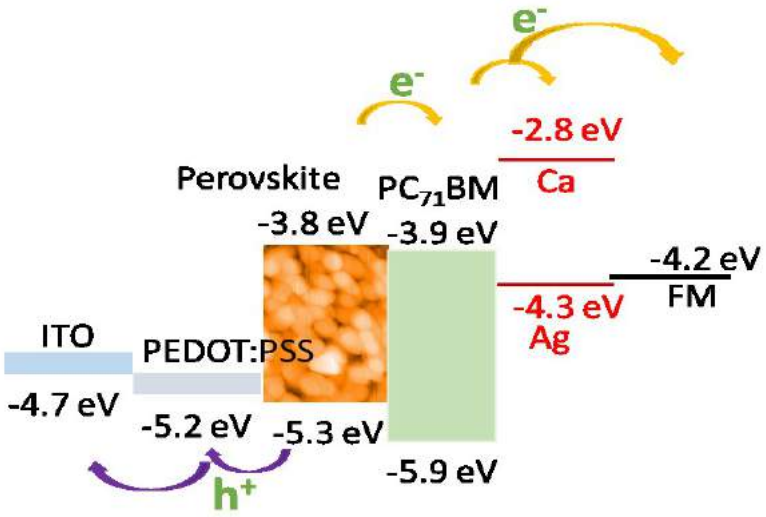

Figure 3.25 Schematic energy level diagram of PSCs

4. Comparative discussion

4.1 Films deposited by one-step and two-step methods

Despite the one-step and two-step methods used for deposition of perovskite films have different variables and deposition conditions, worth looking into the final features of films. Following, we will conduct a comparison of the best films prepared by one-step and two-step methods.

The best perovskite film prepared by the one-step method was obtained when the precursor solution (PbI_2 and MAI with DMF solvent) is deposited by spin-coating technique and washed with chlorobenzene 5 s after the spin process began, and annealing temperature of 80 ºC. The best perovskite film prepared by the two-step method is prepared by the close-space sublimation method from a PbI_2 film deposited at 100 ºC. The overall process for deposition of perovskite film by one-step and two-step methods involves using the preheated solution, a spin coater, and annealing treatment of the deposited film. However, the close-space sublimation method needs a vacuum oven with temperature for the preparation of perovskite film. These conditions make sublimation a more complex method. Therefore, the one-step spin-coating technique is an easier method.

The XRD pattern for the best perovskite films prepared by the one-step and two-step method showed differences. The symmetry of the space group assigned for films prepared by one-step and two-step method was P_4mm and *I4mcm*, respectively. For both space groups, the crystallographic system is tetragonal; however, the difference is the values for

a, b, and c lengths. According to the JPSDS card (Nº 96-433-5635), for the one-step method, the unit cell parameters of perovskite are a a=b=6.3120 Å and c=6.3160 Å, α=γ=β= 90º. Simultaneously, the two-step method are a=b=8.8394 Å and c=12.4264 Å, α=γ=β= 90º according to the JPSDS car (Nº 4124388). The difference in cell parameters could arise from the dynamics of nucleation. The nucleation for the one-step method occurs in the first 5 s of the spin-coating process, just before the anti-solvent addition. For the two-step method, the nucleation and crystal growth occur in a time of tens of minutes. Therefore, the unit cell-size comes to be different. Besides, the diffractogram for the film deposited by the one-step method showed a preferential orientation only in three peaks, while films deposited by the two-step method showed up to ten peaks. This indicated a better crystallographic arrangement for films deposited by the one-step method, which in turn could affect their electrical properties; this is an important feature observed for these films. It should be worth noting that, although the final material is considered $MAPbI_3$, the initial solution is also composed of $PbCl_2$ in contrast to the two-step method where only PbI_2 and MAI are used. This result indicates that the use of $PbCl_2$ in the preparation of the two-step method is an alternative worth looking into.

The UV-Vis absorption spectra recorded for perovskite films prepared by the one-step and two-step method showed the same edge of absorption at about 790 nm, which corresponds to a bandgap value of 1.56 eV. For both methods, the optical absorption was the same. Similarly, the morphology observed for the films deposited by the one-step and two-step method showed similar features; both are compact grains with almost no empty spaces between them (Figures 3.10 (a) and 3.15 (e), (k)). This morphology is reported to favor the charge transport and avoid charge recombination.

Figure 4.1 shows the J-V curves for the best devices prepared by the one-step and two-step methods and the average of electrical parameters are summarized in Table 4.1. The photovoltaic performance for devices prepared by the one-step and two-step method (CSS) showed a great difference; the average efficiency was 10.23% and 6.59%, respectively. Both V_{oc} and J_{sc} showed an increment of about 200 mV and 6 mA/cm^2; for the former, there is no direct evidence that support the improvement, but could be related with the changes in crystallographic parameters. While for the photocurrent, we suspect a higher charge carrier mobility. The higher mobility could arise from the better crystallinity described above but also from the presence of Cl into the perovskite structure. There has been reported that the use of chloride into perovskite leads to a high charge carrier mobility and, therefore, higher photocurrent for solar cell devices.

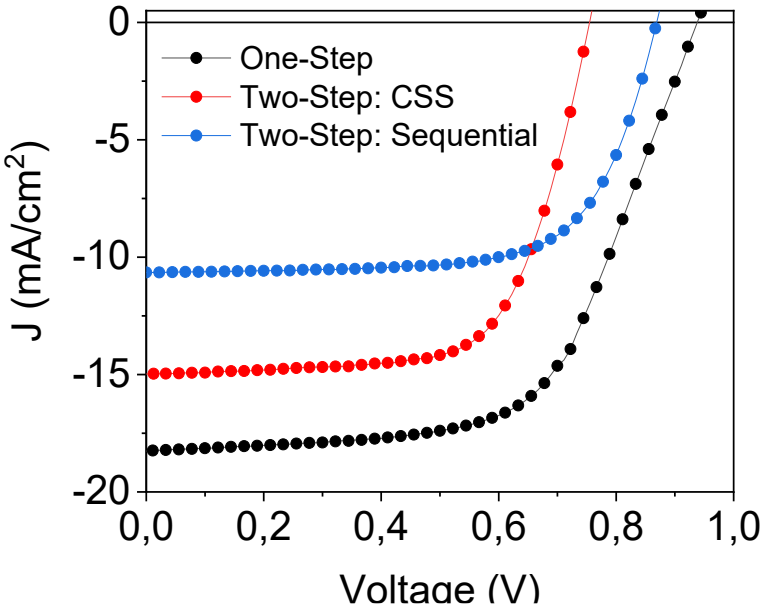

Figure 4.1 J-V curves of perovskite solar cells, based $MAPbI_3$ perovskite films prepared by one-step and two-step methods.

Table 4.1. Parameters from the perovskite solar cells based $MAPbI_3$ perovskite films prepared by one-step and two-step methods.

Sample	Voc [V]	Jsc[mA/cm^2]	FF	PCE [%]
One-Step	0.93 (0.92±0.01)	18.26 (18.33±0.41)	0.62 (0.61±0.01)	10.5 (10.23±0.21)
Two-Step: CSS	0.76 (0.73±0.03)	15.00 (12.75±2.07)	0.67 (0.63±0.04)	7.60 (6.59±1,01)
Two-Step: Sequential	0.87 (0.80±0.06)	10.66 (9.31±0.35)	0.69 (0.61±0.08)	6.37 (5.80±0.57)

The efficiency values of the cells fabricated with the one-step method are in the range of the average efficiency reported in the literature. Table 4.2 compares our results against those reported in the literature with similar architecture.

Table 4.2. Parameters from the perovskite solar cells based $MAPbI_3$ perovskite films prepared by one-step and PV parameters from other authors for similar HPSCs.

Sample	Voc [V]	Jsc[mA/cm^2]	FF	PCE [%]	Ref.
ITO/PEDOT:PSS/$MAPbI_3$/$PC_{71}BM$/FM	0.93 (0.92±0.02)	18.26 (18.33±0.40)	0.62 (0.61±0.04)	10.50 (10.2±0.60)	This work
ITO/PEDOT: PSS/$MAPbI_3Cl_X$/$PC_{71}BM$/Ca-Ag	0.91	17.76	0.73	11.82	[37]
ITO/PEDOT:PSS/$MAPbI_{3-x}Cl_x$/PCBM/Al	0.87	18.5	0.72	11.50	[36]
ITO/PEDOT:PSS/$MAPbI_{3-x}Cl_x$/PCBM/Al	0.84	18.32	0.71	10.93	[35]
ITO/PEDOT:PSS/$MAPbI_3$/PCBM/Bphen/Al	0.93	19.87	0.69	12.63	[34]
ITO/PEDOT:PSS/$MAPbI_3$/PCBM/Al	0.85	18.02	0.75	11.43	[33]
ITO/PEDOT:PSS/$MAPbI_3$/PCBM/LiF/Al	0.94	18.46	0.78	13.47	[32]
ITO/PEDOT:PSS/$MAPbI_3$/PCBM/BCP/Ag	0.93	13.53	0.58	7.33	[113]

4.2 Films deposited by two-step method

The films prepared by the two-step methods, either close-space sublimation or spin-coating with sequential deposition, showed the characteristic features of perovskite material; however, between them, important and interesting similarities and differences can be observed. In both methods a first layer of PbI_2 should be deposited and the features of PbI_2 film will affect those of perovskite material; the best PbI_2 film for preparation of perovskite layer was obtained when PbI_2-DMF solution and substrate were pre-heated at 100 ºC.

A first aspect that should be pointed out is that after being deposited, the PbI_2 film should be annealed at 120 ºC in a vacuum oven to be used in the spin-coating with sequential deposition; in contrast, for the close-space sublimation method, the film can be used just after being deposited without any additional process. For the sequential deposition method, traces of DMF solvent will interact with ethanol of MAI solution leading to dissolving perovskite and PbI_2 layers along the centrifugation waiting time. On the other hand, traces of DMF in PbI_2 film will help to diffuse MAI vapor in the sublimation method due to the formation of PbI_2-DMF coordination complexes that are replaced along the sublimation. Most of the reports on the CSS method for preparing perovskite layers do not take into account the effect of temperature on the deposition of the PbI_2 layer, nor do they consider the temperature used in its transformation into $MAPbI_3$.[114-115] In addition, although close-space sublimation method also uses heating process in a vacuum oven, the time for this process is similar than that used for sequential deposition (to eliminate DMF solvent). Therefore, it can be considered that the close-space sublimation method is an easier process for the preparation of perovskite films.

The best perovskite film prepared by either close-space sublimation or spin-coating with sequential deposition methods showed the same XRD pattern (Figures 3.13 (b) and 3.18 (b)). For both cases, the peaks showed the same position, intensity, and relative intensity; therefore, the same space group (*I_4/mcm space group*) was assigned. This indicates that both methods lead to obtain similar crystallinity for perovskite films once the best deposition conditions were achieved.

Interestingly, the absorption for perovskite films exhibits a slight difference. The edge of absorption for films prepared by close-space sublimation method is at 790 nm, while for films prepared by spin coating with sequential deposition is at 840 nm; the bandgap calculated from Tauc´s plot is 1.59 eV and 1.49 eV, respectively. The shift in the edge of absorption is still not clear; it could be due to concentration changes during the conversion process; however, according to the film characterization study, it is not possible to identify the reason for the shift in the edge of absorption. Chang et al. found that the band gap of $MAPbI_3$ perovskite gradually increases with increasing the CsI content. [116]

The morphology and thickness of films prepared with each method also shown differences; despite both films showed a granular morphology, the size and distribution of grains are different. Overall, the spin-coating with the sequential deposition method leads to spherical grains; but the grains are not compact and show several empty spaces. On the other hand, the grains observed in perovskite films prepared by the close-space sublimation method showed homogeneous distribution are compact with no empty spaces between them and larger size. The difference arises from the time that each method has for nucleation. For the spin-coating method, the time for nucleation is the named CWT, i.e., 15 s, 20 s, and 25 s; in contrast, for the close-space sublimation method, the slow rate

used for the MAI sublimation, about 60 minutes, leads to homogeneous nucleation and slow grain growth. Therefore, fewer empty spaces between grains are observed. The film thickness showed a stronger effect with the deposition method. For the best perovskite film obtained for spin-coating with sequential deposition and close-space sublimation method, the thickness was 300 nm and 415 nm, respectively. Although the PbI_2 layer was deposited under the same conditions for both methods, the one used for the spin-coating method has additional annealing to remove the solvent traces, which affect the thickness by removing formed PbI_2-DMF complexes. On the other hand, the complexes remain in the film used for close-space sublimation, increasing the thickness. This result confirms that the PbI_2 features determine la perovskite film characteristics.

The features above described for films deposited by either spin-coating with sequential deposition or sublimation technique showed influence on the photovoltaic performance of solar cells based on such films. The average of photovoltaic parameters for the best devices fabricated by spin-coating method are V_{oc} = 0.8 V, J_{sc} = 9.31 mA/cm^2, FF = 0.61, and PCE = 5.8%; while for close-space sublimation method are V_{oc} = 0.73 V, J_{sc} = 12.75 mA/cm^2, FF = 0.63, and PCE = 6.59%. The results are in good agreement with perovskite features. Overall, the V_{oc} is related to the perovskite bandgap; therefore, the higher V_{oc} for devices prepared by the spin-coating with sequential deposition method agree with the higher bandgap value calculated for these films. However, for devices prepared by the close-space sublimation method, the best photocurrent and fill factor could be related to morphological characteristics. The compact and larger grains favor the charge transport and reduce the charge traps related to empty spaces at grain boundaries. The final PCE is a consequence of the photovoltaic parameters; therefore, it is higher for devices prepared by the sublimation method.

An overall comparison of two-step methods for perovskite film deposition suggests that the close-space sublimation method is the easier method that allows better control of optical, crystallographic, and morphological properties of the deposited film. These features finally lead to better photovoltaic parameters.

Close space sublimation method has previously been used to prepare efficient large-area perovskite films. [114-115] For example, Li and coworkers [114] report the fabrication of perovskite films as large as 25 cm^2 by closed space vapor transport. The MAI vapor, generated under an N_2 atmosphere (2.5 mbar) at 160 ºC, reacts with the PbI_2 layer heated at 150 ºC. For $MAPbI_3$-based devices, Li et al. [114] report an efficiency of 14% for an active area of 1 cm^2, which highlights an easy and low-cost method for preparing large-area films. Also, Guo et al. [115] reported the use of the close space sublimation method for the deposition of 1 cm^2 perovskite films. In this case, the PbI_2 films were deposited by spin coating at room temperature (RT), but the sublimation of MAI was carried out at 150 ºC under a pressure of -1 bar over 2.5 h to achieve an efficiency of 10.8% for devices with 1 cm^2 active area.

5. Conclusions

In this work, we analyzed $MAPbI_3$ perovskite films for their use as an active layer in hybrid perovskite solar cells (HPSCs). For this purpose, we use the two most common film preparation methods, one-step and the two-step methods. The aim was to do a comparison of both methods for obtaining high quality films. To do so, some experimental parameters were worked out to identify their effect on the performance of the fabricated devices. It is also reported that poor physical contact in ETL/FM interface of devices fabricated and tested does not significantly reduce their performance. This was probed when the efficiency of these devices was contrasted with the efficiency of devices with counter electrode evaporated. The maximum efficiency for our devices with FM was 10.5% and for the evaporated counter electrode devices 11.6%. Therefore, in this work some factors are reported that indeed affect quality and reproducibility of the perovskite films and therefore the quality of HPSCs. Some of the main results from our analysis are listed below.

(1) For the one-step method, washing with chlorobenzene (anti-solvent) induces fast nucleation that significantly affects the crystallinity, optical absorption, morphology, and thus the reproducibility of perovskite films. However, the time when the anti-solvent should be dispensed is a parameter few studied and the results obtained here show that the optimal time is 5 s after the spin process began. At this time, chlorobenzene induces the supersaturation of the precursor solution, allowing better control of crystallization to achieve a morphology with a well-defined granular structure, highly compact grains, and low roughness. Besides, it

was determined that the dropped anti-solvent volume in a wide range of 100-800 μl does not influence the supersaturation processes.

(2) It was observed that the annealing temperature of the $MAPbI_3$ film deposited by the one-step method has an important effect on the morphology. At lower temperatures, i.e., 80 ºC, a more controlled crystallization process can be achieved, allowing the formation of films with larger grain size and homogeneous distribution. A variation of only 20 ºC (above 80 ºC) leads to zones with a lack of surface coverage. This indicates that, although anti-solvent induces supersaturation and fast nucleation, a rearrangement of perovskite material can be done into the film even after solvent evaporation.

(3) In the two-step method, spin-coating with sequential deposition, it was found that the centrifugation waiting time affected the conversion rate from PbI_2 to $MAPbI_3$ and the reproducibility of the perovskite films. The time waiting determined the diffusion of MAI in the PbI_2 layer and the nucleation. This caused the $MAPbI_3$ films to adopt different grain sizes and morphology. The best waiting time was about 20 s, which leads to a better morphology, optical absorption, and crystallinity.

(4) For $MAPbI_3$ perovskite films prepared by the close-space sublimation method (two- step), film morphology showed the biggest-compact grains with no empty spaces between them and high crystallinity. The features for these films come from the formation of PbI_2-DMF complexes that help the reaction between deposited PbI_2 film and MAI vapor. In comparing the two-step methods, the close-space sublimation technique was an easier methodology to achieve homogeneous and reproducible $MAPbI_3$ films.

(5) The one-step and two-step methods for deposition of perovskite films need the deposition of a PbI_2 layer. Although the first step involves only one of the perovskite precursors, the features of the PbI_2 layer will determine the characteristics of the perovskite film; the main factor is related to morphology. The best conditions for deposition of PbI_2 is pre-heating the solution and substrate at 100 ºC before deposition by the spin-coating technique. However, the close-space sublimation method needs a vacuum oven with temperature for the preparation of perovskite film. These conditions make sublimation a more complex method. Therefore, the one-step spin-coating technique is an easier method.

(6) The photovoltaic performance for devices prepared by either the one-step or two-step methods was affected by the whole film features, i.e., the morphological, crystalline, and optical absorption. However, the most important parameter to achieve cells with acceptable PCE and reproducibility is the quality of the perovskite film. $MAPbI_3$ films that adopted a morphology with a more compact granular structure (with few pinholes), with well-defined grain shape and grain size larger than 400 nm showed the best photovoltaic performance for each deposition methodology. Obtaining these films with such characteristics was possible by varying different parameters in each methodology. The study of these parameters allowed a better control in the crystallization of the perovskite films, which resulted in a better structural arrangement.

(7) A detailed study of the interface between ETL and the alternative counter-electrode (CE) Field´s metal (FM) found poor physical contact and large "empty spaces" within the range of a few hundred nanometers. In contrast, an evaporated

CE (Ca/Ag) used as a reference (i.e., ETL-Ca/Ag interface) showed a smooth interface with good physical contact. Despite empty spaces at the ETL-FM interface, the device performance with this alternative CE was comparable to the reference device. The best PCE values for the alternative and evaporated CE were 10.5% and 11.6%, respectively. The above demonstrates that defects at the ETL-FM interface do not explicitly determine charge collection, suggesting that electrons could move along the perovskite layer until reaching a zone with homogeneous ETL-CE contact a continuous contact at the ETL-CE interface might not be mandatory for acceptable HPSC performance.

Future work

Regarding the research carried out in this thesis work, different methods of deposition of $MAPbI_3$ films for use as an active layer in inverted architecture solar cell devices is proposed as future work:

1. Use of best parameters for each method to prepare large area perovskite films (greater than 1 cm^2).

2. Evaluate other solvents such as: toluene or ethyl acetate as an anti-solvent.

3. For the close space sublimation method carry out the sublimation of formamidinium iode (FAI) instead MAI.

4. For sequential deposition use a FAI-solution to prepare $FAPbI_3$ and study the best time for reaction.

Scientific publications

1. **Diana Marcela Montoya**, Enrique Pérez-Gutiérrez, Oracio Barbosa-Garcia, Wilson Bernal, José-Luis Maldonado, M. Judith Percino, Marco-Antonio Meneses, Margarita Cerón. *Defects at the interface electron transport layer and alternative counter electrode, their impact on perovskite solar cells performance*. Sol. Energy 195, 610–617 (2020).

2. Enrique Pérez-Gutiérrez, M. Judith Percino, Pilar Santos, Margarita Cerón, Paulina Ceballos, **Diana Marcela Montoya**, Oracio Barbosa-García,Subbiah Thamotharan. Compositional study of mixed halide perovskite films $CH_3NH_3Pb(I_{1-x}Br_x)_3$ and $CH_3NH_3Pb(I_{1-x}Cl_x)_3$ prepared by close space sublimation. Materials Today Communications 25 101384 (2020).

3. Enrique Pérez-Gutiérrez, M. Judith Percino, **Diana Marcela Montoya**, Diego Solis-Ibarra, Margarita Cerón, and Oracio Barbosa-Garcia. *Control of the Morphology and Crystallinity of a PbI_2 Layer for Large-Area Perovskite Films Prepared by Close Space Sublimation.* ACS Appl. Energy Mater (2018).

References

[1] REN21, "RENEWABLES 2020 GLOBAL STATUS REPORT," 2020. [Online]. Available: https://www.ren21.net/wp-content/uploads/2019/05/gsr_2020_full_report_en.pdf.

[2] H. Bahar, D. D'Ambrosio, R. Malischek, and H. Paillere, "Tracking Power," *IEA*, 2019.

[3] M. Zeman, "SOLAR CELL OPERATIONAL PRINCIPLES," in *SOLAR CELLS*, p. 41.

[4] S. H. Antonio Luque, *Handbook of Photovoltaic Science and Engineering*, Wiley. .

[5] Y. Kuang, M. Di Vece, J. K. Rath, L. van Dijk, and R. E. I. Schropp, "Elongated nanostructures for radial junction solar cells," *Reports Prog. Phys.*, vol. 76, no. 10, p. 106502, Oct. 2013.

[6] M. Kim *et al.*, "Study on efficiency improvement of multi-crystalline silicon solar cell by removing by-product and plasma induced damage generated during reactive ion etching," *Curr. Appl. Phys.*, vol. 20, no. 4, pp. 519–524, Apr. 2020.

[7] Sabu Thomas and Aparna Thankappan, *Perovskite Photovoltaics*. Elsevier, 2018.

[8] W. C. Sinke, "Development of photovoltaic technologies for global impact," *Renew. Energy*, vol. 138, pp. 911–914, Aug. 2019.

[9] S.-U.-I. Mohammad Tawheed Kibria, Akil Ahammed, Saad Mahmud Sony, Faisal Hossain, "A Review: Comparative studies on different generation solar cells technology," in *Proceedings of 5th International Conference on Environmental Aspects of Bangladesh [ICEAB 2015]*, 2015, pp. 51–53.

[10] I. Caballero-Quintana *et al.*, "Scanning Probe Microscopy Analysis of Nonfullerene Organic Solar Cells," *ACS Appl. Mater. Interfaces*, p. acsami.0c06048, Jun. 2020.

[11] O. Amargós-Reyes *et al.*, "Organic photovoltaic cell analysis through quantum efficiency and scanning tunneling microscopy of the donor/blend as an active film," *J. Mater. Sci.*, vol. 54, no. 3, pp. 2427–2445, Feb. 2019.

[12] D. Barreiro-Argüelles *et al.*, "Stability study in organic solar cells based on PTB_7:$PC_{71}BM$ and the scaling effect of the active layer," *Sol. Energy*, vol. 163, pp. 510–518, Mar. 2018.

[13] Best Research-Cell Efficiency, "National Renewable Energy," 2021. .

[14] "Best Research-Cell Efficiency Chart," *National Renewable Energy Laboratory*, 2020. [Online]. Available: https://www.nrel.gov/pv/cell-efficiency.html. [Accessed: 26-May-2020].

[15] Z. Shi and A. Jayatissa, "Perovskites-Based Solar Cells: A Review of Recent Progress, Materials and Processing Methods," *Materials (Basel).*, vol. 11, no. 5, p. 729, May 2018.

[16] P. Roy, N. Kumar Sinha, S. Tiwari, and A. Khare, "A review on perovskite solar cells: Evolution of architecture, fabrication techniques, commercialization issues and status," *Sol. Energy*, vol. 198, pp. 665–688, Mar. 2020.

[17] Q. Chen *et al.*, "Under the spotlight: The organic–inorganic hybrid halide perovskite for optoelectronic applications," *Nano Today*, vol. 10, no. 3, pp. 355–396, Jun. 2015.

[18] Y. Chen, N. Zhou, and H. Zhou, "Organic Inorganic Hybrid Perovskite Materials and Devices," in *Encyclopedia of Modern Optics*, Elsevier, 2018, pp. 282–291.

[19] F.-C. Chen, “Emerging Organic and Organic/Inorganic Hybrid Photovoltaic Devices for Specialty Applications: Low-Level-Lighting Energy Conversion and Biomedical Treatment,” *Adv. Opt. Mater.*, vol. 7, no. 1, p. 1800662, Jan. 2019.

[20] Y. Yamada, T. Nakamura, M. Endo, A. Wakamiya, and Y. Kanemitsu, “Near-band-edge optical responses of solution-processed organic–inorganic hybrid perovskite $CH_3NH_3PbI_3$ on mesoporous TiO_2 electrodes,” *Appl. Phys. Express*, vol. 7, no. 3, p. 032302, Mar. 2014.

[21] S. Liu, F. Zheng, N. Z. Koocher, H. Takenaka, F. Wang, and A. M. Rappe, “Ferroelectric Domain Wall Induced Band Gap Reduction and Charge Separation in Organometal Halide Perovskites,” *J. Phys. Chem. Lett.*, vol. 6, no. 4, pp. 693–699, Feb. 2015.

[22] N. Pellet *et al.*, “Mixed-Organic-Cation Perovskite Photovoltaics for Enhanced Solar-Light Harvesting,” *Angew. Chemie Int. Ed.*, vol. 53, no. 12, pp. 3151–3157, Mar. 2014.

[23] J. Akhtar, M. Aamir, and M. Sher, “Organometal Lead Halide Perovskite,” in *Perovskite Photovoltaics*, Elsevier, 2018, pp. 25–42.

[24] A. Kojima, K. Teshima, Y. Shirai, and T. Miyasaka, “Organometal Halide Perovskites as Visible-Light Sensitizers for Photovoltaic Cells,” *J. Am. Chem. Soc.*, vol. 131, no. 17, pp. 6050–6051, May 2009.

[25] J.-H. Im, C.-R. Lee, J.-W. Lee, S.-W. Park, and N.-G. Park, “6.5% efficient perovskite quantum-dot-sensitized solar cell,” *Nanoscale*, vol. 3, no. 10, p. 4088, 2011.

[26] H.-S. Kim *et al.*, “Lead Iodide Perovskite Sensitized All-Solid-State Submicron Thin Film Mesoscopic Solar Cell with Efficiency Exceeding 9%,” *Sci. Rep.*, vol.

2, no. 1, p. 591, Dec. 2012.

[27] J.-Y. Jeng *et al.*, "$CH_3NH_3PbI_3$ Perovskite/Fullerene Planar-Heterojunction Hybrid Solar Cells," *Adv. Mater.*, vol. 25, no. 27, pp. 3727–3732, Jul. 2013.

[28] F. El-Mellouhi, E. T. Bentria, S. N. Rashkeev, S. Kais, and F. H. Alharbi, "Enhancing Intrinsic Stability of Hybrid Perovskite Solar Cell by Strong, yet Balanced, Electronic Coupling," *Sci. Rep.*, vol. 6, no. 1, p. 30305, Jul. 2016.

[29] C. Yi *et al.*, "Entropic stabilization of mixed A-cation ABX_3 metal halide perovskites for high performance perovskite solar cells," *Energy Environ. Sci.*, vol. 9, no. 2, pp. 656–662, 2016.

[30] X. Li *et al.*, "A vacuum flash–assisted solution process for high-efficiency large-area perovskite solar cells," *Science (80-.).*, vol. 353, no. 6294, pp. 58–62, Jul. 2016.

[31] M. Saliba *et al.*, "Cesium-containing triple cation perovskite solar cells: improved stability, reproducibility and high efficiency," *Energy Environ. Sci.*, vol. 9, no. 6, pp. 1989–1997, 2016.

[32] M. Jahandar *et al.*, "High-performance $CH_3NH_3PbI_3$ inverted planar perovskite solar cells via ammonium halide additives," *J. Ind. Eng. Chem.*, Aug. 2019.

[33] X. Huang, K. Wang, C. Yi, T. Meng, and X. Gong, "Efficient Perovskite Hybrid Solar Cells by Highly Electrical Conductive PEDOT:PSS Hole Transport Layer," *Adv. Energy Mater.*, vol. 6, no. 3, p. 1501773, Feb. 2016.

[34] Z. Liu *et al.*, "Improvement in the performance of inverted planar perovskite solar cells via the $CH_3NH_3PbI_{3-x}Cl_x$:ZnO bulk heterojunction," *J. Power Sources*, vol. 401, pp. 303–311, Oct. 2018.

[35] L. Peng and Z. Liu, "Reduce the hysteresis effect with the PEIE interface dipole

effect in the organic-inorganic hybrid perovskite $CH_3NH_3PbI_{3-x}Cl_x$ solar cell," *Org. Electron.*, vol. 62, pp. 630–636, Nov. 2018.

[36] J. You *et al.*, "Low-Temperature Solution-Processed Perovskite Solar Cells with High Efficiency and Flexibility," *ACS Nano*, vol. 8, no. 2, pp. 1674–1680, Feb. 2014.

[37] N. Tripathi, M. Yanagida, Y. Shirai, T. Masuda, L. Han, and K. Miyano, "Hysteresis-free and highly stable perovskite solar cells produced via a chlorine-mediated interdiffusion method," *J. Mater. Chem. A*, vol. 3, no. 22, pp. 12081–12088, 2015.

[38] T.-T. Duong, P. H. Hoang, L. T. Nhan, L. Van Duong, M. H. Nam, and L. Q. Tuan, "Multistep spin–spray deposition of large-grain-size $CH_3NH_3PbI_3$ with bilayer structure for conductive-carbon-based perovskite solar cells," *Curr. Appl. Phys.*, vol. 19, no. 11, pp. 1266–1270, Nov. 2019.

[39] J. H. Heo *et al.*, "Efficient inorganic–organic hybrid heterojunction solar cells containing perovskite compound and polymeric hole conductors," *Nat. Photonics*, vol. 7, no. 6, pp. 486–491, Jun. 2013.

[40] J.-H. Im, I.-H. Jang, N. Pellet, M. Grätzel, and N.-G. Park, "Growth of $CH_3NH_3PbI_3$ cuboids with controlled size for high-efficiency perovskite solar cells," *Nat. Nanotechnol.*, vol. 9, no. 11, pp. 927–932, Nov. 2014.

[41] W. S. Yang *et al.*, "Iodide management in formamidinium-lead-halide–based perovskite layers for efficient solar cells," *Science (80-.).*, vol. 356, no. 6345, pp. 1376–1379, Jun. 2017.

[42] M. M. Lee, J. Teuscher, T. Miyasaka, T. N. Murakami, and H. J. Snaith, "Efficient Hybrid Solar Cells Based on Meso-Superstructured Organometal Halide

Perovskites," *Science (80-.).*, vol. 338, no. 6107, pp. 643–647, Nov. 2012.

[43] G. E. Eperon, V. M. Burlakov, P. Docampo, A. Goriely, and H. J. Snaith, "Morphological Control for High Performance, Solution-Processed Planar Heterojunction Perovskite Solar Cells," *Adv. Funct. Mater.*, vol. 24, no. 1, pp. 151–157, Jan. 2014.

[44] H.-S. Kim, A. Hagfeldt, and N.-G. Park, "Morphological and compositional progress in halide perovskite solar cells," *Chem. Commun.*, vol. 55, no. 9, pp. 1192–1200, 2019.

[45] M. Liu, M. B. Johnston, and H. J. Snaith, "Efficient planar heterojunction perovskite solar cells by vapour deposition," *Nature*, vol. 501, no. 7467, pp. 395–398, Sep. 2013.

[46] P. Wang *et al.*, "Gradient Energy Alignment Engineering for Planar Perovskite Solar Cells with Efficiency Over 23%," *Adv. Mater.*, vol. 32, no. 6, p. 1905766, Feb. 2020.

[47] P. Docampo, J. M. Ball, M. Darwich, G. E. Eperon, and H. J. Snaith, "Efficient organometal trihalide perovskite planar-heterojunction solar cells on flexible polymer substrates," *Nat. Commun.*, vol. 4, no. 1, p. 2761, Dec. 2013.

[48] S. Paek *et al.*, "Improved External Quantum Efficiency from Solution-Processed $(CH_3NH_3)PbI_3$ Perovskite/$PC_{71}BM$ Planar Heterojunction for High Efficiency Hybrid Solar Cells," *J. Phys. Chem. C*, vol. 118, no. 45, pp. 25899–25905, Nov. 2014.

[49] X. Zheng *et al.*, "Managing grains and interfaces via ligand anchoring enables 22.3%-efficiency inverted perovskite solar cells," *Nat. Energy*, vol. 5, no. 2, pp. 131–140, Feb. 2020.

[50] J. Prakash *et al.*, “Progress in tailoring perovskite based solar cells through compositional engineering: Materials properties, photovoltaic performance and critical issues,” *Mater. Today Energy*, vol. 9, pp. 440–486, Sep. 2018.

[51] K. Zhang *et al.*, “Improve the crystallinity and morphology of perovskite films by suppressing the formation of intermediate phase of $CH_3NH_3PbCl_3$,” *Org. Electron.*, vol. 68, pp. 96–102, May 2019.

[52] J. Yi *et al.*, “Regulated perovskite crystallinity via green mixed antisolvent for efficient perovskite solar cells,” *Org. Electron.*, vol. 69, pp. 69–76, Jun. 2019.

[53] Z. Shao *et al.*, “Tailoring perovskite conversion and grain growth by in situ solvent assisted crystallization and compositional variation for highly efficient perovskite solar cells,” *Org. Electron.*, vol. 69, pp. 208–215, Jun. 2019.

[54] L. Zheng *et al.*, “Morphology control of the perovskite films for efficient solar cells,” *Dalt. Trans.*, vol. 44, no. 23, pp. 10582–10593, 2015.

[55] W. Ruan, Y. Hu, T. Qiu, F. Bai, S. Zhang, and F. Xu, “Morphological regulation of all-inorganic perovskites for multilevel resistive switching,” *J. Phys. Chem. Solids*, vol. 127, pp. 258–264, Apr. 2019.

[56] F. Zhang *et al.*, “A facile route to grain morphology controllable perovskite thin films towards highly efficient perovskite solar cells,” *Nano Energy*, vol. 53, pp. 405–414, Nov. 2018.

[57] C. Li *et al.*, “Efficient lead acetate sourced planar heterojunction perovskite solar cells with enhanced substrate coverage via one-step spin-coating,” *Org. Electron.*, vol. 33, pp. 194–200, Jun. 2016.

[58] D. Y. Torres-Martínez, M. Millán, B. Aguilar, and O. Navarro, “Synthesis and characterization of $CH_3NH_3PbI_3$ perovskite thin films obtained in one step,” *Phys.*

B Condens. Matter, vol. 585, p. 412081, May 2020.

[59] A. E. Lewis, Y. Zhang, P. Gao, and M. K. Nazeeruddin, "Unveiling the Concentration-Dependent Grain Growth of Perovskite Films from One- and Two-Step Deposition Methods: Implications for Photovoltaic Application," *ACS Appl. Mater. Interfaces*, vol. 9, no. 30, pp. 25063–25066, Aug. 2017.

[60] J. Burschka *et al.*, "Sequential deposition as a route to high-performance perovskite-sensitized solar cells," *Nature*, vol. 499, no. 7458, pp. 316–319, Jul. 2013.

[61] L. K. Ono, M. R. Leyden, S. Wang, and Y. Qi, "Organometal halide perovskite thin films and solar cells by vapor deposition," *J. Mater. Chem. A*, vol. 4, no. 18, pp. 6693–6713, 2016.

[62] B. Conings *et al.*, "Structure–Property Relations of Methylamine Vapor Treated Hybrid Perovskite $CH_3NH_3PbI_3$ Films and Solar Cells," *ACS Appl. Mater. Interfaces*, vol. 9, no. 9, pp. 8092–8099, Mar. 2017.

[63] C. F. Arias-Ramos, Y. Kumar, P. G. Abrego-Martínez, and H. Hu, "Efficient and stable hybrid perovskite prepared at 60% relative humidity with a hydrophobic additive in anti-solvent," *Sol. Energy Mater. Sol. Cells*, vol. 215, p. 110625, Sep. 2020.

[64] P.-W. Liang *et al.*, "Additive Enhanced Crystallization of Solution-Processed Perovskite for Highly Efficient Planar-Heterojunction Solar Cells," *Adv. Mater.*, vol. 26, no. 22, pp. 3748–3754, Jun. 2014.

[65] N. J. Jeon, J. H. Noh, Y. C. Kim, W. S. Yang, S. Ryu, and S. Il Seok, "Solvent engineering for high-performance inorganic–organic hybrid perovskite solar cells," *Nat. Mater.*, vol. 13, no. 9, pp. 897–903, Sep. 2014.

[66] M. Xiao *et al.*, "A Fast Deposition-Crystallization Procedure for Highly Efficient Lead Iodide Perovskite Thin-Film Solar Cells," *Angew. Chemie Int. Ed.*, vol. 53, no. 37, pp. 9898–9903, Sep. 2014.

[67] Y. Zhou, M. Yang, W. Wu, A. L. Vasiliev, K. Zhu, and N. P. Padture, "Room-temperature crystallization of hybrid-perovskite thin films via solvent–solvent extraction for high-performance solar cells," *J. Mater. Chem. A*, vol. 3, no. 15, pp. 8178–8184, 2015.

[68] H.-B. Kim *et al.*, "Mixed solvents for the optimization of morphology in solution-processed, inverted-type perovskite/fullerene hybrid solar cells," *Nanoscale*, vol. 6, no. 12, p. 6679, 2014.

[69] Z. Li *et al.*, "Scalable fabrication of perovskite solar cells," *Nat. Rev. Mater.*, vol. 3, no. 4, p. 18017, Apr. 2018.

[70] Y. Zhao and K. Zhu, "CH_3NH_3Cl-Assisted One-Step Solution Growth of $CH_3NH_3PbI_3$: Structure, Charge-Carrier Dynamics, and Photovoltaic Properties of Perovskite Solar Cells," *J. Phys. Chem. C*, vol. 118, no. 18, pp. 9412–9418, May 2014.

[71] C. Zuo and L. Ding, "An 80.11% FF record achieved for perovskite solar cells by using the NH_4Cl additive," *Nanoscale*, vol. 6, no. 17, p. 9935, Jul. 2014.

[72] Y. Chen, Y. Zhao, and Z. Liang, "Non-Thermal Annealing Fabrication of Efficient Planar Perovskite Solar Cells with Inclusion of NH_4Cl," *Chem. Mater.*, vol. 27, no. 5, pp. 1448–1451, Mar. 2015.

[73] J.-W. Lee, H.-S. Kim, and N.-G. Park, "Lewis Acid–Base Adduct Approach for High Efficiency Perovskite Solar Cells," *Acc. Chem. Res.*, vol. 49, no. 2, pp. 311–319, Feb. 2016.

[74] A. Dualeh, N. Tétreault, T. Moehl, P. Gao, M. K. Nazeeruddin, and M. Grätzel, "Effect of Annealing Temperature on Film Morphology of Organic-Inorganic Hybrid Pervoskite Solid-State Solar Cells," *Adv. Funct. Mater.*, vol. 24, no. 21, pp. 3250–3258, Jun. 2014.

[75] W. Nie *et al.*, "High-efficiency solution-processed perovskite solar cells with millimeter-scale grains," *Science (80-.).*, vol. 347, no. 6221, pp. 522–525, Jan. 2015.

[76] L.-L. Gao, C.-X. Li, C.-J. Li, and G.-J. Yang, "Large-area high-efficiency perovskite solar cells based on perovskite films dried by the multi-flow air knife method in air," *J. Mater. Chem. A*, vol. 5, no. 4, pp. 1548–1557, 2017.

[77] H. Chen *et al.*, "A solvent- and vacuum-free route to large-area perovskite films for efficient solar modules," *Nature*, vol. 550, no. 7674, pp. 92–95, Oct. 2017.

[78] L.-L. Gao *et al.*, "Preparation of flexible perovskite solar cells by a gas pump drying method on a plastic substrate," *J. Mater. Chem. A*, vol. 4, no. 10, pp. 3704–3710, 2016.

[79] J. Ye *et al.*, "Enhanced morphology and stability of high-performance perovskite solar cells with ultra-smooth surface and high fill factor via crystal growth engineering," *Sustain. Energy Fuels*, vol. 1, no. 4, pp. 907–914, 2017.

[80] B. Li *et al.*, "Spontaneously supersaturated nucleation strategy for high reproducible and efficient perovskite solar cells," *Chem. Eng. J.*, vol. 405, p. 126998, Feb. 2021.

[81] S. A. Olaleru, J. K. Kirui, D. Wamwangi, K. T. Roro, and B. Mwakikunga, "Perovskite solar cells: The new epoch in photovoltaics," *Sol. Energy*, vol. 196, pp. 295–309, Jan. 2020.

[82] C.-H. Chiang, M. K. Nazeeruddin, M. Grätzel, and C.-G. Wu, "The synergistic effect of H_2O and DMF towards stable and 20% efficiency inverted perovskite solar cells," *Energy Environ. Sci.*, vol. 10, no. 3, pp. 808–817, 2017.

[83] T.-B. Song *et al.*, "Perovskite solar cells: film formation and properties," *J. Mater. Chem. A*, vol. 3, no. 17, pp. 9032–9050, 2015.

[84] D. Angmo *et al.*, "A Lab-to-Fab Study toward Roll-to-Roll Fabrication of Reproducible Perovskite Solar Cells under Ambient Room Conditions," *Cell Reports Phys. Sci.*, vol. 2, no. 1, p. 100293, Jan. 2021.

[85] M. Saliba *et al.*, "How to Make over 20% Efficient Perovskite Solar Cells in Regular (n–i–p) and Inverted (p–i–n) Architectures," *Chem. Mater.*, vol. 30, no. 13, pp. 4193–4201, Jul. 2018.

[86] P. D. Matthews, D. J. Lewis, and P. O'Brien, "Updating the road map to metal-halide perovskites for photovoltaics," *J. Mater. Chem. A*, vol. 5, no. 33, pp. 17135–17150, 2017.

[87] J. Wang *et al.*, "Chlorobenzene: A Processing Solvent Enabling the Fabrication of Perovskite Solar Cells with Consecutive Double-Perovskite and Perovskite/Organic Semiconductor Bulk Heterojunction Layers," *Sol. RRL*, vol. 3, no. 5, p. 1800325, May 2019.

[88] Donald E. Sands, *Introduction to Crystallography*. Dover Publications, 2012.

[89] "Crystallography Open Database." [Online]. Available: http://www.crystallography.net/cod/.

[90] Y. Tidhar *et al.*, "Crystallization of Methyl Ammonium Lead Halide Perovskites: Implications for Photovoltaic Applications," *J. Am. Chem. Soc.*, vol. 136, no. 38, pp. 13249–13256, Sep. 2014.

[91] M. Xiao *et al.*, “Selection of an anti-solvent for efficient and stable cesium-containing triple cation planar perovskite solar cells,” *Nanoscale*, vol. 10, no. 25, pp. 12141–12148, 2018.

[92] O. Malinkiewicz *et al.*, “Perovskite solar cells employing organic charge-transport layers,” *Nat. Photonics*, vol. 8, no. 2, pp. 128–132, Feb. 2014.

[93] B. Li, V. Ferguson, S. R. P. Silva, and W. Zhang, “Defect Engineering toward Highly Efficient and Stable Perovskite Solar Cells,” *Adv. Mater. Interfaces*, vol. 5, no. 22, p. 1800326, Nov. 2018.

[94] Y. Chen *et al.*, “A universal strategy combining interface and grain boundary engineering for negligible hysteresis and high efficiency (21.41%) planar perovskite solar cells,” *J. Mater. Chem. A*, vol. 8, no. 13, pp. 6349–6359, 2020.

[95] J.-F. Wang *et al.*, “Surface engineering of perovskite films for efficient solar cells,” *Sci. Rep.*, vol. 7, no. 1, p. 14478, Dec. 2017.

[96] M. R. Ahmadian-Yazdi, F. Zabihi, M. Habibi, and M. Eslamian, “Effects of Process Parameters on the Characteristics of Mixed-Halide Perovskite Solar Cells Fabricated by One-Step and Two-Step Sequential Coating,” *Nanoscale Res. Lett.*, vol. 11, no. 1, p. 408, Dec. 2016.

[97] L. Xi, C. B. Boothroyd, T. Salim, S. Borghardt, Y. M. Lam, and B. E. Kardynał, “Facile in situ synthesis of stable luminescent organic–inorganic lead halide perovskite nanoparticles in a polymer matrix,” *J. Mater. Chem. C*, vol. 5, no. 29, pp. 7207–7214, 2017.

[98] E. Pérez-Gutiérrez, M. J. Percino, D. M. Montoya, D. Solis-Ibarra, M. Cerón, and O. Barbosa-García, “Control of the Morphology and Crystallinity of a PbI_2 Layer for Large-Area Perovskite Films Prepared by Close Space Sublimation,” *ACS*

Appl. Energy Mater., vol. 1, no. 8, pp. 3843–3849, Aug. 2018.

[99] P. Docampo *et al.*, "Solution Deposition-Conversion for Planar Heterojunction Mixed Halide Perovskite Solar Cells," *Adv. Energy Mater.*, vol. 4, no. 14, p. 1400355, Oct. 2014.

[100] S. Chavhan *et al.*, "Organo-metal halide perovskite-based solar cells with CuSCN as the inorganic hole selective contact," *J. Mater. Chem. A*, vol. 2, no. 32, pp. 12754–12760, 2014.

[101] W. Li, J. Fan, J. Li, Y. Mai, and L. Wang, "Controllable Grain Morphology of Perovskite Absorber Film by Molecular Self-Assembly toward Efficient Solar Cell Exceeding 17%," *J. Am. Chem. Soc.*, vol. 137, no. 32, pp. 10399–10405, Aug. 2015.

[102] A. Wakamiya *et al.*, "Reproducible Fabrication of Efficient Perovskite-based Solar Cells: X-ray Crystallographic Studies on the Formation of $CH_3NH_3PbI_3$ Layers," *Chem. Lett.*, vol. 43, no. 5, pp. 711–713, May 2014.

[103] J. S. Manser, M. I. Saidaminov, J. A. Christians, O. M. Bakr, and P. V. Kamat, "Making and Breaking of Lead Halide Perovskites," *Acc. Chem. Res.*, vol. 49, no. 2, pp. 330–338, Feb. 2016.

[104] C. Del Angel-Olarte, H. Moreno-García, and Gabriela-Palestino, "One-step method for the fabrication of high-quality perovskite thin-films under ambient conditions: Stability, morphological, optical, and electrical evaluation," *Thin Solid Films*, vol. 717, p. 138438, Jan. 2021.

[105] J. Su *et al.*, "Efficient Perovskite Solar Cells Prepared by Hot Air Blowing to Ultrasonic Spraying in Ambient Air," *ACS Appl. Mater. Interfaces*, vol. 11, no. 11, pp. 10689–10696, Mar. 2019.

[106] A. K. Jena, A. Kulkarni, and T. Miyasaka, “Halide Perovskite Photovoltaics: Background, Status, and Future Prospects,” *Chem. Rev.*, vol. 119, no. 5, pp. 3036–3103, Mar. 2019.

[107] A. S. Chouhan, N. P. Jasti, and S. Avasthi, “Effect of interface defect density on performance of perovskite solar cell: Correlation of simulation and experiment,” *Mater. Lett.*, vol. 221, pp. 150–153, Jun. 2018.

[108] M. Wang, B. Li, J. Yuan, F. Huang, G. Cao, and J. Tian, “Repairing Defects of Halide Perovskite Films To Enhance Photovoltaic Performance,” *ACS Appl. Mater. Interfaces*, vol. 10, no. 43, pp. 37005–37013, Oct. 2018.

[109] Y. Yang *et al.*, “An all-carbon counter electrode for highly efficient hole-conductor-free organo-metal perovskite solar cells,” *RSC Adv.*, vol. 4, no. 95, pp. 52825–52830, Oct. 2014.

[110] J. Zhao *et al.*, “Is Cu a stable electrode material in hybrid perovskite solar cells for a 30-year lifetime?,” *Energy Environ. Sci.*, vol. 9, no. 12, pp. 3650–3656, 2016.

[111] “Interface engineering of organic electronics,” *J. Mater. Chem.*, vol. 20, no. 13, p. 2491, 2010.

[112] A. Guerrero *et al.*, “Interfacial Degradation of Planar Lead Halide Perovskite Solar Cells,” *ACS Nano*, vol. 10, no. 1, pp. 218–224, Jan. 2016.

[113] J.-H. Tsai, I.-C. Cheng, C.-C. Hsu, C.-C. Chueh, and J.-Z. Chen, “Feasibility study of atmospheric-pressure dielectric barrier discharge treatment on $CH_3NH_3PbI_3$ films for inverted planar perovskite solar cells,” *Electrochim. Acta*, vol. 293, pp. 1–7, Jan. 2019.

[114] G. Li, J. Y. L. Ho, M. Wong, and H.-S. Kwok, “Low cost, high throughput and centimeter-scale fabrication of efficient hybrid perovskite solar cells by closed

space vapor transport," *Phys. status solidi - Rapid Res. Lett.*, vol. 10, no. 2, pp. 153–157, Feb. 2016.

[115] Q. Guo *et al.*, "The growth of a $CH_3NH_3PbI_3$ thin film using simplified close space sublimation for efficient and large dimensional perovskite solar cells," *Energy Environ. Sci.*, vol. 9, no. 4, pp. 1486–1494, 2016.

[116] R. Chang, Y. Yan, J. Zhang, Z. Zhu, and J. Gu, "Large-grain and smooth cesium doped $CH_3NH_3PbI_3$ perovskite films by cesium iodide post-treatment for improved solar cells," *Thin Solid Films*, vol. 712, p. 138279, Oct. 2020.

[117] Y. Wu *et al.*, "Retarding the crystallization of PbI_2 for highly reproducible planar-structured perovskite solar cells via sequential deposition," *Energy Environ. Sci.*, vol. 7, no. 9, pp. 2934–2938, 2014.

[118] G. Chen, J. Zheng, L. Zheng, X. Yan, H. Lin, and F. Zhang, "Crack-free $CH_3NH_3PbI_3$ layer via continuous dripping method for high-performance mesoporous perovskite solar cells," *Appl. Surf. Sci.*, vol. 392, pp. 960–965, Jan. 2017.

[119] Y. Rong *et al.*, "Solvent engineering towards controlled grain growth in perovskite planar heterojunction solar cells," *Nanoscale*, vol. 7, no. 24, pp. 10595–10599, 2015.

Appendix I

Effect of DMSO on the morphology and crystallization of PbI_2 films and $MAPbI_3$ perovskite films deposited by the close-space sublimation method.

Solvent chemistry is another important parameter that has been used to improve the quality perovskite films processed by one/two steps (spin-coating) methods. For example, for two steps method, the DMSO as co-solvent or the mixture DMF/DMSO have been employee to improve the solubility of the inorganic solution and retard the crystallization process of PbI_2 resulting in very uniform perovskite films. [101] To see the effect mixture DMF/DMSO on the morphology and crystallization of PbI_2 and $MAPbI_3$ (by the close-space sublimation method) films, PbI_2 films were prepared by spin-coating with mixture DMF/DMSO as solvent. DMF: DMSO volume ratios of 1: 0, 0.95: 0.05, 0.9: 0.1, 0.80: 0.2, 0.7: 0.3 and 0.6:0.4 v/v% (also simplified with solution A, B, C, D, E and F respectively in the following discussion) were used. The fabrication of perovskite was performed as specified in item 2.2.2.

The surface morphology of the PbI_2 deposited on PEDOT:PSS films were examined by AFM. Figure A1.1 shows the AFM topography of the PbI_2 films obtained with the A-F solutions. One can observe that the films exhibit grains with different distribution and size from the different solutions. As shown in Figure A1.1 (a), the PbI_2 film prepared from solution A, i.e. with solution in pure DMF forms a needle morphology, meanwhile, with the addition of DMSO, the morphology becomes more granular; the larger the

volume of co-solvent, the more spherical the grains are and the more compact they are with each other, which decreases the amount of pinholes. As a result of these changes, the roughness of the films also varied; for the samples from solutions A, B and C the values are ≤15 nm while for the samples of solutions D, E and F the roughnesses are higher (~ 40 nm). Such phenomenon implies that the introduction of DMSO plays a crucial role in the process of the nucleation and crystallization of PbI_2.

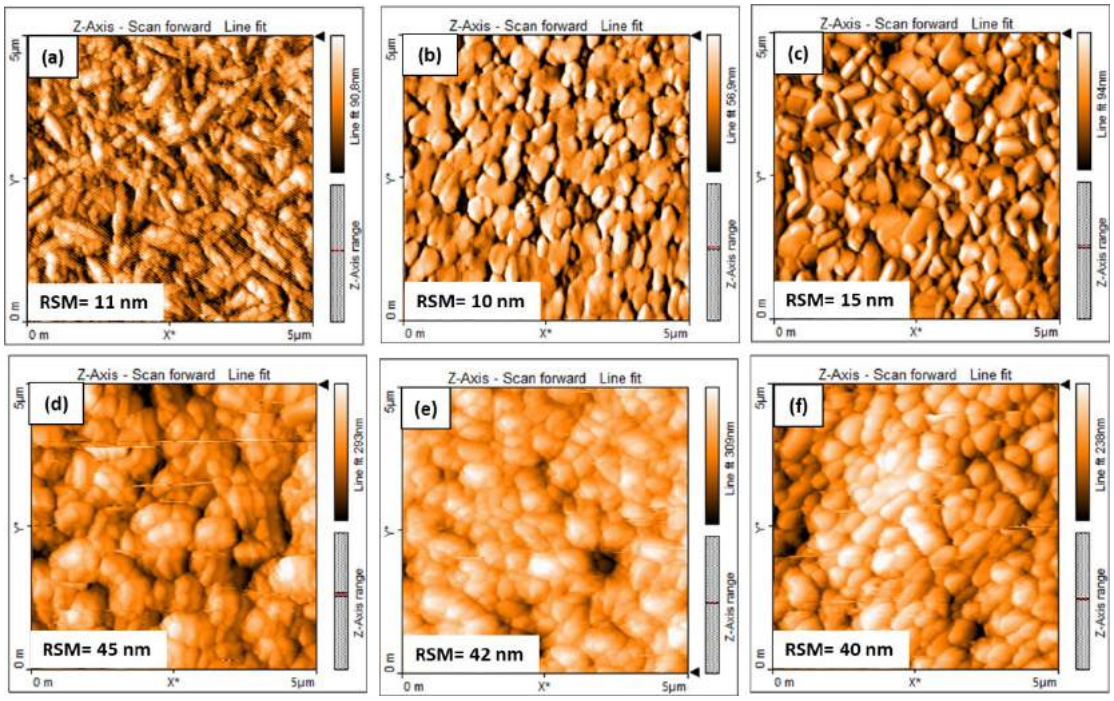

Figure A1.1 AFM images of PbI_2 films from DMF:DMSO solutions with volume ratios of (a) 1:0, (b) 0.95:0.05, (c) 0.9:0.1, (d) 0.80:0.2 (e) 0.7:0.3 and (f) 0.6:0.4v/v%.

Figure A1.2 exhibits the AFM images of $MAPbI_3$ perovskite films prepared by close-space sublimation method using the PbI_2 films of Figure A1.1. The $MAPbI_3$ films clearly displays different grain distribution, surface roughness, and coverage. This changes are consistent with the morphology of PbI_2 films. When the volume amount of DMSO is increased in precursor solutions of PbI_2, the perovskite films show a higher density of interconnected grains which leads to the formation of more compact films with fewer

pinholes (although not in full). The perovskite films from solutions C and F have less pinholes but the latter shows some grains that are no longer spherical, revealing the presence of anisotropy. When the amount of DMSO volume is increased, the roughness of the films increases but these values are in the range reported recently. [104-105]

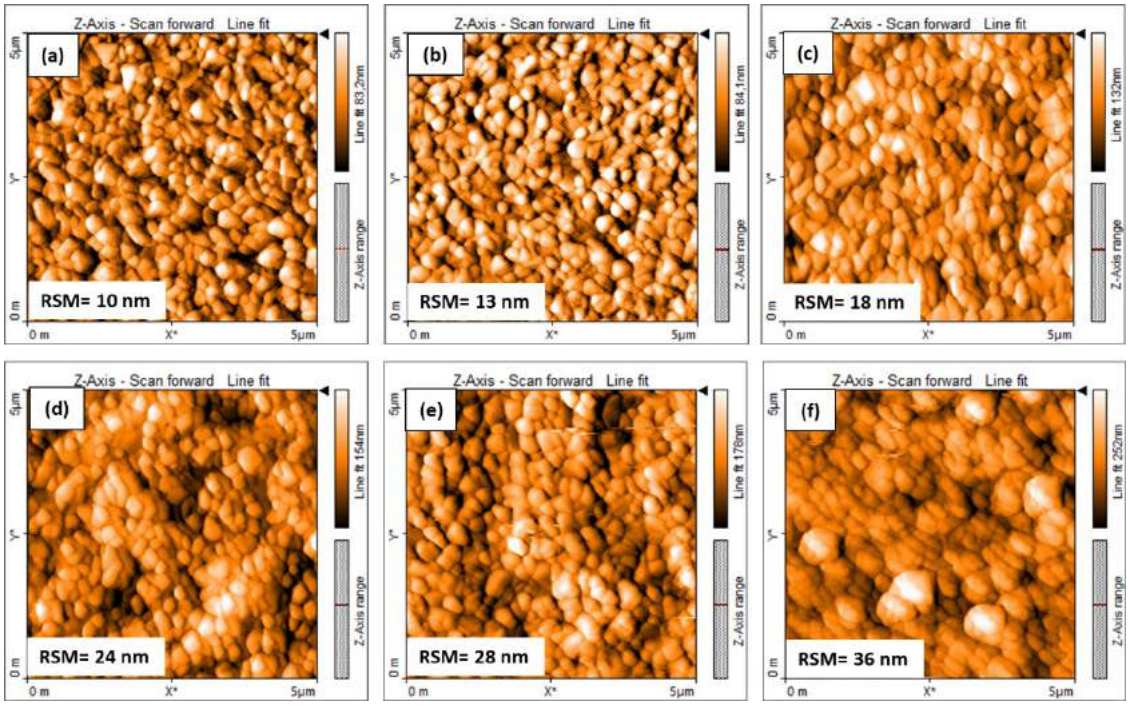

Figure A1.2 AFM images of $MAPbI_3$ films obtained by close-space sublimation method. The PbI_2 was deposited from solutions with DMF:DMSO volume ratios of (a) 1:0, (b) 0.95:0.05, (c) 0.9:0.1, (d) 0.80:0.2 (e) 0.7:0.3 and (f) 0.6:0.4v/v%.

The changes in the morphologies of PbI_2 and $MAPbI_3$ films is due to the crystallization rate of PbI_2. It is well known that DMSO retards the crystallization of PbI_2 due to its strong coordination ability with PbI_2 forming PbI_2•DMSO coordination complexes which enhances molecular ordering and allows slower crystal growth compared to films with DMF alone; if the crystal growth is slow it will result in a film with more compact grain. The existence of such complexes in our films was confirmed by XRD (see Figure A1.3).

Figure A1.3 (a) displays the evolution of the XRD patterns of PbI_2 film with DMSO ratio increasing. With the exception of film F, the XRD patterns correspond to PbI_2 with predominant crystallization along the planes (001) and (110) with diffraction peaks at 12.6º and 38.5º. When the DMSO ratio increasing the intensities of planes (001) and (110) decrease which suggests that the presence of DMSO retards the crystal growth of PbI_2 along all of the crystallographic directions. It has also been reported that the decrease in the intensity of PbI_2 peaks is related to the formation of PbI_2•DMSO complexes. [117] For film from solution F, the characteristic peaks of PbI_2 are completely quenched and it can be observed two new peaks located at 9.9º and 26º (see top box diffractogram). According to several reports these peaks correspond to formation the PbI_2•$(DMSO)_2$ complex. [101], [118] The PbI_2•$(DMSO)_2$ complex phase is significantly beneficial to the crystal growth and morphological control of perovskite film. [118]

(a) (b)

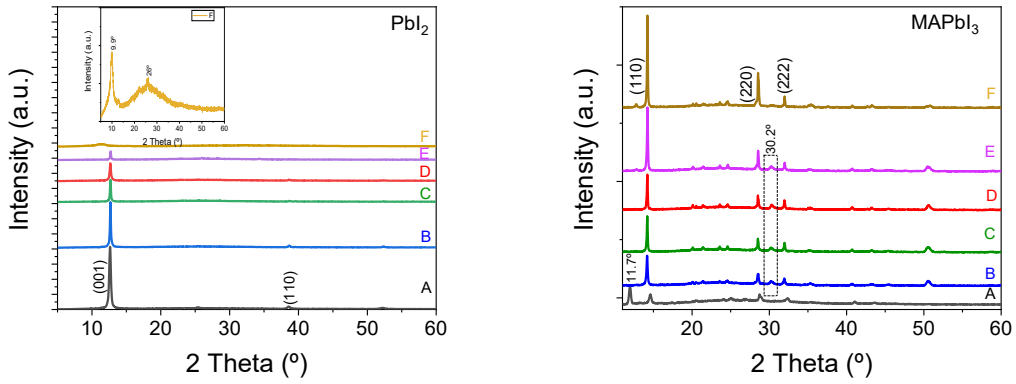

Figure A1.3 XRD patterns for (a) PbI_2 films from DMF:DMSO solutions with different volume ratios (b) PbI_2 films transformed into $MAPbI_3$ by close-space sublimation.

The XRD patterns of $MAPbI_3$ films are showed in Figure A1.3 (b). All XRD patterns show a set of diffraction peaks of $MAPbI_3$ perovskite tetragonal phase located at 2θ

around 14.2º, 28.6º and 31.9º. It can be observed that the film obtained from solution A (without DMSO) presents an additional peak at 11.7º which corresponds to the DMF•PbI_2 complex. The formation of this complex was discussed in session 3.2.1. With the addition of DMSO this peak disappears and a new peak is observed at 30.2º in the samples from solutions B, C, D and E. This peak is attributed to (172) plane of the MAI•PbI_2•DMSO complex and corresponds to an intermediate phase of $MAPbI_3$. The MAI•PbI_2•DMSO complex was first reported by Jeon et al.[65] using the solvent engineering method and the crystalline structure was identified by Rong et al. [119]As seen in our diffractograms, the peak of the complex disappears (in film F) and the intensities of the $MAPbI_3$ peaks become stronger with increasing DMSO ratio indicating more perfect crystallinity of $MAPbI_3$. Therefore the results suggest that the $MAPbI_3$ growth strongly correlates with the ratio DMF:DMSO in PbI_2 solution.

In addition, from the XRD study it can be inferred that highly crystallized PbI_2 films (from solutions A-D) lead to $MAPbI_3$ films with lower crystallinity while PbI_2 films with low crystallinity and amorphous character (from solutions A and F, respectively) lead to more crystalline perovskite films. Yongzhen Wu et al. reported that the amorphous nature of inorganic films, when exposed to the organic part, can generate perovskite crystals faster than crystalline PbI_2 films due to fast reaction of PbI_2 with MAI molecules. [117] This may explain the incomplete transformation of the samples prepared from solutions B-E since the sublimation time of all the films was the same.

It was studied the photovoltaic performance of perovskite solar cells prepared by tuning the concentration of DMSO and DMF from PbI_2 solutions (A-F solutions). Solar cells were assembled with the following configuration:

ITO/PEDOTS:PSS/$MAPbI_3$/$PC_{71}BM$/FM. Figure A1.4 shows the J-V curves solar cells and Table A1.1 summarizes the photovoltaic parameters, in parentheses the average and standard deviation values of 5 measurements are reported.

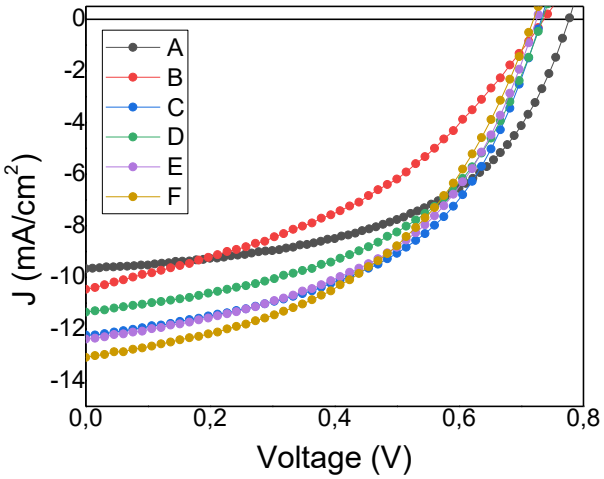

Figure A1.4 J-V curves of perovskite solar cells (best devices). $MAPbI_3$ films were transformed from PbI_2 films based on solutions with different volume ratios of DMF:DMSO.

As shown in Figure A1.4, with the addition of DMSO in the PbI_2 solution, the V_{oc} and FF slightly decreased while the J_{sc} of the solar cells suffered a small increase which contributed to an improved PCE. These variations in photovoltaic performance are consistent with the evolution of perovskite films morphology when the DMF:DMSO volume ratio varies. As expect, the devices fabricated with solutions C and F exhibit better J_{sc} because the perovskite films showed a more compact grain growth morphology which minimized the recombination processes. The best device was obtained from the sample of solution C whose photovoltaic parameters are: V_{oc} of 0.73 V, J_{sc} of 12.24 mA/cm^2, FF of 0.51, and PCE of 4.55%.

Table A1.1 Parameters from the best perovskite solar cells, based on $MAPbI_3$ films using PbI_2 films fabricate from solutions with different volume ratios of DMF:DMSO.

Sample	V_{oc} [V]	J_{sc}[mA/cm^2]	FF	PCE [%]
A	0.77	9.65	0.53	3.91 (2.99±0.92)
B	742	10.47	0.40	3.11 (2.51± 0.59)
C	0.73	12.24	0.51	4.55 (4.10±0.43)
D	0.73	11.35	0.50	4.13(3.80±0.33)
E	0.73	12.39	0.49	4.42 (3.62±0.82)
F	0.73	13.10	0.46	4.40 (3.59±0.79)

It has been found that the addition of DMSO improves the morphological and crystalline quality of perovskite films and that these have an influence on the performance of the device. The best performance of the device was obtained with sample C which presented an acceptably compact morphology with few pinholes. However, from the XRD study it was observed that this film did not present a pure crystalline phase of $MAPbI_3$; this one had remains of the MAI•PbI_2•DMSO complexes. This suggests that the remains of the complexes did not have a significant impact on the performance of the cells.